Parallel Resonances between Filter Capacitors and the Low Voltage Power Grid

Parallelresonanzen zwischen Filterkondensatoren und dem Niederspannungsnetz

Zur Erlangung des akademischen Grades Doktor-Ingenieur (Dr.-Ing.)
genehmigte Dissertation von Markus Bienholz aus Bochum
Tag der Einreichung: 08. März 2019, Tag der Prüfung: 03. Juni 2019
Darmstadt — D 17

1. Gutachten: Prof. Dr.-Ing. Gerd Griepentrog
2. Gutachten: Prof. Dr.-Ing. Johanna Myrzik

TECHNISCHE UNIVERSITÄT DARMSTADT

Fachbereich Elektrotechnik
und Informationstechnik

Institut für Stromrichtertechnik und Antriebsregelung
Fachgebiet Leistungselektronik

Parallel Resonances between Filter Capacitors and the Low Voltage Power Grid
Parallelresonanzen zwischen Filterkondensatoren und dem Niederspannungsnetz

Genehmigte Dissertation von Markus Bienholz aus Bochum

1. Gutachten: Prof. Dr.-Ing. Gerd Griepentrog
2. Gutachten: Prof. Dr.-Ing. Johanna Myrzik

Tag der Einreichung: 08. März 2019
Tag der Prüfung: 03. Juni 2019

Darmstadt — D 17

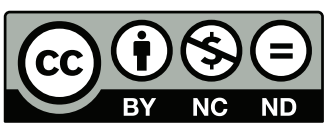

Contents

List of symbols and abbreviations

List of symbols

ε_0	$8.854 \times 10^{-12}\,\mathrm{F\,m^{-1}}$	permittivity of vacuum
$\mathbf{I}_n$		n^{th} order identity matrix
$\mathbf{O}_n$		n^{th} order square zero matrix

List of abbreviations

AC	alternating current
AIC	active infeed converter
CM	common mode
DC	direct current
DFT	digital fourier transform
DM	differential mode
DUT	device under test
EMC	electromagnetic compatibility
EMI	electromagnetic interference
ESL	equivalent series inductance
ESR	equivalent series resistance
IPM	intelligent power module
L1	first line of the utility grid
LISN	line impedance stabilization network
N	neutral line of the utility grid
PCC	point of common coupling
PE	protective earth
PIL	processor in the loop
PLL	phase locked loop
PWM	pulse width modulation
RCD	residual current detection
RMS	root mean square
THD	total harmonic distortion
VNA	vector network analyzer
VOC	voltage oriented control
VPI	vector proportional integrator

Abstract

This work studies the resonances which appear between the capacitors of power electronics grid interfaces and the inductance of the power grid. For this purpose it firstly introduces a frequency domain simulation method that is able to model asymmetrical components as well as symmetrical components. Models of typical power electronic components are derived from measurement for a frequency range of 2 kHz to 150 kHz. The asymmetrical cable model shows much better results than publications using a symmetrical model. A measurement procedure to measure impedances while connected to the power grid using coupling circuits is described and used for the measurement of the grid impedance up to 150 kHz.

A set of simulations of two power electronic converters at a point of common coupling is carried out, showing that a resonance between EMI filter capacitors and the grid inductance appears. The frequency of this resonance is determined by the value of the grid inductance and the total capacitance connected to the grid. The damping of the resonance and the resulting resonant currents are found to depend predominantly on the resistivity of the grid impedance. Long cables can shift and dampen the resonance, however connecting a load to the filter versus leaving it idle has no influence on the resonance.

Measurements are provided that prove all findings of the simulation and additionally demonstrate a thermal threat to the filter capacitors as well as a significant negative impact on the voltage quality at the point of common coupling.

Finally an integration of the EMI filter into an LCL filter is proposed. A first analysis shows equivalent behavior in terms of control while the total filter component size is decreased over the traditional approach. A decrease in filter damping is accompanied by decreased likeliness of exciting or suffering from a resonance with the power grid. Further improvements of this filter design are proposed for coming research.

Kurzfassung

Die vorliegende Arbeit befasst sich mit Resonanzen zwischen netzseitigen Kondensatoren leistungselektronischer Schaltungen und der Netzinduktivität. Hierzu wird zuerst eine Simulationsmethode im Frequenzbereich vorgestellt, die in der Lage ist sowohl symmetrische als auch asymmetrische Komponenten zu modellieren. Modelle aller typischen leistungselektronischen Bauteile werden durch Messungen für einen Frequenzbereich von 2 kHz bis 150 kHz bestimmt. Insbesondere das asymmetrische Kabelmodell zeigt deutliche Verbesserungen gegenüber in Veröffentlicheungen üblichen symmetrischen Modellen. Ein Messverfahren zur Vermessung von Impedanzen unter anliegender Netzspannung wird beschrieben und für die Bestimmung der Netzimpedanz bis 150 kHz verwendet.

Verschiedene Simulationen zweier Wechselrichter an einem gemeinsamen Anschlusspunkt werden durchgeführt um Resonanzen zwischen den Kondensatoren eines EMV-Filters und der Netzinduktivität nachzuweisen. Die Frequenz der Resonanz wird durch den Wert der Netzinduktivität und die gesamte Kapazität am Anschlusspunkt bestimmt. Die Dämpfung und die sich ergebenden Ströme hängen nachweislich hauptsächlich vom resistiven Anteil der Netzimpedanz ab.

Die dargestellten Messungen bestätigen die Erkenntnisse der Simulationen und zeigen darüber hinaus eine thermische Gefährdung der Filterkondensatoren sowie einen erheblichen negativen Einfluss auf die Spannungsqualität am Netzanschlusspunkt auf.

Abschließend wird die Integration des EMV-Filters in ein LCL-Filter vorgeschlagen. Eine erste Analyse dieses Vorgehens bestätigt ein gleichbleibendes regelungstechnisches Verhalten, während die benötigten Bauteilwerte reduziert werden. Eine Reduktion der Filterdämpfung steht einer Reduktion der Anregung sowie Anfälligkeit für Resonanzen mit dem Netz gegenüber. Optimierungsmöglichkeiten am vorgeschlagenen Filterdesign werden für künftige Untersuchungen aufgezeigt.

1 Introduction

Due to the increase in renewable energies connected to LV power grids [BSL+15] and the goal to increase the efficiency of loads connected, the amount of power electronic converters connected to the distribution grid is increasing as well. As the share of power fed into and consumed from the grid by power electronic circuits increases also the functional requirements of power electronics are increasing. These challenges can be allocated to different frequency ranges of interest.

At 50 Hz the control of active and reactive power in order to adjust the grid frequency and voltage becomes more important. The first renewable energy plants had only the goal to feed the maximum possible power into the grid at any given time. A grid frequency of 50.2 Hz was decided to be a non-acceptable operating condition for further power flow into the grid resulting in solar converters being programmed to turn off completely at this frequency. With the installed solar power reaching tens of gigawatts the sudden disconnect of this large share of power consumption could not be compensated by conventional power generation resulting in increasing possibility for islanding and partial to full black-outs of the European power grid. As a result the active power must be decreased by 40 % per 1 Hz frequency above 50.2 Hz and fully turned off at 51.5 Hz according to [VDE11] since 2012 in Germany. The European network of transmission system operators for electricity (ENTSO-E) is working on harmonizing the different legislation throughout Europe. The above example shows that an increase in grid services provided by power electronics concerning the active an reactive power control of the grid is to be expected with further increase in installed regenerative power generation.

In the classical power quality frequency range up to 2 kHz the increase in electronic consumers using diode front ends results in distortion of the grid voltage by harmonic currents which in turn is seen by any consumer and generator connected to the grid. The normative reaction to this is the decrease of nominal power for which power factor correction (PFC) is mandatory. This leads to more switched power electronic circuits in the grid typically utilizing EMI filters in order to comply with EMI standards.

The parallel connection of many converters has been shown to lead to additional resonances in this frequency range within the converters subgrid [EBWB17]. Since those frequencies are within the bandwidth of the current controllers they can be considered during the controller design [CBA+16], [FCG+15]. In the future the prediction or on-line determination and suppression of such resonances will have to be done by power electronic converters.

This work focuses on a frequency range between 2 kHz and 150 kHz which is the normative gap between the power quality standards and the EMI standards. Due to the trends in power electronics described above the number of switching or self commutated converters connected to the power grid is increasing and will continue to do so. Besides having to fulfill requirements concerning their low frequency current waveforms they also have to comply with EMI standards resulting in the application of EMI filters. The resonance frequencies of those filters as well as the switching frequencies of the converters are typically in the frequency range of 2 kHz to 150 kHz.

When selecting or designing an EMI filter it is made sure that the filter resonances can not be excited by the corresponding converter. In grids with many converters and EMI filters connected together it is unclear if a converter might excite a resonance of another EMI filter or a resonance between several filters and other consumers. Excitation of a resonance would lead to increased currents through the components or additional voltages at the components resulting in accelerated aging or even instant destruction of the components forming the resonance. Depending on the destroyed component and its fault state (open or short) the operation of the corresponding converter is no longer possible.

This work aims at analyzing the possibility for resonances when two power electronic converters are connected in parallel to the same supply. To do so a general introduction to grid connected power converters is given in chapter 2 as well as a description of the realized lab setup. Chapter 3 gives an overview of typical modeling methods used for the description and simulation of components in different frequency ranges and outlines the modeling method used in this work. The measurement procedures utilized as well as the resulting component models are described in chapters 4 and 5 respectively. Chapter 6 contains simulations of two converters with varying components and surroundings, in order to identify the key influences on the resonance. The findings of the simulation are verified by measurements in chapter 7 and finally a converter design aiming to solve the described problem is analyzed in chapter 8.

2 Grid Connected Converters

This chapter introduces the most typical designs of active infeed converters in section 2.1. Section 2.2 introduces the realized lab setup including the control structure of the designed converter.

2.1 Typical configurations of active infeed converters

In industrial environments the use of diode rectifiers to supply a drive or a set of drives is still dominant over the use of active infeed converters. Only if a drive generates enough braking energy which shall be fed back into the grid for efficiency reasons or connected loads have low tolerance for variation in DC-link voltage the higher price of active infeed converters is tolerated. In addition to the increase in price a decrease in efficiency of the active infeed converters over diode rectifiers has to be compensated.

Surveying the product portfolio of the biggest european industrial drives manufacturers reveals, that in case of industrial drives the grid interface of AICs is either realized using a grid inductor or an LCL filter. Both versions can be combined with an EMI-filter to be installed on the grid side of the inductor or LCL-filter.

In case of regenerative energies the connection to the grid is similar with significantly larger interest in solutions with LCL-filters. This is most likely due to their inherent feature of being able to provide grid supporting functionality, by actively controlling the capacitor voltage of the LCL-filter [PMCS14, GBM+15].

As an LCL filter introduces resonances into the system it is necessary to damp this resonance. Several options for active and passive damping are available. Damping passively is typically done by adding a resistor in parallel to the grid side inductance [CWZ+14, PST06, RT07] or in series with the capacitors [LBH05, WHTB13].

Since any damping resistor creates additional losses in a power system with LCL-filter it is undesirable. If the self resonance of the LCL-filter is well within the controller bandwidth of the circuit it can be actively damped [RT07, LZHL11]. The main advantage of active damping besides higher efficiency is that the filter retains its 3rd order damping property for a wider frequency range.

As LCL-filter capacitors are typically not connected to ground the filter acts only on DM components. Therefore an additional EMI filter is typically necessary to limit CM emissions.

2.2 Realized Lab Setup

Figure 2.1 shows the replacement circuit of the realized converter including the controller structure, which will be explained in detail in the coming subsection. The converter is connected to the grid through ferrite inductors to avoid the gradual saturation observable in many iron powder chokes. The DC side of the converter is supplied by a DC source which is connected to an independent AC system through an isolation transformer. The use of a well regulated DC source and the generation of symmetrical currents on the AC side allows for a rather small DC link capacitance of 80 μF.

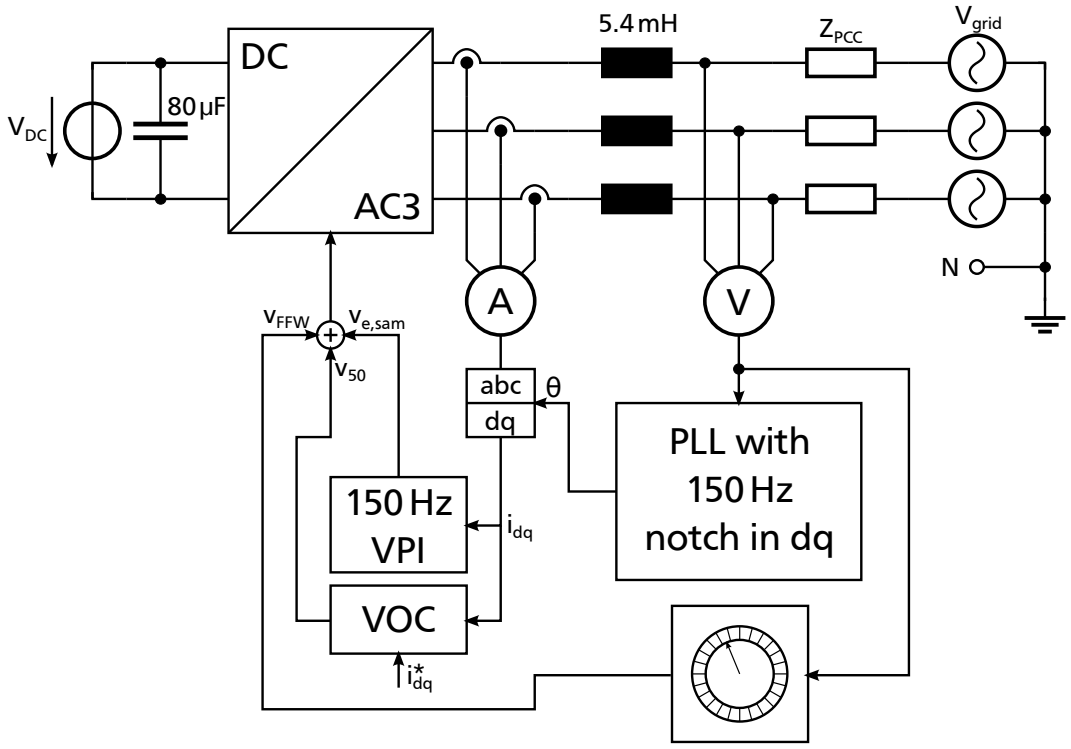

Figure 2.1.: Control structure and DM replacement circuit of the designed converter

2.2.1 Controller Design

In order to generate a wide spectrum of harmonic content the converter is designed to operate at any switching frequency between 2 kHz and 10 kHz. Additionally, the impedance at the point of common coupling is expected to be very variable depending on the additional loads connected. Both of those requirements result in additional challenges for the controller design.

To realize a simple way of adjusting the parameters of the controller to different switching frequencies, the parameters are calculated in a Matlab® script and transferred to the micro-controller via Matlab®'s external mode, which allows to change parameters during execution. The basic control algorithm used is the well known voltage oriented control (VOC) [KKB02]. The control parameters are calculated using the magnitude optimum method.

Typically VOC is supported by a classical voltage feed-forward loop. At 2 kHz the time delay between a sample and the feed-forward taking action is 1.5 samples or 750 μs which leads to a phase error of 13.5° for the 50 Hz component. This in turn leads to an error of 23.3 % relative to the grid voltage in the initial output voltage set by the converter at start up. Assuming a relative voltage drop of 8 % across the grid choke this would lead to a dynamic overcurrent at turn-on of almost three times the nominal current of the circuit. To avoid this problem a circular buffer is used and the value from the last period, taking into account the 1.5 samples delay, is used. This measure was found to improve both the turn-on behavior and the robustness against harmonic content in the grid voltage significantly.

Figure 2.2 shows the measured grid voltage of the converter for different grid impedances for single and double edge sampling. The figure shows that there is a strong influence of the grid impedance on

the sampled voltage of the controller. The different sampling errors and their influence on the controller are explained in the following paragraphs.

The first simulated impedance is equal to ten times the ohmic-inductive grid impedance measured in the laboratory grid. The switching pattern of the converter is clearly visible in the voltage it measures. Since this is an ohmic-inductive voltage divider, a similar result is expected if the converters power rating is increased and in turn the inductance of the grid choke decreased. The sampling error of single and double edge sampling contain only a 50 Hz component and are compensated easily by the controller.

The second row shows the voltages when using a LISN, which is described in section 5.4 in more detail. The sampling error shows a 100 Hz negative sequence component, which can be decreased by using double edge sampling. This sequence will turn into a 150 Hz component in dq reference frame, which a simple VOC can not control well.

Row three shows the converter when operated without a LISN but with additional differential mode capacitors connected to the PCC. An oscillation of the voltage of roughly 30 V peak to peak is now visible. The resulting sampling error consists mostly of a positive sequence component at 200 Hz. Double edge sampling does not significantly decrease this sampling error. Transformation to the dq-reference frame of the sampling error again results in a 150 Hz component.

Since the above operating points have to be used at the test bench while maintaining sinusoidal currents, the controller is improved to cancel those effects. Both effects turn into a 150 Hz component in dq-reference frame. Therefore the current controller is equipped with a vector proportional integral (VPI) controller, which places a damped pole at 150 Hz [BDL00, LABB07]. Additionally the signals in the PLL are filtered in dq-reference frame by a 150 Hz notch filter to avoid oscillation on the estimated angle of the grid voltage (see figure 2.1).

Figure 2.3 shows the harmonic currents resulting from different controller types at different switching frequencies. The controller labeled "“simple"” consists of a regular VOC with a feed forward of the previously measured values. The label "“improved"” corresponds to the improved controller structure shown in figure 2.1.

The following non-idealities were considered in the simulation:

- IGBT deadtime: 1 μs
- harmonics in grid voltage: 4 % of 5^{th} and 7^{th} harmonic
- grid frequency: 49.9 Hz
- grid connection through LISN and 2 μF DM capacitance at the PCC

The harmonics depicted in figure 2.3 are calculated well after the converter reaches steady state operation. A simple VOC feeds more current at the second harmonic into the grid than at the fundamental. Also the harmonic content at the harmonic numbers 4,5 and 7 are in the order of magnitude of the fundamental current. In time domain this current waveform is not recognizable as a 50 Hz current. When using the improved controller structure all mentioned harmonics are decreased significantly and regular operation is possible.

The simple controller works much better if the switching frequency is increased to 10 kHz. Also at this frequency a decrease of all harmonics is visible when using the improved control structure.

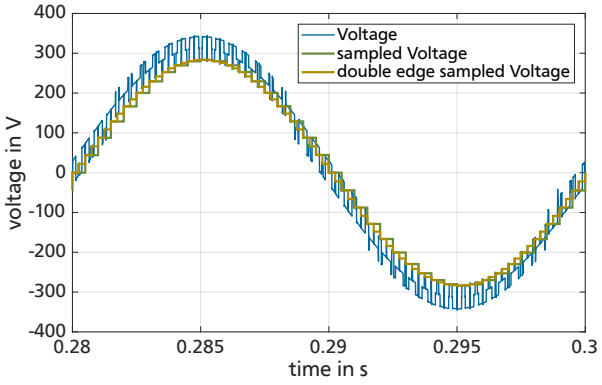

(a) tenfold grid impedance

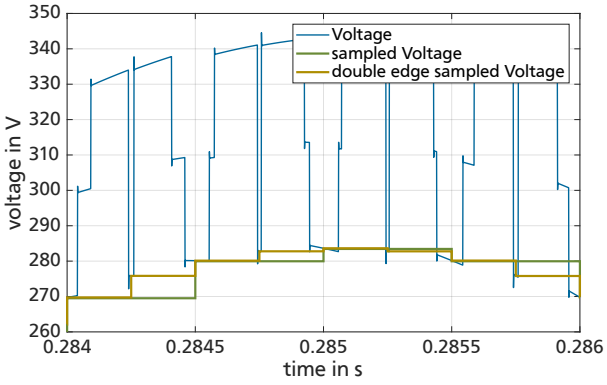

(b) tenfold grid impedance, zoom

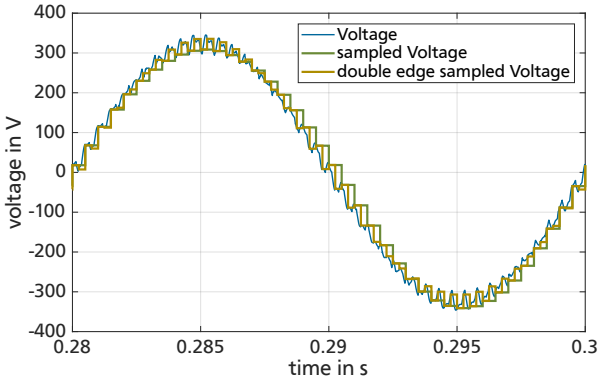

(c) LISN

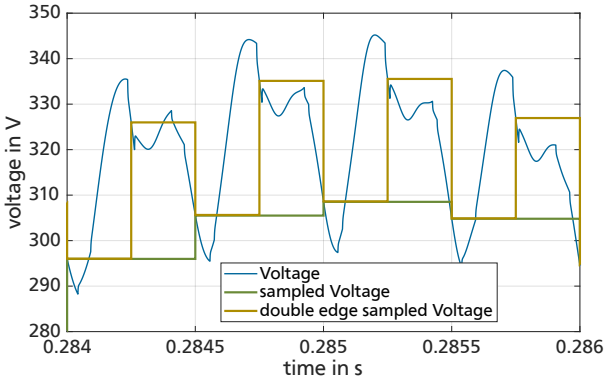

(d) LISN, zoom

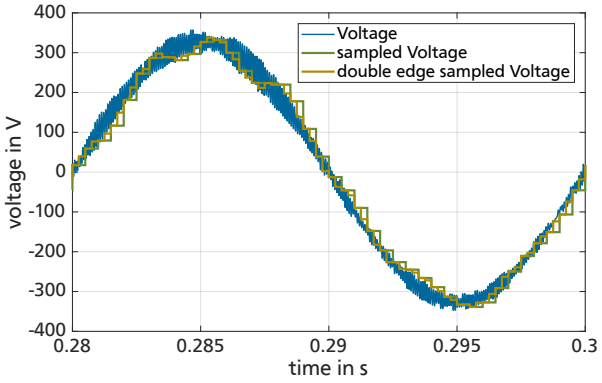

(e) 2 μF DM capacitance at PCC

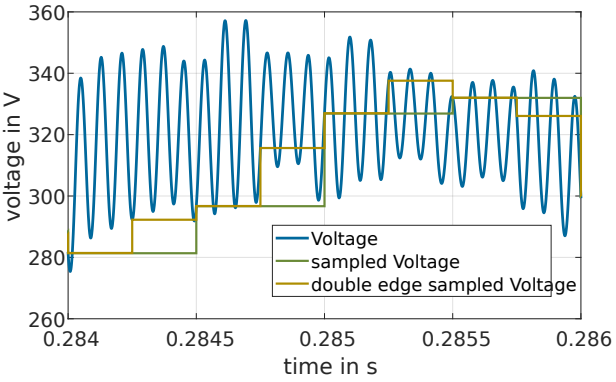

(f) 2 μF DM capacitance at PCC, zoom

Figure 2.2.: Effects of different grid impedances on the sampling results

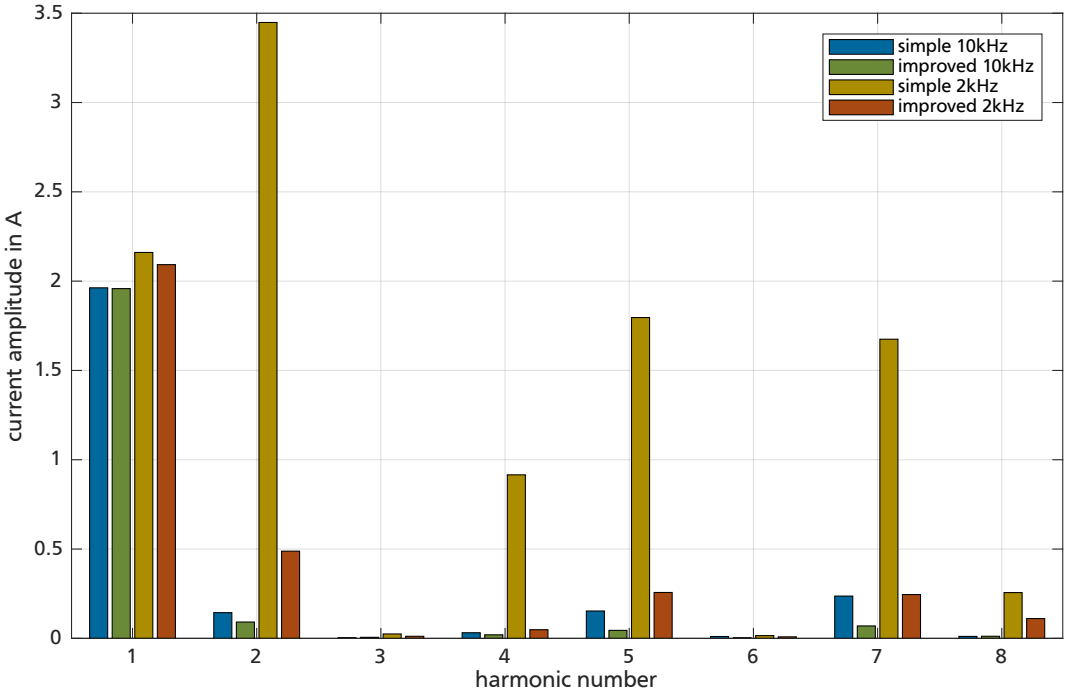

Figure 2.3.: Current harmonics for different switching frequencies and controllers

Using processor in the loop (PIL) execution profiling of the control algorithm on the used microcontroller (TI 28335) results in an execution time of 39.16 μs allowing switching frequencies of up to 25 kHz. The speed of the improved and therefore more complicated controller is still more than sufficient to allow the desired maximum switching frequency of 10 kHz.

2.2.2 Typical Common Mode Hardware Design

Figure 2.1 shows a converter hardware design ignoring the common mode paths. This is possible because an isolation transformer was used to supply the DC side shifting all possible CM resonances to frequencies well beyond any switching frequencies [1]. This is necessary to allow for a strong variation in switching frequency without significantly exciting a CM resonance within the converter.

A more typical approach for CM design of the circuit is to place the CM resonance of the converter above any relevant frequency components of the modulation technique and below the switching frequency. The resulting converter design with this CM strategy, incorporating an EMI-filter and capacitors to ground on the DC side is depicted in figure 2.4.

If the CM resonance is placed below the switching frequency the component mainly responsible for the amplitude of the common mode current at switching frequency is the choke of the converter. The current resulting from a value of 5.4 mH DM inductance and a CM voltage of 325 V at 10 kHz is 958 mA per phase. In order to reduce the CM current a CM choke is added in series resulting in 332 mA CM current per phase.

[1] For a converter model considering the CM path see section 5.5

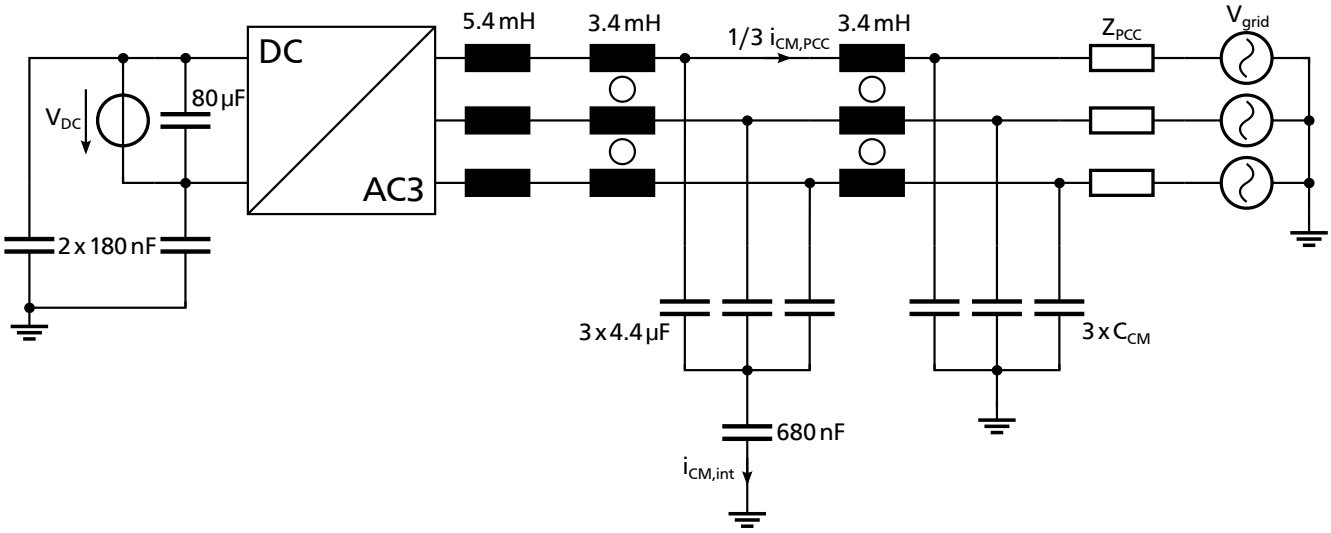

Figure 2.4.: Lab setup with common mode design for fixed switching frequency

Solving the series connection of the filter capacitors and CM capacitors on DC side results in a total CM capacitance of 231 nF which places the CM resonance at 4.59 kHz with the combined CM inductance L_{CM}.

$$L_{\mathrm{CM}} = \frac{5.4\,\mathrm{mH}}{3} + 3.4\,\mathrm{mH} = 5.2\,\mathrm{mH} \tag{2.1}$$

The CM choke on grid side decreases the CM currents flowing into the grid and decouples the CM resonance from any influence from the grid side. Figure 2.5 shows the transfer functions of CM currents fed into the grid per 1 V CM voltage generated by the converter and the CM currents resulting within the converter, labeled internal. Both are simulated with a grid impedance Z_{grid} of 80 μH and 30 mΩ. No significant influence when increasing the capacitance C_{CM} from PCC to ground from 1 μF to 100 μF is visible.

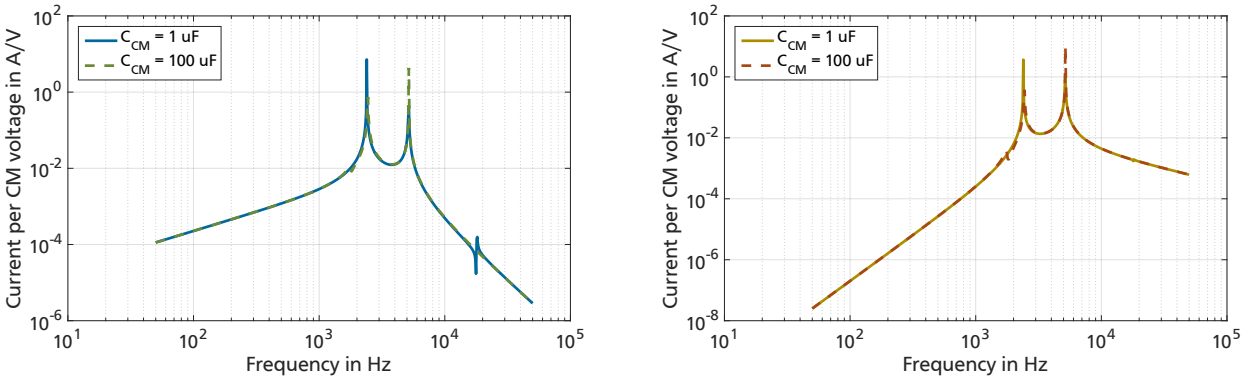

(a) PCC current $i_{\mathrm{CM,PCC}}$ **(b)** internal current $i_{\mathrm{CM,int}}$

Figure 2.5.: Internal and PCC CM currents of the designed converter

Figure 2.5 shows that the hypothetical CM design would lead to a converter which is very robust against any type of PCC impedance variation. The converter would therefore perform well in terms of CM, independent of loads or sources connected in parallel.

While this CM design would work well for a converter with a switching frequency of 10 kHz or more, the test setup is meant to adjust the switching frequency between 2 kHz and 10 kHz, which would result in destructively large currents and disqualifies this design for implementation. Decreasing the resonance frequency below 2 kHz would result in excessively large components.

3 Frequency Domain Simulation

This chapter introduces the typical modeling approaches in different frequency ranges and the advantages and drawbacks of those in section 3.2. The selected modeling approach for the considered range from 2 kHz to 150 kHz is described in that section as well. Since all approaches use multiport theory it is introduced in general in section 3.1. Finally in section 3.3 a functional outline of the developed simulation in Matlab is given.

3.1 Multiport Theory

Multiport theory as an extension to the widely used and taught theory of two-port networks is extensively described in several publications, such as [Kle76] and [AV06]. A short introduction based on those publications will be given in this section and the advantageous properties of the network parameters used throughout this work are described. The notation is chosen in accordance with the German standard regarding 2-port systems DIN 40148 [DIN78, DIN84, DIN71].

Each port of a multiport network consists of two terminals and is defined by two parameters. For electrical networks those two parameters are typically the voltage between the terminals and the current flowing into the input terminal and out of the output terminal. If two terminals are to form a port those two currents must be equal. The simplest form of a multiport network is the one-port network, which can be used to describe simple components with two terminals, such as resistors. In case of a resistor the port parameters voltage and current are linked through the resistance R.

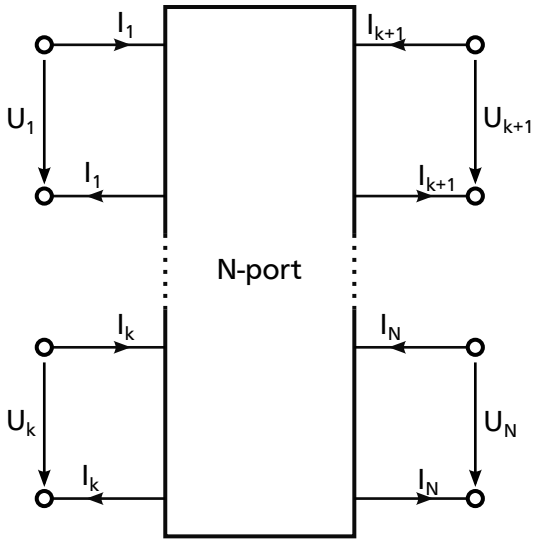

Figure 3.1.: General form of a multiport

Figure 3.1 shows the general form of a multiport with N ports. The 2N parameters can be linked using a N^{th} order matrix. Each parameter can be chosen as an independent or dependent parameter resulting

in 2^N different matrices, which can be transformed into one another by using linear algebra in case of non-singular matrices. Out of the 2^N matrices only two will be explained here in more detail as they have advantageous properties due to a certain symmetry in choosing the independent variables. In addition a third matrix linking different variables is presented.

Admittance Parameters Y

The admittance matrix $\mathbf{Y}$ describes the port currents in terms of the port voltages, such that:

$$\vec{I} = \mathbf{Y} \cdot \vec{U} \tag{3.1}$$

Figure 3.2 shows the parallel connection of two 2-ports marked as $\mathbf{Y}'$ and $\mathbf{Y}''$. The voltages applied to the terminals of both 2-ports are equal since $\vec{U}' = \vec{U}'' = \vec{U}$ and the sum of the currents is equal to total currents into the parallel connection $\vec{I}' + \vec{I}'' = \vec{I}$. Therefore the calculation of this network can be simplified to:

$$\vec{I} = \left(\mathbf{Y}' + \mathbf{Y}''\right) \cdot \vec{U} = \mathbf{Y} \cdot \vec{U} \tag{3.2}$$

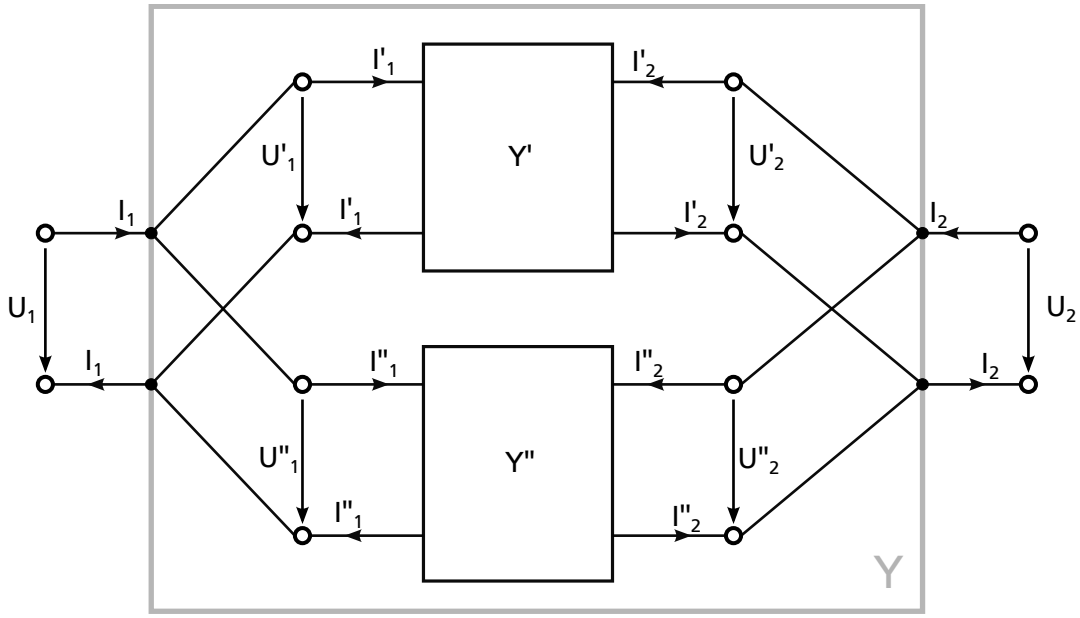

Figure 3.2.: Parallel connection of two 2-ports

The parallel connection of k N-ports can therefore easily be reduced to one N-port by summing up the admittance matrices.

$$\mathbf{Y} = \sum_k \mathbf{Y}_k \tag{3.3}$$

Chain Parameters A

The chain matrix relates a set of unknown port parameters to a set of independent and known port parameters:

$$\begin{bmatrix} \vec{U}_1 \\ \vec{I}_1 \end{bmatrix} = \mathbf{A} \cdot \begin{bmatrix} \vec{U}_2 \\ \vec{I}_2 \end{bmatrix} \tag{3.4}$$

Chain parameters therefore allow the determination of parameters at output ports depending on the values at input ports. The main application of those parameters is therefore a chain connection of several N-ports shown in figure 3.3 for two 2-port networks. In case of the chain matrix the current direction of the secondary side ports is reversed from the general definition in figure 3.1 in accordance with DIN 40148 [DIN78].

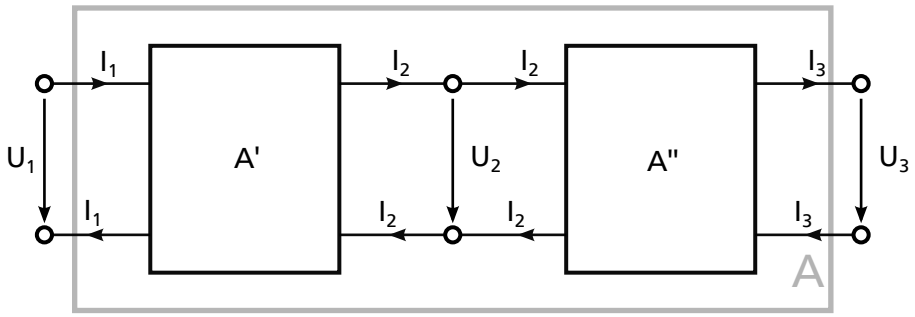

Figure 3.3.: Chain connection of two 2-ports

The chain connection in figure 3.3 can be simplified by applying (3.4) to both 2-ports and combining the two formulas through I_2 and U_2 resulting in:

$$\begin{bmatrix} U_1 \\ I_1 \end{bmatrix} = \mathbf{A}' \cdot \mathbf{A}'' \begin{bmatrix} U_3 \\ I_3 \end{bmatrix} \tag{3.5}$$

In the same manner the chain connection of k N-ports can always be simplified by multiplication of their chain matrices.

$$\mathbf{A} = \prod_k \mathbf{A}_k \tag{3.6}$$

Scattering Parameters S

Figure 3.4 shows the structure of a general N-port which has been extended by a voltage source and impedance per port. Since any combination of sources and passive impedances can be simplified as a voltage source with internal impedance this extension does not restrict the applicability of the general N-port in scattering parameters compared to the general N-port in figure 3.1.

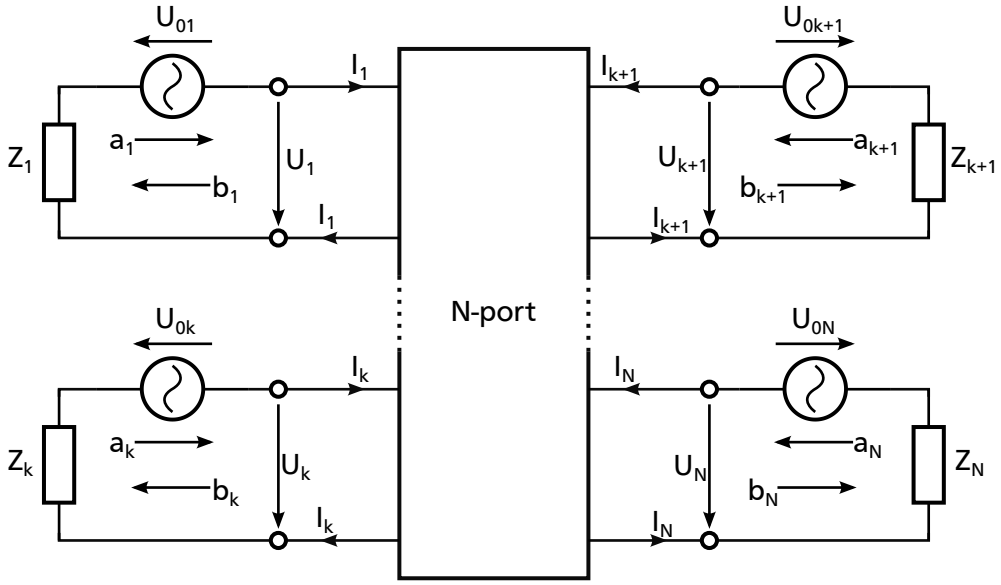

Figure 3.4.: General N-port with external wiring for scattering parameters

Rather than currents and voltages the scattering parameters **S** link the scattering variables $\vec{a}$ and $\vec{b}$ [1] by multiplication:

$$\vec{b} = \mathbf{S} \cdot \vec{a} \tag{3.7}$$

With the scattering parameters being [Kle76]:

$$a_i = \frac{U_i + Z_i \cdot I_i}{2 \cdot \sqrt{Z_i}} = \frac{U_{0i}}{2 \cdot \sqrt{Z_i}} \tag{3.8}$$

$$b_i = \frac{U_i - Z_i \cdot I_i}{2 \cdot \sqrt{Z_i}} \tag{3.9}$$

In case the impedance of all ports is purely resistive the real power flowing into the considered port simplifies to (3.10) with $|a_i|^2$ being the maximal power the source U_{0i} can induce into port i and $|b_i|^2$ the part of the power which is reflected back from the ith port plus the powers transferred from all other ports to port i.

$$P_i = |a_i|^2 - |b_i|^2 \tag{3.10}$$

[1] DIN 40148 labels the scattering variables with the letters 'M' and 'N'. Since this is neither commonly used in English nor German anymore, the common notation as 'a' and 'b' is used here.

Knowing the S-parameters of an N-port the power balance of each port can be determined by superposition using (3.7):

$$P_i = |a_i|^2 - \left| \sum_k a_k \cdot S_{ik} \right|^2 \tag{3.11}$$

Each S-parameters is therefore a measure of the power transferred from one port to another.

Conversion between admittance and chain parameters

Components in AC transmission systems typically have an even amount of ports as the component connects to the same amount of lines on both sides. Therefore (3.1) can be rewritten by using one subset of ports per component side and four quadrants of the admittance matrix [Kle76]:

$$\vec{I}_1 = \mathbf{Y}_{11} \cdot \vec{U}_1 + \mathbf{Y}_{12} \cdot \vec{U}_2 \tag{3.12}$$
$$\vec{I}_2 = \mathbf{Y}_{21} \cdot \vec{U}_1 + \mathbf{Y}_{22} \cdot \vec{U}_2 \tag{3.13}$$

Dividing the chain matrix (3.4) using the two subgroups leads to:

$$\vec{U}_1 = \mathbf{A}_{11} \cdot \vec{U}_2 + \mathbf{A}_{12} \cdot \vec{I}_2 \tag{3.14}$$
$$\vec{I}_1 = \mathbf{A}_{21} \cdot \vec{U}_2 + \mathbf{A}_{22} \cdot \vec{I}_2 \tag{3.15}$$

Solving (3.13) for $\vec{U}_1$ leads to the format of (3.14) and inserting it into (3.12) leads to an equation in the form of (3.15). This allows to determine the chain parameters from the admittance parameters by comparison of the coefficients resulting in [Kle76]:

$$\begin{bmatrix} \mathbf{A}_{11} & \mathbf{A}_{12} \\ \mathbf{A}_{21} & \mathbf{A}_{22} \end{bmatrix} = \begin{bmatrix} -\mathbf{Y}_{21}^{-1} \cdot \mathbf{Y}_{22} & -\mathbf{Y}_{21}^{-1} \\ \mathbf{Y}_{12} - \mathbf{Y}_{11} \cdot \mathbf{Y}_{21}^{-1} \cdot \mathbf{Y}_{22} & -\mathbf{Y}_{11} \cdot \mathbf{Y}_{21}^{-1} \end{bmatrix} \tag{3.16}$$

Rearranging for the admittance parameters in terms of the chain parameters leads to [Kle76]:

$$\begin{bmatrix} \mathbf{Y}_{11} & \mathbf{Y}_{12} \\ \mathbf{Y}_{21} & \mathbf{Y}_{22} \end{bmatrix} = \begin{bmatrix} \mathbf{A}_{22} \cdot \mathbf{A}_{12}^{-1} & \mathbf{A}_{21} - \mathbf{A}_{22} \cdot \mathbf{A}_{12}^{-1} \cdot \mathbf{A}_{11} \\ -\mathbf{A}_{12}^{-1} & \mathbf{A}_{12}^{-1} \cdot \mathbf{A}_{11} \end{bmatrix} \tag{3.17}$$

Reciprocal Networks

A reciprocal network has the property that power transmission between two ports is equal independent of the direction of power transfer [Kle76]. Typical, but not all, passive components and combinations

of those fulfill this property whereas most active circuits do not. For the basic passive components used in power electronics (resistance, inductance, capacitance, mutual inductance) the matrices have the following special properties that are helpful when setting up a component model (see chapter 4).

$$\mathbf{S} = \mathbf{S}^T \tag{3.18}$$

$$\mathbf{Z} = \mathbf{Z}^T \tag{3.19}$$

$$\mathbf{Y} = \mathbf{Y}^T \tag{3.20}$$

$$\det(\mathbf{A}) = 1 \tag{3.21}$$

3.2 Approaches for different frequency ranges

The frequency span from 2 to 150 kHz considered in this work is framed between two frequency spans in which emission levels and the measurement of those levels are standardized. Before introducing the concepts utilized in this work in subsection 3.2.3 the approaches in the frequency range of power quality (subsection 3.2.1) and electromagnetic interference frequency range (subsection 3.2.2) are discussed.

3.2.1 Power Quality Frequency Range (<2-9kHz)

In 1918 Fortescue [For18] introduced the theory to transform n harmonic values into n different sequences which are independent of each other and used these sequences for the description and calculation of three phase asynchronous machines. Later, in the 1940's this concept was applied to three phase power networks by Lyon [Lyo40] and has since then been frequently used for the description of three phase power systems as it allows for the calculation as a single phase network under common circumstances.

Fortescue [For18] introduces a complex factor α that rotates any vector by the n^{th} part of 2π. Using this factor to build vectors $\vec{B}_k$ the k^{th} sequences of a given set of phase values (here: voltage $\vec{U}$) can be determined:

$$\alpha = e^{\mathrm{j}\cdot\frac{2\pi}{n}} \tag{3.22}$$

$$U_k = \vec{B}_k \cdot \vec{U} = \frac{1}{n}\left(\alpha^{0k}, \alpha^{-k}, \alpha^{-2k}, \ldots \alpha^{-(n-1)k}\right) \cdot \vec{U} \tag{3.23}$$

To maintain equal amplitudes through transformation, the vector $\vec{B}_k$ contains a scaling factor $\frac{1}{n}$. Writing all sequences as a vector U_{seq} the transformation can be expressed using the matrix $\mathbf{B}$.

$$\vec{U}_{\mathrm{seq}} = \mathbf{B} \cdot \vec{U} \tag{3.24}$$

Applying equations (3.22) through (3.24) to a three-phase system results in the well known form (3.25), where U_0 is the zero sequence component, U_1 the positive sequence component and U_2 the negative sequence component. The exponents of α in (3.25) have been adjusted compared to (3.23) using the property $\alpha^n = 1$.

$$\begin{bmatrix} U_0 \\ U_1 \\ U_2 \end{bmatrix} = \frac{1}{3} \cdot \begin{bmatrix} 1 & 1 & 1 \\ 1 & \alpha^2 & \alpha \\ 1 & \alpha & \alpha^2 \end{bmatrix} \cdot \begin{bmatrix} U_a \\ U_b \\ U_c \end{bmatrix} \tag{3.25}$$

The main advantages of this transformation are the following:

1. If all impedances are symmetrical a voltage of a certain sequence only creates current of that same sequence and vice versa.

2. If the phase voltages or currents are ideal sinusoids with equal amplitude and 120° phase shift only the positive sequence component exists. Zero sequence and negative sequence are equal to zero.

If the assumptions of symmetrical impedances and electrical values in the network are appropriate a three phase systems can be reduced from a six port to a two port, significantly reducing the calculation effort and allowing for manual calculation. In case of non-ideal electrical values systems still reduces to three separate systems of two-ports excited by the respective electrical sequences.

In case of unsymmetrical impedances however those three systems are coupled such that voltages of one sequence excite currents of all three sequences and vice versa. Since time domain simulation can still be done well in this low frequency range such cases are typically not calculated in frequency domain but rather in time domain.

3.2.2 Modeling approaches above 150 kHz

In the frequency range above 150 kHz similar assumptions are made as in subsection 3.2.1. The network impedances are assumed to be symmetrical allowing the consideration as two-ports. One two-port system is used to model the transmission of common mode (CM) emissions and another to model differential mode (DM) emissions. Comparing the definition of common mode voltage U_{CM} in (3.26) to the first line in (3.25) reveals that it is equal to the zero sequence U_0 previously introduced.

$$U_{CM} = \frac{U_a + U_b + U_c}{3} \tag{3.26}$$

The differential mode component must therefore describe the reaction of the circuit to positive and negative sequence components. The fact that those two components are described by only one component in this frequency domain illustrates three characteristics of the analysis within this frequency range:

1. The impedances are considered to be purely passive, therefore any difference in impedance for positive or negative frequencies due to the rotation of machines or influences of control algorithms[2] are neglected.

2. Power emitted at a given frequency is considered rather than sequence, voltage and current at that frequency.

3. Measurement results are acquired using specified port impedances, typically 50 Ω, and can't be easily transferred to cases with different impedances.

3.2.3 Considered Frequency Range (2-150 kHz)

Todays switching frequencies are typically located between the two ranges described above. Due to missing normative requirements imposed on power electronic circuits within this considered frequency range there is no modeling or calculation method in this frequency range that can be considered the standard. Some of the typical approaches to model power electronic components in this range are circuit simulators which run time domain simulations such as Matlab® Simulink®, Plecs® or GeckoCIRCUITS. Since accurate representation of the switched waveforms requires a significantly larger sampling rate which is directly proportional to simulation time the converters can be replaced by a behavioral model as a controlled current source reducing the bandwidth of the analysis to the bandwidth of the control structures considered. Passive effects due to switching waveforms are neglected by this method.

The requirements for the simulation within this work are:

- high simulation speed
- consideration of non symmetrical sources and components
- consideration of switched waveforms

The first requirement imposes the necessity for a frequency domain simulation, the second requirement eliminates the possibility of decreasing the order of the considered components by splitting the signals into sequences or modes as introduced in the preceding subsections.

Since the bandwidth of modern sampled measurement equipment is more than sufficient to measure frequencies up to 150 kHz this work uses an approach with chain, impedance and admittance rather than scattering parameters which would require much more complicated measurement equipment especially at low frequencies[3].

To allow the simulation of both three phase and single phase components all simulations include the neutral line resulting in a total of four lines whose currents and voltages against protective earth form 8-ports for components with connectors on both sides.

Figure 3.5 shows a general structure of 8-ports connected to a point of common coupling (PCC) where one 8-port represents the interface to the power grid and N 8-ports represent N different converters. The

[2] The impedance of a power converter connected to the grid can be shaped within the controller bandwidth using the concept of virtual impedance [YLY+16, SMR12, CMB17].

[3] Typical measurement equipment for scattering parameters is designed for frequencies in the range of GHz and powers of few W and is not suited to measure large signals at frequencies close to the superimposed and much larger grid voltage.

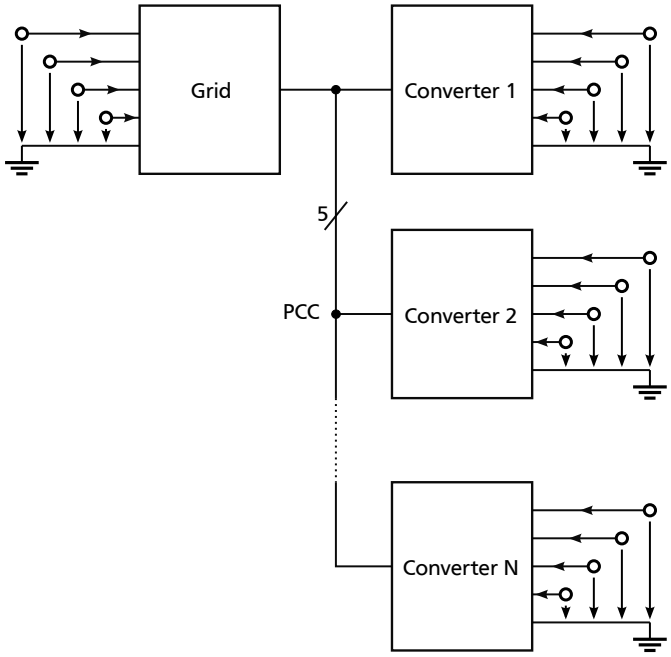

Figure 3.5.: General Structure of a low voltage system with converters connected

system in figure 3.5 is essentially a multiport of the order $4 \cdot (N+1)$ and could be represented using any of the above introduced matrices of this order. If half of the port quantities are known all others can be determined. However this calculation procedure is not feasible as the setup of the matrices becomes more complex with increasing size. For example to set up an admittance matrix one would need to express the current flowing into port 4 of the N^{th} converter in terms of the voltage at terminal 1 of the 1^{st} converter with all other voltages being equal to zero. Considering the amount of parallel paths in this network the manual determination of this expression becomes impossible. Section 3.3 introduces a way to solve a network as shown in figure 3.5 by using only the 8-ports of the separate components for calculation.

3.3 Simulation: Functional Outline

Since frequency domain simulation assumes all components show linear behavior the concept of superposition can be used without any further constraint to the solution. Superposition assumes that the effect of each source in the network can be calculated individually and those effects can be added if a combination of sources is active. The diagram from figure 3.5 can be adjusted as done in figure 3.6 where all voltages except for the voltages at Converter 1 are shorted to ground and therefore equal to zero. Since the nodes G and 2 through N are now connected through ground it becomes clear that the grid and converter 2 through N are connected in parallel between the PCC and ground. By determining the admittance of this parallel connection $\mathbf{Y}_{\text{par}}$ in series with the admittance of converter 1 ($\mathbf{Y}_1$) the

current flowing into the network from converter 1 can be calculated using the resulting total admittance $\mathbf{Y}_{\text{tot}}$.

$$\begin{bmatrix} I_1 \\ I_2 \\ I_3 \\ I_4 \end{bmatrix} = \mathbf{Y}_{\text{tot}} \cdot \begin{bmatrix} U_1 \\ U_2 \\ U_3 \\ U_4 \end{bmatrix} \tag{3.27}$$

The calculation of $\mathbf{Y}_{\text{tot}}$ is done by transforming the admittance matrices to chain matrices and multiplying them since they are connected in series as introduced in section 3.1.

$$\mathbf{A}_{\text{tot}} = \mathbf{A}_1 \cdot \mathbf{A}_{\text{par}}^{-1} \tag{3.28}$$

When multiplying chain matrices the defined direction of the currents has to be considered in order to comply with figure 3.3 and equation (3.5). If the direction of the currents entering into converter 1 in figure 3.6 is to be kept, the current definition in all other components has to be flipped to form a circuit according to figure 3.3. This can be considered by using the inverse chain matrix of the parallel connected components $\mathbf{A}_{\text{par}}^{-1}$.

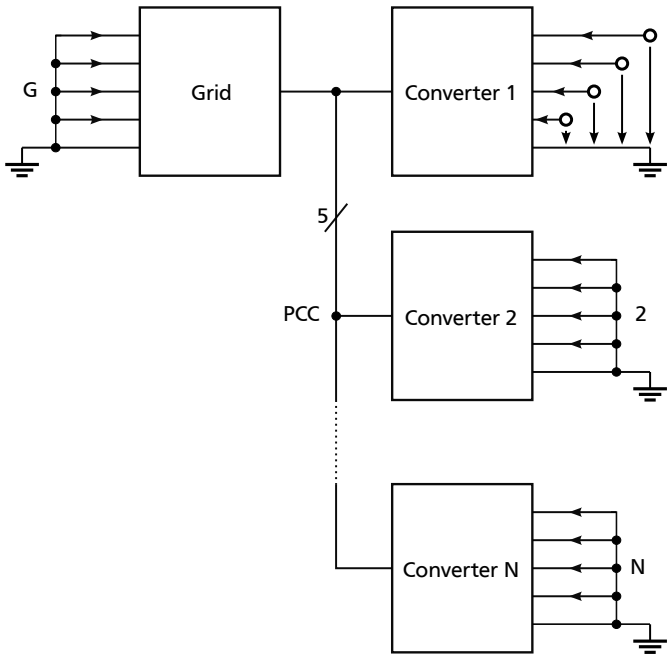

Figure 3.6.: LV grid structure with only one excitation

Now that the currents into the network at converter 1 are known the resulting currents and voltages throughout the network can be calculated. In the first step the voltages at the PCC and the currents into it due to converter 1 can be calculated.

Using the voltages at the PCC the currents into each converter and into the grid can be calculated using the admittances of each of the branches.

Using the above described concepts also more complex networks with more branches and subbranches than in this example can be calculated in the same manner. However the simulation so far can only handle grids in a tree structure. A ring structure can not be solved.

When all voltages and currents throughout the network are known the results can be analyzed. In this work the excitation from the converters was always simulated through the whole considered frequency band with a constant amplitude of 1 V. Due to linearity a current of interest anywhere within the network can be determined from a specter at a converter by scaling the results of the per unit calculation by the amplitudes of the voltage specter of interest.

Functional limits of the simulation

Due to the above described nature of the simulation the following limits of it have to be considered when using it:

- All components are assumed to behave linearly.
- The component models have to be determined using a common ground as reference.
- Only grids resembling a tree structure can be calculated.

4 Component Measurement

The component measurements are carried out in two different ways depending on the nature of the component. If the component is a true 8-port with connections on both sides such as cables or the filter and choke shown in figure 4.1 their measurement is performed passively meaning when they are disconnected from all surrounding components and there is no voltage present. The measurement procedure is described in section 4.1.

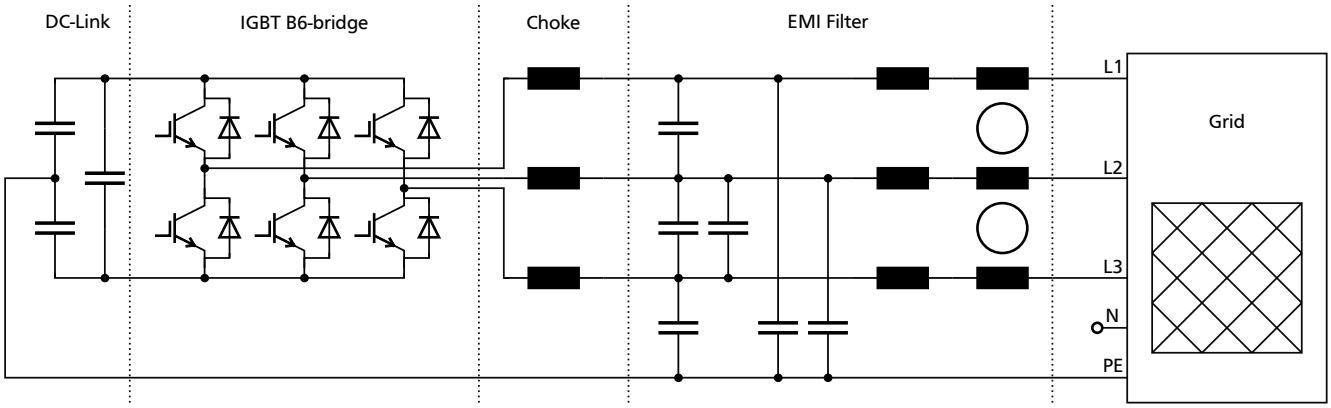

Figure 4.1.: Typical components of a converter

The IGBT bridge of the converter as well as the power grid can not be considered and measured as passive components. Since the power grid as shown in figure 4.1 is a 4-port and the IGBT bridge can be considered a 5-port (3-port on the AC side and 2-port on the DC side) dedicated measurement procedures have to be designed. Also the behavior of the components can only be measured accurately when they are active, therefore the measurement procedure has to be able to handle 230 V at 50 Hz. The selected approach is described in section 4.2.

4.1 Passive Components

The measurements of the passive components are carried out when they are disconnected from the grid and are performed using a low frequency network analyzer E5061B from Keysight Technologies which allows measurements between 5 Hz and 3 GHz. Since the maximum power of the measurement signals can be set to 0 dBm which is equal to 1 mW, all measurement results are small signal results. Especially the values of inductors can change drastically when they are operated at their rated current value, due to the beginning of saturation, resulting in different small signal behavior than measured without any additional large-signal component. This effect is ignored in this work but is discussed by the author in a dedicated publication [BG16].

Two measurement approaches have been tested during this work. The first approach is to measure either the admittance or the impedance matrix of a component. The result is a black-box model. This

approach and its downsides are discussed in subsection 4.1.1. The second approach is to assume a replacement circuit, expected to model the component well, and determine the values within this replacement circuit by measurement. Subsection 4.1.2 introduces this concept that shows good results in case the physics of a component is well known in the considered frequency range.

4.1.1 Measurement of impedance and admittance matrices

Figure 4.2 shows the measurement setup to determine the parameters of the impedance matrix of a device under test (DUT). In the figure an ideal three-phase inductor whose housing can be connected to protective earth is used as the device under test. The remaining components resemble the internal structure of the used network analyzer.

The voltage source U has an internal resistance of $50\,\Omega$. The actual output voltage of the network analyzer is measured at port R across a $1\,\mathrm{M}\Omega$ resistor. At port T of the network analyzer the voltage across a $50\,\Omega$ resistor is measured in order to determine the current through the DUT. The impedance phasor $\vec{Z}$ is automatically calculated by a vector[1] network analyzer (VNA) according to equation (4.1).

$$\vec{Z} = 50\,\Omega \cdot \frac{\vec{U}_\mathrm{R} - \vec{U}_\mathrm{T}}{\vec{U}_\mathrm{T}} \tag{4.1}$$

Equation (4.1) allows an error analysis of the measurement using a VNA by considering the two following critical cases.

1. $\vec{U}_\mathrm{T}$ is small and in the range of non-deterministic measurement errors of the VNA that can not be compensated by calibration. As $\vec{U}_\mathrm{T}$ becomes small for large impedances of the DUT this case limits the maximum impedance which can be measured.

2. $\vec{U}_\mathrm{T}$ is similar to $\vec{U}_\mathrm{R}$ and the difference in (4.1) becomes small. If this difference is within the range of measurement errors the resulting error in the calculated impedance is large. This is the case if the impedance of the DUT is small resulting in a minimal measurable impedance.

The used VNA limits the impedance to more than $7\,\Omega$ and up to $15\,\mathrm{k}\Omega$ to stay within 10 % error in the frequency range, considered in this work.

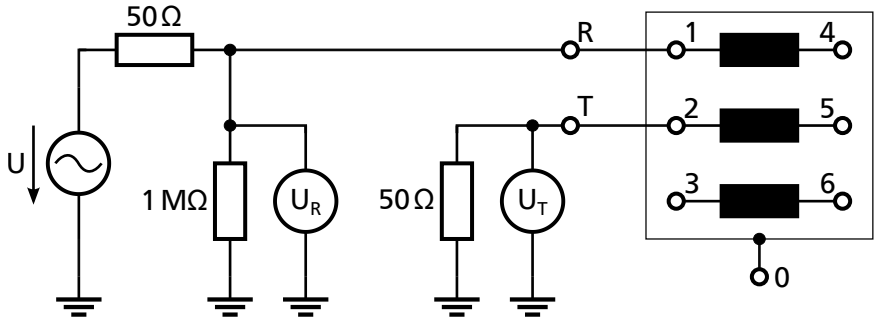

Figure 4.2.: Setup for the measurement of impedance matrices

[1] a regular network analyzer would only determine the amplitude of the impedance without any phase information

The DUT in figure 4.2 is a 6-port with a common reference node labeled 0. In order to measure impedance parameters the currents into the ports must be defined. The easiest way to acchieve this is applying only one current to two terminals and leaving all others open. In the case depicted in figure 4.2 the measured current I_{m12} and measured voltage across the DUT U_{m12} can be expressed in terms of the port parameters of port 1 and 2:

$$I_{\mathrm{m12}} = I_1 = -I_2 \tag{4.2}$$

$$U_{\mathrm{m12}} = U_1 - U_2 \tag{4.3}$$

Multiplying the port currents with the impedance matrix the port voltages can be written in terms of the measured current:

$$\begin{bmatrix} U_1 \\ U_2 \\ U_3 \\ U_4 \\ U_5 \\ U_6 \end{bmatrix} = I_{\mathrm{m12}} \cdot \begin{bmatrix} Z_{11} - Z_{12} \\ Z_{21} - Z_{22} \\ Z_{31} - Z_{32} \\ Z_{41} - Z_{42} \\ Z_{51} - Z_{52} \\ Z_{61} - Z_{62} \end{bmatrix} \tag{4.4}$$

Combining equations (4.3) and (4.4) leads to:

$$\frac{U_{\mathrm{m12}}}{I_{\mathrm{m12}}} = Z_{11} - Z_{12} - Z_{21} + Z_{22} \tag{4.5}$$

In case the terminal T of the NWA is connected to pin 0 of the DUT the measured current I_{m10} and the measured voltage U_{m10} are equal to the port parameters of port 1. The diagonal elements of the impedance matrix can therefore be measured directly:

$$Z_{\mathrm{m10}} = Z_{11} \tag{4.6}$$

The non-diagonal elements can be calculated in case of a reciprocal network ($\mathbf{Z} = \mathbf{Z}^{\mathrm{T}}$) from equation (4.5) using the measured diagonal elements:

$$Z_{\mathrm{ij}} = Z_{\mathrm{ji}} = \frac{Z_{\mathrm{ii}} + Z_{\mathrm{jj}} - Z_{\mathrm{mij}}}{2} \tag{4.7}$$

Alternatively, the admittance parameters can be measured. Figure 4.3 shows the measurement setup to determine the first diagonal element of the admittance matrix Y_{11}. All port voltages except U_1 are zero and the measured current of the NWA is equal to the port current I_1 so one can simply write:

$$Y_{\mathrm{m11}} = \frac{i_{\mathrm{m11}}}{u_{\mathrm{m11}}} = \frac{I_1}{U_1} = Y_{11} \tag{4.8}$$

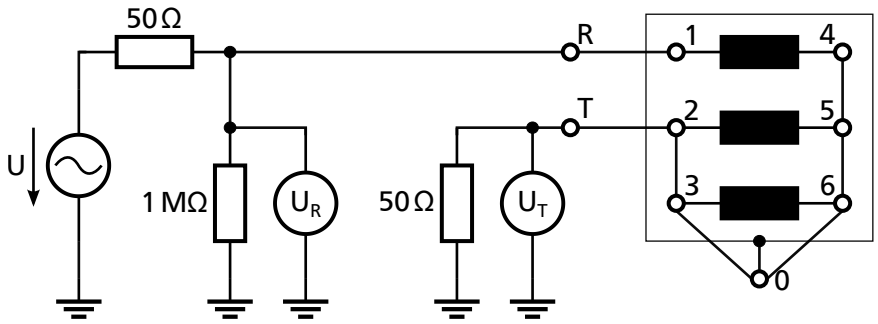

Figure 4.3.: Measurement setup of diagonal entries of the admittance matrix

Figure 4.4 shows the measurement setup used to determine non-diagonal components. As in case of the diagonal components of the impedance matrix two independent variables are set to the same amplitude, namely: $U_{\mathrm{m14}} = U_1 = U_4$ Again two dependent variables are related to a measured value as a sum: $I_{\mathrm{m14}} = I_1 + I_4$

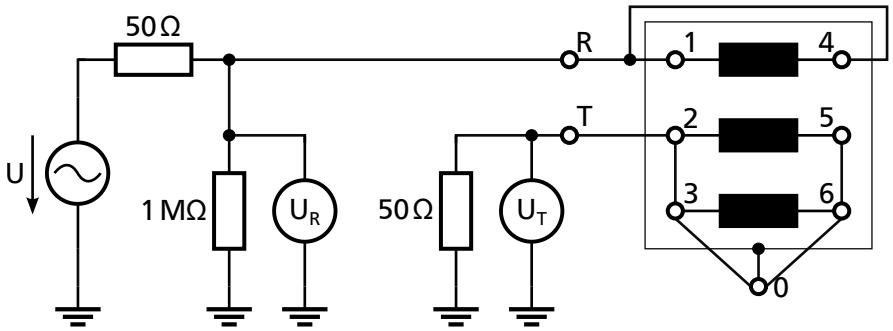

Figure 4.4.: Measurement setup of non-diagonal entries of the admittance matrix

Inserting above relations into the general form of the admittance parameters (3.1) leads to (4.9).

$$I_{\mathrm{m14}} = U_{\mathrm{m14}} \cdot (Y_{11} + Y_{14} + Y_{41} + Y_{44}) \tag{4.9}$$

In case of reciprocal networks ($\mathbf{Y} = \mathbf{Y}^{\mathrm{T}}$) the non-diagonal components are equal and can be calculated from the diagonal components and the measurement:

$$Y_{14} = Y_{41} = \frac{Y_{\mathrm{m14}} - Y_{11} - Y_{44}}{2} \tag{4.10}$$

Either of the above measurement strategies could be used to determine blackbox models of components. Implementing the strategies however comes with several limitations relevant in this work:

- The measurement examples in figures 4.2 and 4.4 would return an infinite impedance for ideal power components. For real components the measured impedance would be smaller than infinite due to parasitic capacitance to ground, however still much larger than the limit of the NWA of 15 kΩ to stay within the 10 % error band for the considered frequency range.
- Both procedures are only possible if the reference node is common to all ports as the housing in above example which is connected to PE. In case of a cable with PE on one side and PE' on the other separated by an impedance as reference nodes for the respective sides of the cable the above procedure does not work anymore.
- When using a blackbox model it is far from trivial to change component parameters to determine their influence on effects under investigation.

4.1.2 Generating port parameters from measurements

Considering the limitations described in subsection 4.1.1 it appears beneficial to generate a replacement circuit of a component first and subsequently generate its port representation.

The major downside of this technique is that the structure of a component has to be known in order to model it. Also all relevant nonidealities have to be known and modeled accurately within the considered frequency range. All considered power electronic components were found to be well resembled by replacement circuits of moderate complexity in the considered frequency range (see chapter 5) resulting in simple determination of good replacement circuits with this method.

Reconsidering the example of the parasitic capacitance to PE of a line choke the advantage of generating a replacement circuit becomes obvious. Instead of measuring the complete frequency range of interest the parasitic capacitance can be measured at frequencies where its impedance is within the range for good measurement accuracy. If the impedance is still too large or doubts about the accuracy remain for other reasons the influence of a change in parasitic capacitance can be easily determined by adjusting the measured value in the replacement circuit.

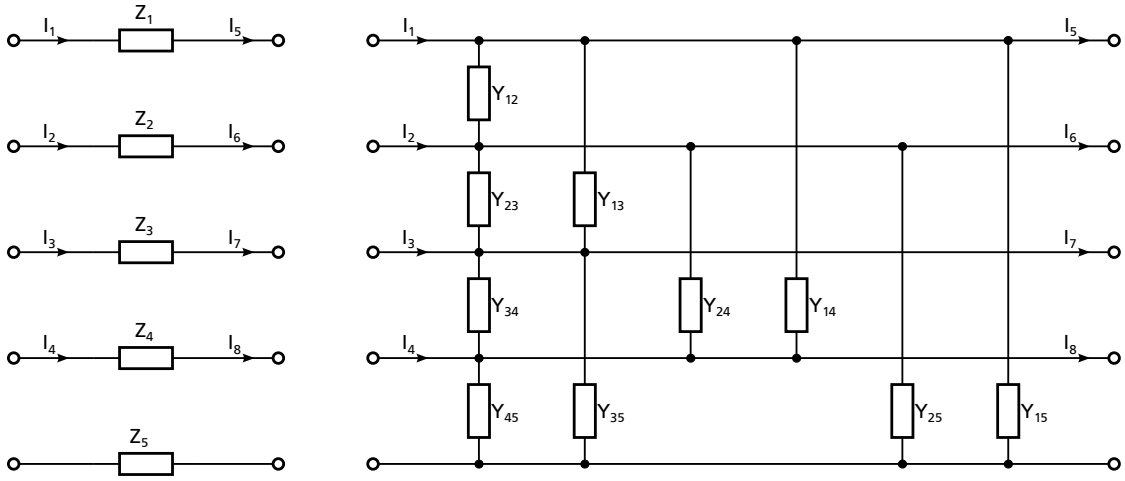

(a) series **(b)** shunt

Figure 4.5.: Basic generalized sub-circuits of power components

All typical power components can be modeled as combinations of basic 8-port series impedance elements and shunt admittance elements. Both are depicted in figure 4.5 in a generalized form, where the impedances and admittances can represent any interconnection of resistances, capacitances, inductances and mutual inductances. The port currents are defined according to the convention for chain matrices introduced in section 3.1, the eight port voltages defined to the reference node on the corresponding side are omitted from the figure to improve readability.

In case of the series sub-circuit the currents through each set of opposing ports must be equal according to Kirchhoffs current law. In case of the shunt sub-circuit the voltages on both sides are always equal since there is no series component generating a voltage drop. The chain matrices of both sub-circuits therefore only contain elements depending on the circuits components in one quadrant each. The other quadrants can be represented using the fourth order identity $\mathbf{I}_4$ and zero matrix $\mathbf{O}_4$

The bottom half of (4.11) describes the primary side currents in terms of the secondary side currents and voltages of the generalized series replacement circuit. The 4^{th} order zero matrix describes that there is no influence of the voltage on the currents and the 4^{th} order identity matrix sets the primary and secondary currents equal. The top half of the equation describes the effect of the secondary side currents and voltages on the primary side voltages. The voltage U_1 is larger than U_5 by the current I_5 times the impedance Z_1. Additionally each current flowing through one of the four lines creates a voltage drop across the impedance Z_5 as the port currents always have to return through their respective reference node (see chapter 3). This results in the first line of (4.11), which can be derived for the other three lines equivalently.

$$\mathbf{A}_{\text{series}} = \left[\begin{array}{c|cccc} \mathbf{I}_4 & \begin{matrix} Z_1+Z_5 & Z_5 & Z_5 & Z_5 \\ Z_5 & Z_2+Z_5 & Z_5 & Z_5 \\ Z_5 & Z_5 & Z_3+Z_5 & Z_5 \\ Z_5 & Z_5 & Z_5 & Z_4+Z_5 \end{matrix} \\ \hline \mathbf{O}_4 & \multicolumn{4}{c}{\mathbf{I}_4} \end{array}\right] \tag{4.11}$$

Applying an ideal differential mode signal to the first three lines (L1 through L3) and no signal to the fourth (neutral) line the influence of the impedance in the reference (PE) path Z_5 looses its influence and is therefore a common mode impedance. Modeling common mode inductors can therefore be done easily using this method by adding an equal inductance to the corresponding fields in the chain matrix. An ideal three phase common mode choke can be modeled by adding its common mode impedance to each field of the 3x3 sub-matrix starting at index (1;5).

In (4.13) the top half expresses the dependencies of the primary side voltages of the generalized shunt circuit in figure 4.5. The currents on the primary side have to consist of the currents out of the secondary side and the currents flowing through any of the connected admittances towards other lines. The current towards the reference node can be determined directly using the port voltage with $U_x \cdot Y_{x5}$. The currents between the lines depend on the voltage difference of the port voltages. These relations result in the bottom half of (4.13) where the diagonal components $Y_i x$ of the shown submatrix are the sum of all

admittances connected to the corresponding line. (see (4.12)) The voltage difference is considered by substracting the admittance component, connecting two lines, in the respective matrix fields.

$$Y_{ix} = \sum_{j} Y_{Y_{ij}} \tag{4.12}$$

$$\mathbf{A}_{\text{shunt}} = \left[\begin{array}{cccc|c} & & \mathbf{I}_4 & & \mathbf{O}_4 \\ \hline Y_{1x} & -Y_{12} & -Y_{13} & -Y_{14} & \\ -Y_{12} & Y_{2x} & -Y_{23} & -Y_{24} & \mathbf{I}_4 \\ -Y_{13} & -Y_{23} & Y_{3x} & -Y_{34} & \\ -Y_{14} & -Y_{24} & -Y_{34} & Y_{4x} & \end{array}\right] \tag{4.13}$$

More complex power components can now be realized by a series connection of several series and shunt circuits. The chain matrix of the resulting component can simply be determined by multiplication of the matrices of the basic circuits. Components, which are not needed can generally be set to zero. To calculate the impedance and admittance matrices the inverse matrices of the submatrices $\mathbf{A}_{21}$ and $\mathbf{A}_{12}$ have to exist. Therefore it can be necessary to add components that are in another order of magnitude than those of the power component to model, but well within the numerical limitations of the processor used for calculation.

4.2 Active Components

Measuring active components is more challenging as they are components which can only be accurately measured while a 50 Hz component of 230 V or 400 V is tolerated by the measurement setup. Typical measurement equipment which tolerates high amplitudes does not have sufficient resolution to allow for low amplitude measurement. A 10 bit oscilloscope set to measure a phase to phase voltage amplitude of 565 V has a theoretical resolution of 1.1 V which will not be achieved in practice by a factor of at least 2. Other equipment such as network analyzers are not equipped to handle high amplitudes at their inputs.

Besides online impedance estimation techniques [RVS14] previous measurements of the grid impedance were realized using a power electronic converter to inject currents of varying frequency into the grid. Current and voltage are measured and the impedance is calculated. This method shows good results for low frequencies but is limited in bandwidth by the switching frequency of the semiconductors used. [Kno13] [JF15] [JGF+15].

[SLD12] introduces a measurement procedure designed for up to 500 kHz to validate grid models used for power line communication. In the following subsections 4.2.1 and 4.2.2 this measurement procedure is adapted for smaller frequencies and extended from DM injection to CM injection.

4.2.1 Coupling Circuits

In order to allow for a simple automated measurement over the desired frequency range a network analyzer is decoupled from the active components as shown in figures 4.6 and 4.7 for DM and CM signals

respectively. The signal generated by the network analyzer is fed to a power amplifier which increases the amplitude of the measurement signal. Since the power amplifier is not equipped to handle the voltages at the power line a high pass filter is used, which blocks the 50 Hz grid voltage but transmits the higher frequencies from the amplifier to the grid. This coupling circuit is equipped with the possibility to measure the voltage at the injection point as well as the injected current.

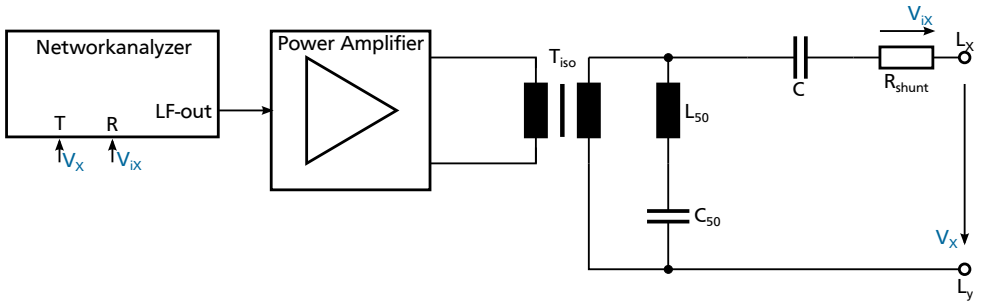

Figure 4.6.: DM measurement setup for active components

Galvanic isolation is achieved in both cases by an isolation transformer T_{iso} and one or three capacitors C. The current shunt resistors have to allow sufficient bandwidth and power dissipation.

In case of the DM coupling circuit in figure 4.6 the 50 Hz component has to be considered in more detail. The 50 Hz current flowing into the circuit is determined by the value of the blocking capacitor C and the grid voltage. In order to realize a low minimum measurement frequency a large value of capacitance is desired to allow for good transmission of those low frequencies into the measurement object. This in turn results in larger 50 Hz currents into the measurement setup which can not be tolerated by the power amplifiers output. In order to protect the power amplifier an additional path for the current is given by the resonant components L_{50} and C_{50}. The resonance has to have a very high quality factor in comparison to the sum of the parasitic impedance through the transformer and the output impedance of the power amplifier which are both very low.

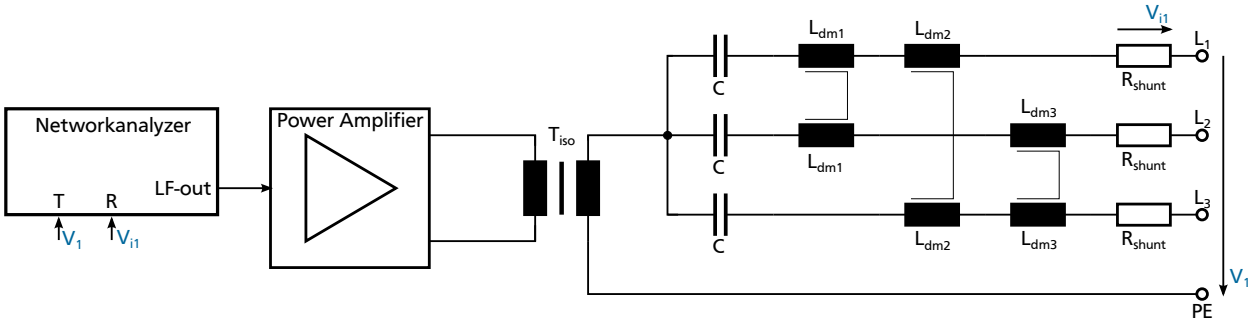

Figure 4.7.: CM measurement setup for active components

In case of the common mode coupler the 50 Hz component and all other differential mode components present in the grid are not transmitted towards the power amplifier since they are short circuited behind the coupling capacitors. The generated currents only have to be considered for the current rating of the components in the path. As common mode has to be injected into all phases with the same amplitude, any asymmetries of the setup have to be considered instead. Those are compensated in the coupling circuit by three coupled inductors ($L_{\text{dm}i}$), which block differential mode currents. This not only balances the injected CM current but also decreases DM currents from the grid.

4.2.2 Calibration of the active measurement setup

In typical measurement applications of a network analyzer such as the measurement of passive components as described in section 4.1 the network analyzer uses a calibration method in order to determine the nonidealities of the realized measurement setup or fixture. The typical calibration method for low frequency network analyzers (below 30 MHz) is the measurement of three known impedances, called standards, between the leads the measurement objects will be connected to. Those standards namely are:

- Open Circuit
- Short Circuit
- 50 Ω load

The maximum power the network analyzer can emit is limited to 10 dBm or 10 mW. Realizing the previously described measurement setup including the power amplifier above significantly increases the power emitted into the measurement object, which the typical 50 Ω standards provided with the network analyzer are not suited for. Therefore a self made standard is needed where the focus is not on it being exactly 50 Ω but rather it having a well known impedance. As it also has to be able to handle up to several 10s of watts the DM and CM standards are realized with 50 W wire wound resistors with an accuracy of 1 %. A wire wound resistor is expected to show noticeable inductive behavior in the given frequency range of up to 150 kHz resulting in the necessity to accurately measure the self designed calibration standards with a well calibrated network analyzer first. Since the common mode standard consists of three resistors they were selected during the measurement process to show as little deviation as possible.

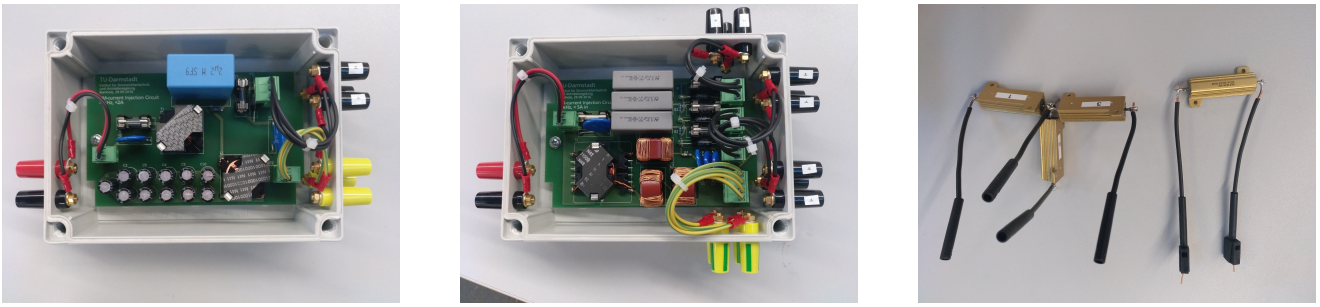

(a) DM coupler **(b)** CM Coupler **(c)** load standards

Figure 4.8.: Coupling circuits and corresponding calibration standards

The measured values can then be used to define a custom calibration standard. Figure 4.8 shows the two coupling circuits with their calibration standards which have the following values:

- DM: 10.2 Ω + 2 μH
- CM: 6.9 Ω + 910 nH

Due to the robust high power design of the standards their usability for high frequency measurements is limited. Within 150 kHz, however, the ohmic-inductive replacement circuit models the standards close to ideal resulting in good calibration results.

Figure 4.9 shows a measurement of the CM standards after calibration of the setup. The impedance range of the measurement is limited to the area between the short and open standard with decreasing accuracy towards the standards. Within the frequency range from 2 kHz to 150 kHz impedances between 1 Ω and 300 Ω can be measured well.

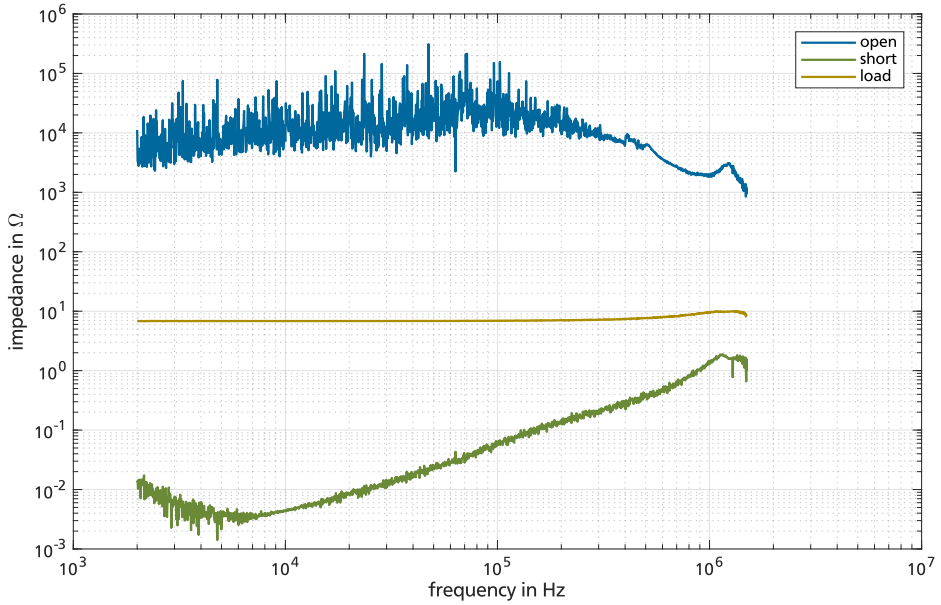

Figure 4.9.: Limits of the CM measurement

5 Component Models

Using the measurement techniques from chapter 4 models are derived, which can be used for the simulation according to section 3.3. Each section of this chapter presents a model for one of the used components, namely chokes, filters, cables, the utility grid and converters.

5.1 Chokes

Different types of inductors are used in the scope of this work. The noise sink converters choke is realized using a large pot core per phase. All three cores are chucked between two metal sheets which are connected to PE. As a result the cores of the chokes are connected to PE as well.

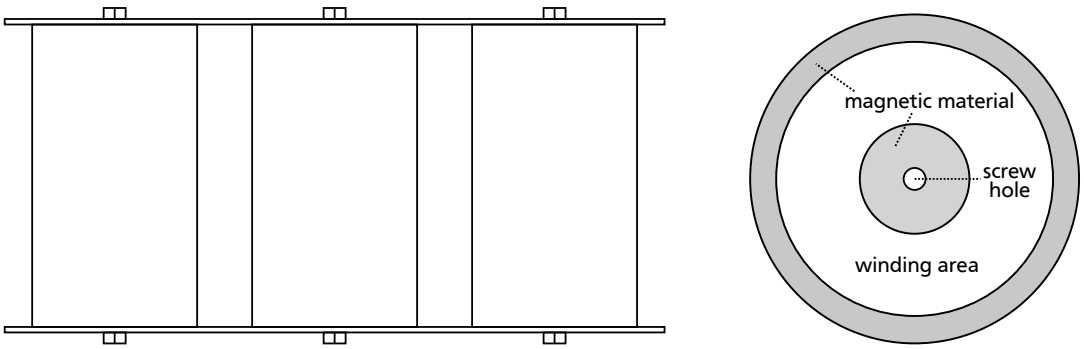

(a) side view **(b)** cross section

Figure 5.1.: Three phase pot choke

Figure 5.1 shows a sketch of the side view of the choke (a) and the cross section of one choke (b). From the cross section a capacitive coupling between the winding and the inner and outer magnetic material can be directly deducted. Any direct coupling between the windings can be neglected. The magnetic field is contained within the pot core, an electric field does not exist between two chokes, since their surfaces are on the same potential. The resulting replacement circuit is shown in figure 5.2.

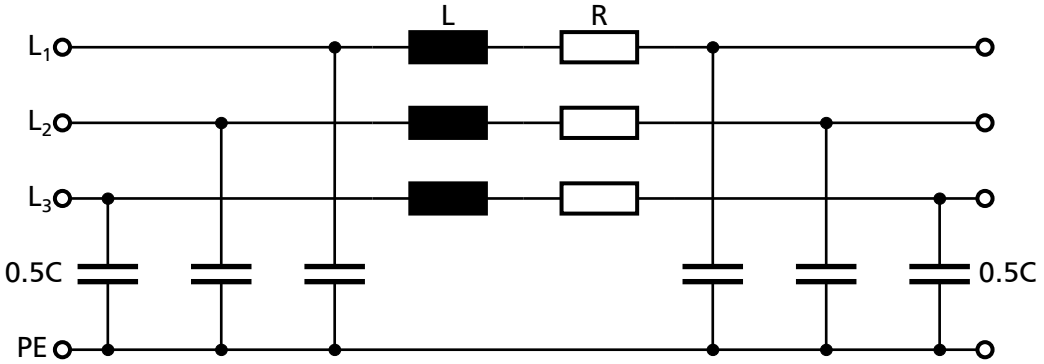

Figure 5.2.: Replacement circuit of a three phase choke

The noise source converter is self built in order to allow variation of many converter parameters including rated current and choke inductance. Therefore a total of 18 chokes were produced with the following ratings:

- nominal current: 20 A
- inductance: 1.47 mH

Above values result in a relative short circuit voltage of $u_K = 4\,\%$ which can be increased by serial connection. Higher currents can be realized by parallel connection of the chokes. Using all chokes the possible operating points range from 20 A with 24 % relative voltage drop if all are connected in series to 120 A at 4 % if all are connected in parallel.

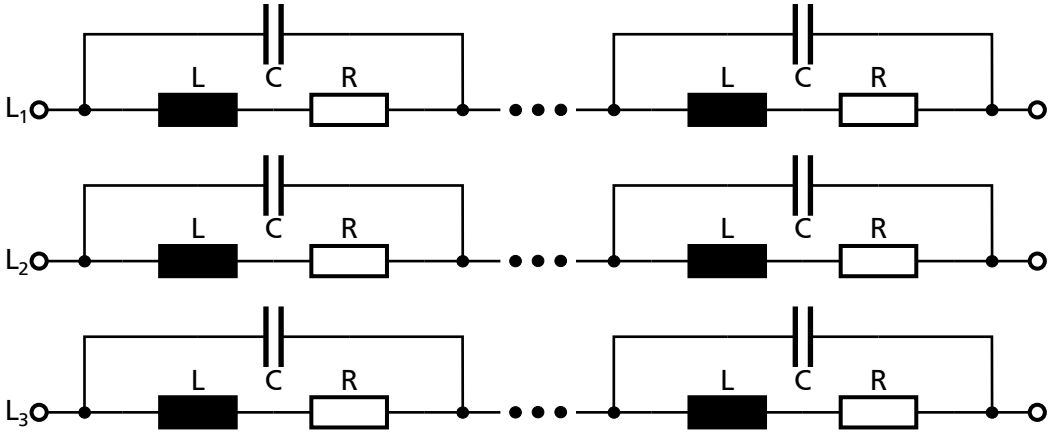

Figure 5.3.: Replacement circuit of variable choke

The chokes are protected by resin within three plastic containers each housing six chokes. In the frequency range up to 150 kHz there is no noticeable coupling between the chokes or towards PE. Therefore the chokes are modeled using a simple replacement circuit according to figure 5.3, where one combination of inductance, resistance and capacitance represents one choke. The self resonance of the chokes are well in the MHz-range resulting in a small value of the capacitance which is not noticeable in the considered frequency range. A further reduction of the replacement circuit as done for the serial components of the previous choke in figure 5.2 would be possible as well. The more complex model according to figure 5.3 was used nonetheless because the component is expected to have a large influence on the emitted noise and a more complex model allows to look beyond the considered frequency range and put the desired results into perspective.

5.2 Filters

EMI-filters consist of several stages of capacitors and common mode inductors. Typical filter orders range from 2^{nd} to 4^{th} order but are not generally limited to this range. Depending on the current rating of the filter the ratio between inductive and capacitive components changes. Figure 5.4 shows the CM inductor portfolio by Schaffner, as an example, in terms of their rated current. The inductance within a series is inversely proportional to the rated current with differences between the absolute inductances

in the different series due to varying core material and size. Other manufacturers of common mode inductors design their products similarly. Resulting from the decreasing inductance with increasing currents, filters with larger nominal currents have to contain more capacitance in order to provide the same damping with the same amount of stages. In order to model any type of filter for any current accurately a description of the capacitive and inductive components can be determined separately and combined to model the desired filter.

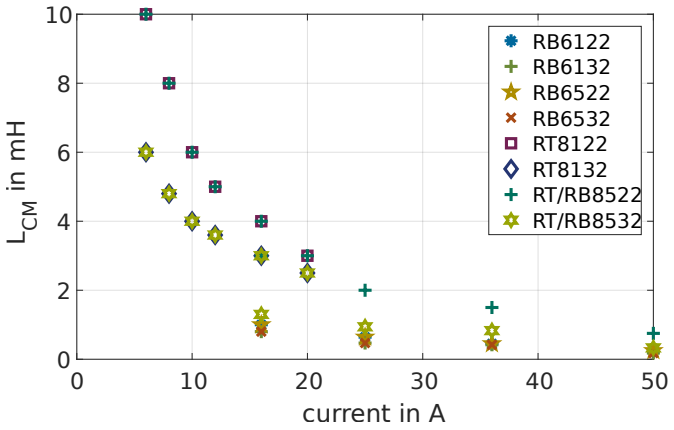

Figure 5.4.: Common mode inductance of Schaffner CM chokes

To describe a common mode choke more parameters than the common mode inductance are necessary. Figure 5.5 shows a possible replacement circuit to describe a CM-choke. The parameters are determined from datasheets if possible. Since the data quality is questionable in some cases, measurements were performed on several components in order to prove assumptions derived from datasheets. The parallel capacitance is not modeled in this work as the self resonances due to parasitic capacitances were found to be well beyond the maximum considered frequency of 150 kHz.

The differential mode inductance L_{DM} ranges from 0.3 % of the common mode value L_{CM} for small chokes up to 1 % for large chokes. Measurements confirm this and an average differential mode inductance of 2/3 % was chosen for the simulations in this work.

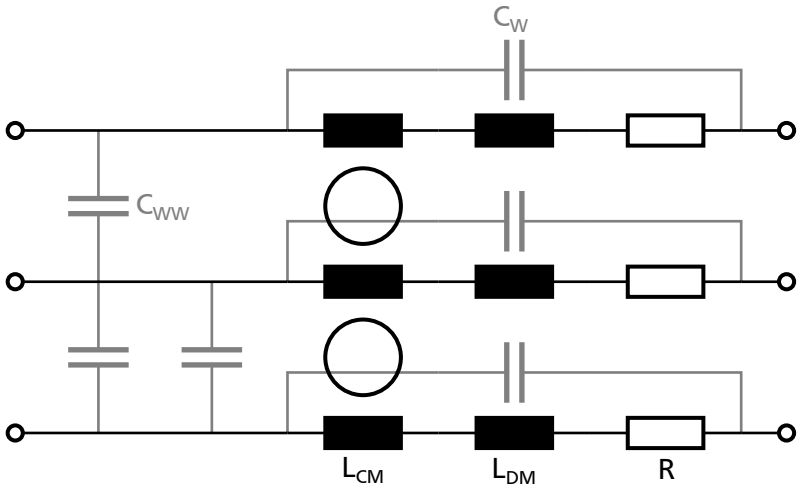

Figure 5.5.: Replacement circuit of a CM choke (grey components can be omitted within 150 kHz)

The DC resistances R of the chokes generate losses of 1 W up to 3 W per phase at the nominal current of all chokes. This value seems uncorrelated to the physical size of the device, therefore the average of the considered chokes, 2 W, was used for determination of the resistance.

At large frequencies two types of parasitic capacitances have to be considered: The self capacitance of each winding C_W as well as the capacitance between each set of windings C_{WW}, which is equal between all windings for symmetrical designs. The self resonances of the measured common mode chokes were found to be in the MHz range and the capacitances were omitted in the model without reducing its validity within the considered frequency range up to 150 kHz.

The other main components of EMI filters are film capacitors. Typically they have small parasitic inductances resulting in high frequencies for their first self resonance. Figure 5.6 shows the self resonance frequencies of different product lines of filter capacitors. The self resonance increases for larger values of the capacitance, however always stays well above 100 kHz. The influence of the stray inductance in the frequency range considered in this work is expected to be very small and is therefore neglected.

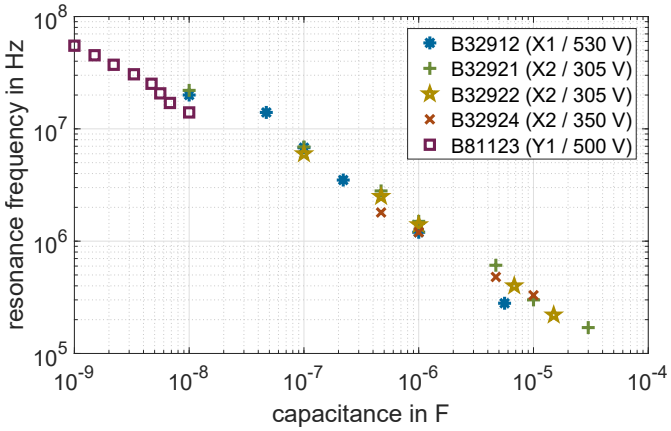

Figure 5.6.: Self resonant frequency over capacitance value

Typically the losses of EMI filter capacitors can be calculated by using the dissipation factor $\tan(\delta)$ denoted in the corresponding datasheet at a certain frequency. Typical maximum values for $\tan(\delta)$ are 1×10^{-3} at 1 kHz. This work assumes that the actual resistance of the capacitors stays well below this maximum in all cases and calculates a series resistance using a $\tan(\delta)$ of 1×10^{-4} at 1 kHz. Due to missing supplier data a frequency dependency is not modeled in this work.

Resistors in the MΩ-range in parallel to the capacitors ensure the discharge of the capacitors when all external voltages are disconnected. The measurement of 6 commercial filters showed discharge time constants between 0.5 s and 15 s. As this is at least 3 orders of magnitude from the lowest considered frequency of 2 kHz those resistances are neglected.

The resulting replacement circuit for EMI capacitors within the frequency range from 2 kHz to 150 kHz according to figure 5.7 only consists of the capacitance C and the equivalent series resistance ESR.

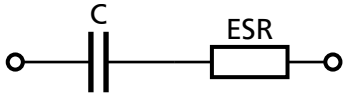

Figure 5.7.: Replacement circuit of EMI capacitors

The most typical filter structure, readily available by all filter providers, is a 3rd order filter with two capacitive stages and a common mode choke in between. Some of those filters are specifically designed for use with residual current detection by using a very small value for the Y-capacitance or no Y-capacitance in the capacitive stage on the grid side.

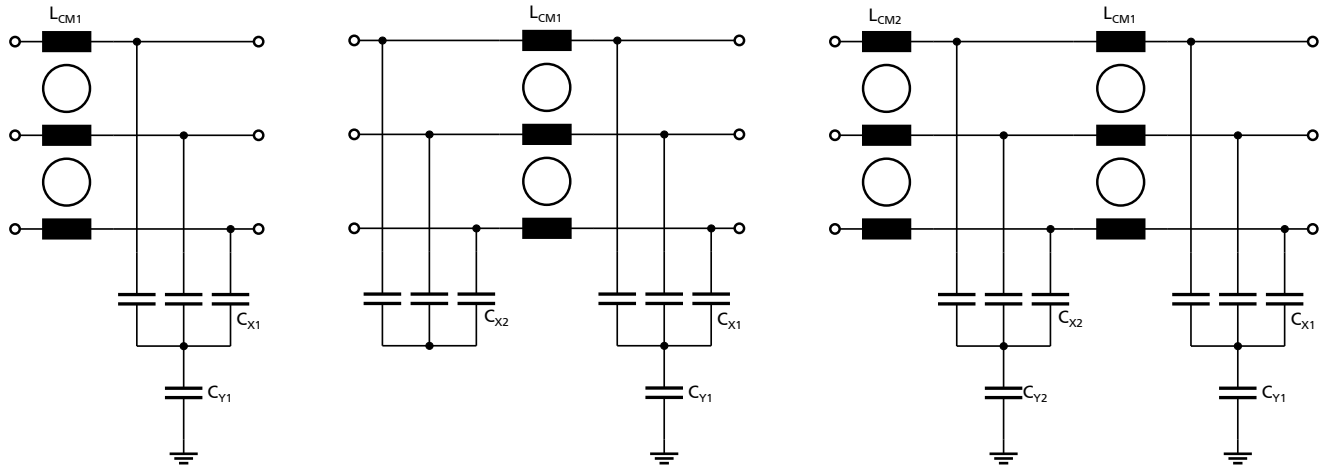

(a) 2nd order **(b)** 3rd order **(c)** 4th order

Figure 5.8.: Different filter topologies, grid left, converter right

Figure 5.8 shows the three variants of EMI filters used for simulation in this work. They are optimized towards small residual currents on the grid side (left in figures) by either omitting the Y-capacitance in the grid side capacitive stage completely or by connection to the grid through a common mode choke.

The individual components are modeled using the above findings from component surveys.

5.3 Cables

An influence of long cable connections between converters on their behavior is expected and has been observed by different publications both on the machine [LZL+16, Lus11, WHCJ10, ZWMZ16] and the grid [PO03, ZJL+14, WPC+16, ZJL+13] side of converters. Often cables are modeled with symmetrical models which is a valid assumption for cables with three conductors with and without shield. Cables with 4 and more conductors behave asymmetrically however resulting in the need for an asymmetrical model. In the first part of this section an analytical calculation approach for a cable with 5 conductors without shield is described and evaluated. The second part estimates the influence of a shield on the cable parameters. Since the analytical approach results in large errors, the third part introduces a measurement procedure based on chapter 4 and the resulting model used for simulation.

The following subsections are based on a cable cross-section as shown in figure 5.9. In case of unshielded cables the layout stays the same except for the brown conductor marked "S". The following dimensions will be used throughout the calculations:

- r_0: conductor radius
- r_{ij}: distance between centers of conductor i and j
- r_{i0}: distance between centers of conductor i and ground conductor

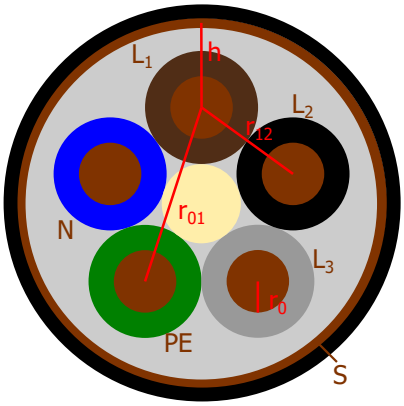

Figure 5.9.: Cross section of a shielded cable with five conductors

- h: distance between conductor centers and cable shield

5.3.1 Analytical approach for unshielded cables

This subsection determines a model analytically which fulfills the port properties from chapter 3 by default by presuming that the current through any line returns through the PE conductor, which is the reference node. All parameters are determined as per unit length parameters which is denoted by using lower case letters.

Inductive Components

There are three inductive components which have to be considered when modeling a cable:

- inner impedance, considering the skin-effekt
- outer impedance, being the coupling with the ground wire
- inductive coupling between the lines

The inner impedance can be described using Bessel functions [KMR13] of order 0 and 1 (J_0, J_1) as shown in (5.1).

$$z_{\text{in}}(\omega) = \frac{\sqrt{-j\omega\mu\sigma}}{2\pi r_0 \sigma} \cdot \frac{J_0(\sqrt{-j\omega\mu\sigma} \cdot r_0)}{J_1(\sqrt{-j\omega\mu\sigma} \cdot r_0)} \tag{5.1}$$

The resistance and inner inductance of the conductor can be calculated from the real and imaginary parts of (5.1).

$$r = \text{Re}\{z_{\text{in}}\} \tag{5.2}$$

$$\omega \cdot l_{\text{in}} = \text{Im}\{z_{\text{in}}\} \tag{5.3}$$

The outer impedance of a conductor with the ground conductor returning the current can be determined using the standard formula for two parallel conductors [KMR13]. (5.4) describes the outer inductance of line 1 depending on the length l of the conductor.

$$l_{11} = \frac{\mu_0}{\pi} \cdot \ln\left(\frac{r_{01}}{r_0}\right) \tag{5.4}$$

The inductive coupling between the different lines has two components [KMR13]. The first depends on the size and distance of the loops of each of the two conductors with the ground conductor. It is described using the $\ln\left(\frac{r_{02}}{r_0} \cdot \frac{r_{01}}{r_{12}}\right)$ term in (5.5). The second coupling term $\frac{\mu_r}{4}$ is supposed to model the inner impedance of the ground conductor and the voltage drop resulting on the other lines due to a current in one line, which flows back through the ground conductor by our definition of the mathematical model, where ground is the reference for the three lines and the neutral wire.

$$m_{12} = \frac{\mu_0}{2\pi} \cdot \left(\ln\left(\frac{r_{02}}{r_0} \cdot \frac{r_{01}}{r_{12}}\right) + \frac{\mu_r}{4}\right) \tag{5.5}$$

Using (5.5) the inner impedance of the ground wire does not depend on the frequency. Therefore the coupling in this work is modeled using only the geometric part of (5.5) and the inner impedance from (5.1) of the ground connector resulting in (5.6).

$$m_{12} = \frac{\mu_0}{2\pi} \cdot \ln\left(\frac{r_{02}}{r_0} \cdot \frac{r_{01}}{r_{12}}\right) + Z_{\text{in}}(\omega) \tag{5.6}$$

Figure 5.10 shows the analytically determined ohmic inductive series components of a 2.5 mm^2 unshielded cable with 5 conductors according to (5.1), (5.4) and (5.6). The inner impedance shows the expected properties. At around 10 kHz the Skin Effect starts to show its effect and the resistance of the wire increases while the inductance of the wire decreases. Other than the mutual inductances, the outer inductances l_{11} and l_{33} have a constant inductance throughout the whole frequency range and their impedances are therefore parallel lines increasing with constant 20 dB per decade. Their impedance is larger than the mutual impedances which are plotted considering the frequency dependency of the inner inductance of the mutual conductor (PE). Not only while the inner inductance is constant they show a slope of 20 dB per decade but also at high frequency, when the inner inductance becomes negligibly small. The shift between these parallel lines is hardly noticeable in figure 5.10 showing that an assumption according to (5.5) does not significantly influence the accuracy of calculated cable parameters.

A power cable can therefore be modeled using inductive cable parameters which are independent of frequency.

Measurements were carried out at a 5 wire cable with 6 mm^2 copper area per conductor. Table 5.1 compares the measured results to the calculated values for the inductive components per unit length of the given cable. The largest deviation appears in the case of m_{3N} with less than 7 %. The calculation of the inductive components therefore is possible using the formulas presented above.

The size of table 5.1 has been decreased using the symmetry of the cable. Considering figure 5.9 it can be seen that the self inductance of L1 and L2 has to be equal just like the self inductance of L3 and

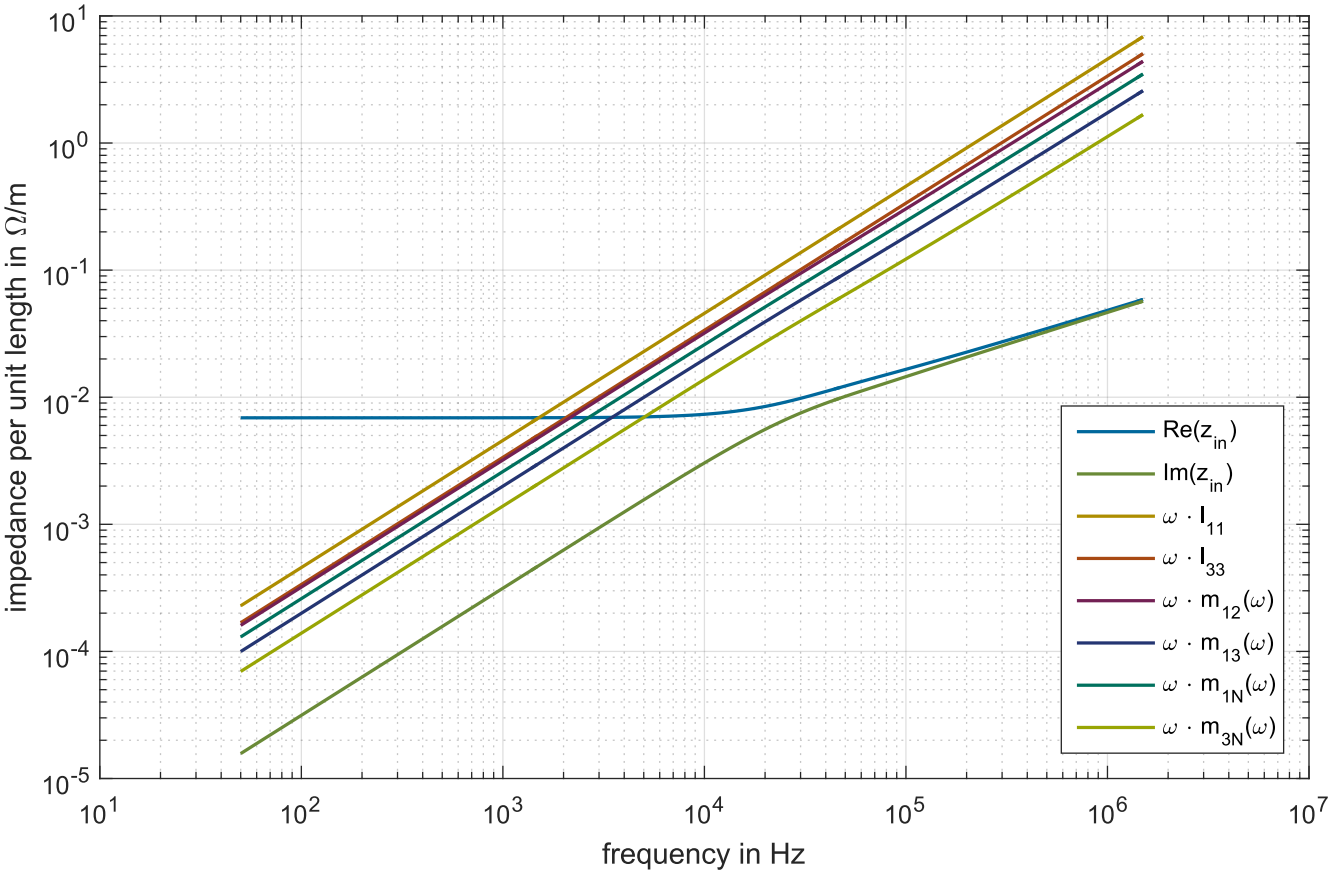

Figure 5.10.: Analytically calculated frequency dependent cable series impedances (5x2.5 mm^2)

N. Also some mutual inductances are the same, such as the mutual inductance between L1 and L3 and between L2 and N. The same has been done for figure 5.10.

Table 5.1.: Comparison of measured and calculated per unit length inductive components of a unshielded cable (5x6 mm^2); equal parameters listed in blue

value	description	measured	calculated	deviation
l_{11}, l_{22}	self inductance line 1	729 $\mathrm{nH\,m^{-1}}$	707 $\mathrm{nH\,m^{-1}}$	3.1 %
l_{33}, l_{NN}	self inductance line 3	533 $\mathrm{nH\,m^{-1}}$	514 $\mathrm{nH\,m^{-1}}$	3.7 %
m_{12}	mutual inductance line 1+2	437 $\mathrm{nH\,m^{-1}}$	445 $\mathrm{nH\,m^{-1}}$	−1.8 %
m_{13}, $m_{2\mathrm{N}}$	mutual inductance line 1+3	244 $\mathrm{nH\,m^{-1}}$	257 $\mathrm{nH\,m^{-1}}$	−5.1 %
$m_{1\mathrm{N}}$, m_{23}	mutual inductance line 1+N	355 $\mathrm{nH\,m^{-1}}$	353 $\mathrm{nH\,m^{-1}}$	0.6 %
$m_{3\mathrm{N}}$	mutual inductance line 3+N	150 $\mathrm{nH\,m^{-1}}$	161 $\mathrm{nH\,m^{-1}}$	−6.8 %

The capacitive coupling between two cable strings can be approximated by the capacitance between two parallel cylinders. Formula (5.7) is derived in most textbooks about theoretical electrical engineering and electromagnetic compatibility, such as [KMR13] and [Pau06].

$$c_{ij} = \frac{\pi \cdot \epsilon}{ln\left(\frac{r_{ij}}{2 \cdot r_0} + \sqrt{\left(\frac{r_{ij}}{2 \cdot r_0}\right)^2 - 1}\right)} = \frac{\pi \cdot \epsilon}{\operatorname{arcosh}\left(\frac{r_{ij}}{2 \cdot r_0}\right)} \tag{5.7}$$

A typical simplification of this formula can be made by assuming that the distance between the centers of the conductors is much larger than their radius ($r_{ij} >> r_{r_0}$), resulting in formula (5.8). However, the assumption is not valid for power cables, having large radii in comparison to their insulation.

$$c_{ij} = \frac{\pi \cdot \epsilon}{ln\left(\frac{r_{ij}}{r_0}\right)} \tag{5.8}$$

Table 5.2 shows the measured and calculated (according to (5.7)) capacitive parameters of an unshielded cable. Due to the symmetry of a cable with 5 conductors there are only two different parameters to be calculated being a capacitance between neighboring conductors such as L1 and L2 and the capacitance between opposing conductors, such as N and L2. (see figure 5.11)

Table 5.2.: Comparison of measured and calculated per unit length capacitive components of an unshielded cable (5x6 mm^2)

value	description	measured	calculated	deviation
c_{close}	capacitance between close conductors	58.4 pF m^{-1}	69.6 pF m^{-1}	−16.1 %
c_{far}	capacitance between far conductors	17.5 pF m^{-1}	48.1 pF m^{-1}	−63.6 %

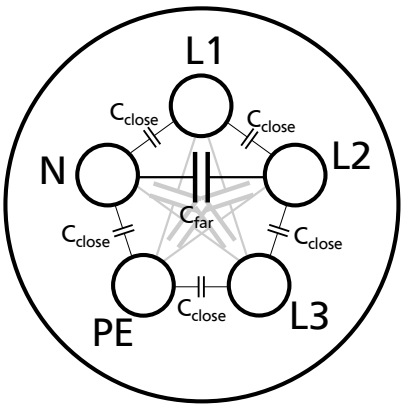

Figure 5.11.: Capacitances in a cable with 5 conductors

From table 5.2 it becomes obvious that the calculation of capacitive components of a cable is much less accurate than that of the inductive components. Concerning the accuracy of the analytical solution for two parallel cylindrical conductors, Clayton R. Paul states in [Pau06]:

> *"Although we may derive an exact expression (9.39a) for the per-unit-length capacitance of two bare wires, we cannot derive an exact expression for (1) more than two wires, or (2) wires with dielectric insulations [7]. For these cases we must use numerical methods to obtain the per-unit-length parameters."*

Power cables, however, always consist of more than two conductors and their dielectric is inhomogeneous, due to different materials within the cable and no (or an unknown) dielectric on the outside. For this case a measurement of the capacitive components rather than their calculation seems to be the more reliable and feasible solution.

5.3.2 Differences in self inductance and capacitance for shielded cables

The cable shield has to be considered as an additional conductor with two additional terminals resulting in a 10 port network instead of an 8 port network as for the unshielded cable. The components can be measured similarly as for the unshielded cable. Table 5.3 compares the calculated per unit length self inductance and capacitance of an unshielded cable to the measured parameters of a shielded cable.

The literature provides no solutions to calculate the inductances of shielded cables, other than for the case of an ideally centered coaxial cable. The complexity of a five conductor cable with shield is however by far greater, therefore the calculated parameters for an unshielded cable are compared to the measured values of the shielded cable, to show the influence of the shielding on the inductive behavior of the cable.

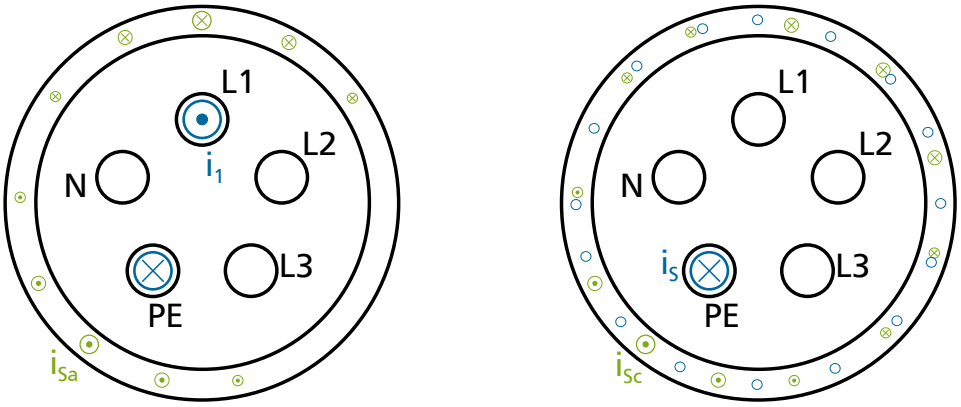

(a) current through L1 **(b)** current through shield

Figure 5.12.: Independent shield currents (green) resulting from currents (blue) through different conductors

A decrease in self inductance of the lines (l_{11} and l_{33}) can be observed for a cable with shield compared to a cable without shield. This can be easily explained if the shield is assumed to be an ideal conductor for simplicity. The ideal shield conducts a current which completely compensates the magnetic field, created by the conductors inside the shield (see figure 5.12), at its inner edge. Therefore there is no remaining field outside the shield. Keeping in mind the relation between inductance and energy W stored in a magnetic field (5.9) and the calculation of this energy by integration (5.10) [KMR13] it becomes clear that the compensation of the field results in a smaller volume to be integrated and therefore a smaller

value of inductance. Although the shield in an actual cable is not a perfect conductor and has holes the effect can be observed in the measurements very well. The decrease of the self-inductances is 27 % for l_{11} und l_{22} and 18 % for l_{33} and l_{NN}.

$$L = 2 \cdot \frac{W}{i^2} \tag{5.9}$$

$$W = \frac{1}{2} \cdot \int\int\int B \cdot H dV = \frac{1}{2} \cdot \mu \cdot \int\int\int \|H\|^2 \, dV \tag{5.10}$$

Table 5.3.: Comparison of measured parameters of a shielded cable to calculated cable parameters of an unshielded cable (5x2.5 mm^2); parameters in addition to the model from 5.3.1 and 5.3.1 colored blue

value	description	measured	calculated	deviation
l_{11}	self inductance line 1	530 $\mathrm{nH\,m^{-1}}$	728 $\mathrm{nH\,m^{-1}}$	−27.2 %
l_{33}	self inductance line 3	437 $\mathrm{nH\,m^{-1}}$	535 $\mathrm{nH\,m^{-1}}$	−18.3 %
l_{SS}	self inductance shield	312 $\mathrm{nH\,m^{-1}}$	na	na
c_{12}	capacitance between line 1+2	36.8 $\mathrm{pF\,m^{-1}}$	66.2 $\mathrm{pF\,m^{-1}}$	−44.4 %
c_{13}	capacitance between line 1+3	3.7 $\mathrm{pF\,m^{-1}}$	46.6 $\mathrm{pF\,m^{-1}}$	−92.1 %
c_{1S}	capacitance between line 1+shield	87.5 $\mathrm{pF\,m^{-1}}$	60.2 $\mathrm{pF\,m^{-1}}$	45.3 %

Concerning the capacitances, there are additional capacitances between each of the conductors and the shield. Due to the symmetry of the cable this capacitance is equal for all conductors, meaning there are now 3 values for capacitance, as shown in table 5.3. A derivation of the capacitance from conductor to cylindrical shield is made for 2 to 4 wires in [Web07]. Extending the concept to a 5 wire cable leads to equation (5.11), where:

- r_i: radius of the circle through the conductor centers
- r_a: inner radius of the shield cylinder
- r_0: radius of the conductors

$$c_{iS} = \frac{2 \cdot \pi \cdot \epsilon}{ln\left(\frac{r_\mathrm{a}^5}{5 \cdot r_\mathrm{i}^4 \cdot r_0} \cdot \left(1 - \frac{r_\mathrm{i}^{10}}{r_\mathrm{a}^{10}}\right)\right)} \tag{5.11}$$

The resulting c_{iS} is colored blue in table 5.3 and is 31.2 % smaller than the measured value. The inaccuracy in the capacitive components which is already observed for the unshielded cable is a problem in the shielded cable as well. This issue is also observed in [Web06], where the analytical approach, a simulation using finite element method and a measurement show three different results. A scaling factor for the permittivity is then assumed for the three different capacitance values of the cable. However this factor might depend on the size of the cable as well as other parameters, suggesting the identification of capacitive parameters of a power cable via measurement as the preferred option for cables with and without shield.

5.3.3 Measurement based model for shielded and unshielded cables

In the previous sections the cable was modelled in a way that the PE conductors impedances were transformed to the other conductors since this is more convenient for the simulation as described in chapter 3. If PE is considered the same as the other conductors however, additional symmetry can be used to determine the cable parameters.

Capacitive Components

Each conductor in the cable is coupled capacitively to each other conductor of the cable. Considering the symmetry of the cable one can assume that there are only three different capacitive components possible between any set of the two conductors:

- c_{12}: capacitance between neighboring round conductors
- c_{13}: capacitance between distanced round conductors
- c_{1S}: capacitance between round conductor and shield

In contrast to the calculated values of capacitance in subsection 5.3.2 the capacitance c_{13} does not consider the electric field between two conductors without any other conductor present, but rather the actual self capacitance between two conductors which are being shielded by a shield as well as neighboring conductors. c_{13} is therefore not the capacitance you measure between two distanced lines but rather the value you need to represent the capacitive behavior of the cable in a replacement circuit as in subsection 5.3.2. The same holds true for the values of c_{12} and c_{1S}. Figure 5.13 is the extension of figure 5.11 received by adding a shield and the capacitances to the shield. c_{12} corresponds to the previous c_{close} and c_{13} corresponds to c_{far}.

Each of the regular round conductors is connected to the other conductors via two c_{12} and c_{13} each and one c_{1S}. The shield is connected to the surroundings through five equal capacitances c_{1S}. To determine the three parameters three measurements are sufficient. By connecting conductors externally the capacitance between those conductors can be considered shorted within the frequency range where the cable does not show wave impedance characteristics yet. Therefore the amount of capacitances influencing a measurement can be greatly reduced. Four possible cases along with the capacitance measured when connecting the conductors such that only two terminals remain to measure the capacitance between those terminals are:

- connect all inner conductors: $c_{\text{A}} = 5 \cdot c_{1S}$
- connect 4 inner conductors and shield: $c_{\text{B}} = 2 \cdot c_{12} + 2 \cdot c_{13} + c_{1S}$
- connect 2 neighboring conductors, connect all others: $c_{\text{C}} = 2 \cdot c_{12} + 4 \cdot c_{13} + 2 \cdot c_{1S}$
- connect 2 distanced conductors, connect all others: $c_{\text{D}} = 4 \cdot c_{12} + 2 \cdot c_{13} + 2 \cdot c_{1S}$

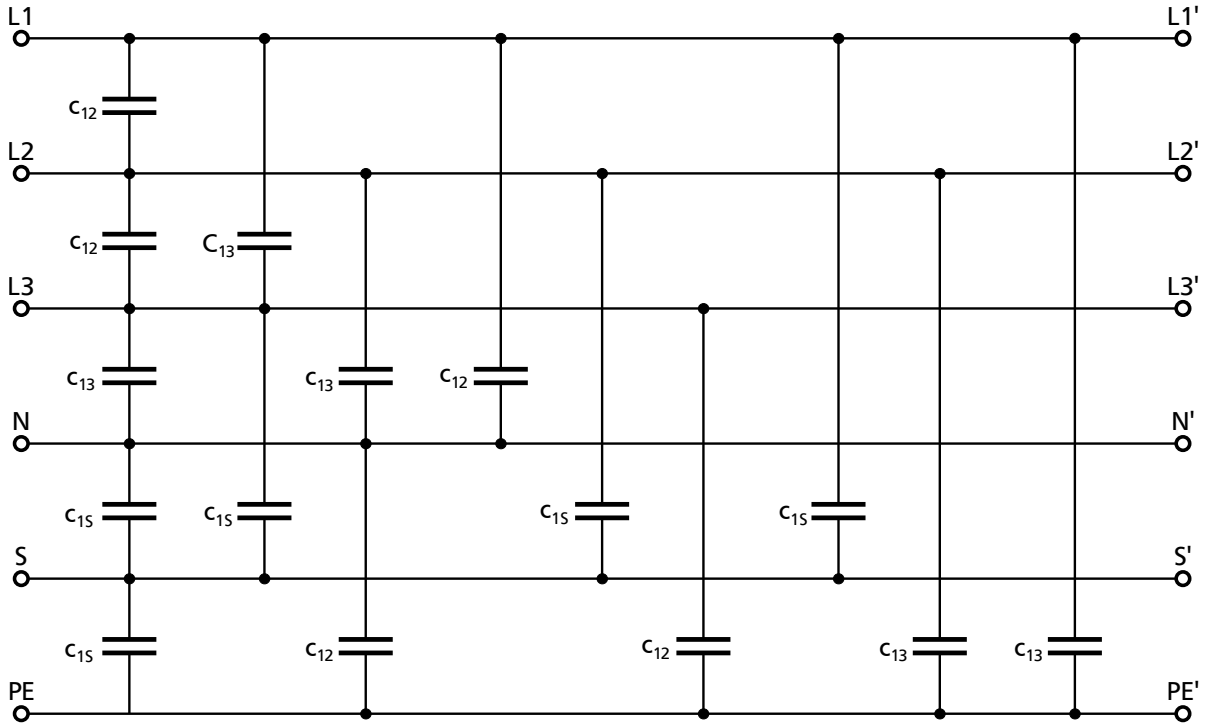

Figure 5.13.: Capacitive components of the cable model

Using the first three formulas one can easily write:

$$c_{1S} = \frac{c_A}{5} \tag{5.12}$$

$$c_{12} = c_B - \frac{c_C}{2} \tag{5.13}$$

$$c_{13} = \frac{c_C - c_B - 0.2 \cdot c_A}{2} \tag{5.14}$$

Theoretically the calculation above delivers the correct cable parameters, however, due to measurement accuracy especially c_{13} which is by an order of magnitude smaller than the other components is quite inaccurate. It has proven to give better results to use the average of the calculation above utilizing both c_C and c_D.

Using the theory from chapters 3 and 4 a chain matrix for the capacitive part (5.15) of the cable can be written in terms of the parameters above, using the 5^{th} order identity matrix $\mathbf{I}_5$ and 5^{th} order zero matrix $\mathbf{O}_5$.

For simplicity, the admittance of the above capacitances with the same indices are used in (5.15). Resistive components between the conductors could be considered by including them in the admittances in (5.15).

$$\begin{pmatrix} v_1 \\ v_2 \\ v_3 \\ v_N \\ v_S \\ i_1 \\ i_2 \\ i_3 \\ i_N \\ i_S \end{pmatrix} = \left[\begin{array}{ccccc|c} \multicolumn{5}{c|}{\mathbf{I}_5} & \mathbf{O}_5 \\ \hline y_B & -y_{12} & -y_{13} & -y_{12} & -y_{1S} & \\ -y_{12} & y_B & -y_{12} & -y_{13} & -y_{1S} & \\ -y_{13} & -y_{12} & y_B & -y_{13} & -y_{1S} & \mathbf{I}_5 \\ -y_{12} & -y_{13} & -y_{13} & y_B & -y_{1S} & \\ -y_{1S} & -y_{1S} & -y_{1S} & y_{1S} & -y_A & \end{array}\right] \cdot \begin{pmatrix} v'_1 \\ v'_2 \\ v'_3 \\ v'_N \\ v'_S \\ i'_1 \\ i'_2 \\ i'_3 \\ i'_N \\ i'_S \end{pmatrix} \tag{5.15}$$

Inductive Components

When assuming an equivalent circuit as in figure 5.14 each conductor has a self inductance l_{ii} and mutual inductances to all other conductors m_{ij}. Due to symmetry the self inductances must be equal except for the self inductance of the shield. Also the mutual inductances only appear in three different forms and the inductive components can be simplified to only five values:

- l_{11}: self inductance of each conductor (l_{11}, l_{22}, l_{33}, l_{NN}, l_{PP})
- l_{SS}: self inductance of the shield (l_{SS})
- m_{12}: mutual inductance between neighboring conductors (m_{12}, m_{1N}, m_{23}, m_{3P}, m_{NP})
- m_{13}: mutual inductance between distanced conductors (m_{13}, m_{1P}, m_{2N}, m_{2P}, m_{3N})
- m_{1S}: mutual inductance between each conductor and shield (m_{1S}, m_{2S}, m_{3S}, m_{NS}, m_{PS})

To determine those five values at least five measurements have to be performed and inductances determined from that:

- L_A: inductance of a loop of two neighboring conductors
- L_B: inductance of a loop of two distanced conductors
- L_C: inductance along one conductor
- L_D: inductance along the shield
- L_E: inductance of a loop of a conductor and the shield

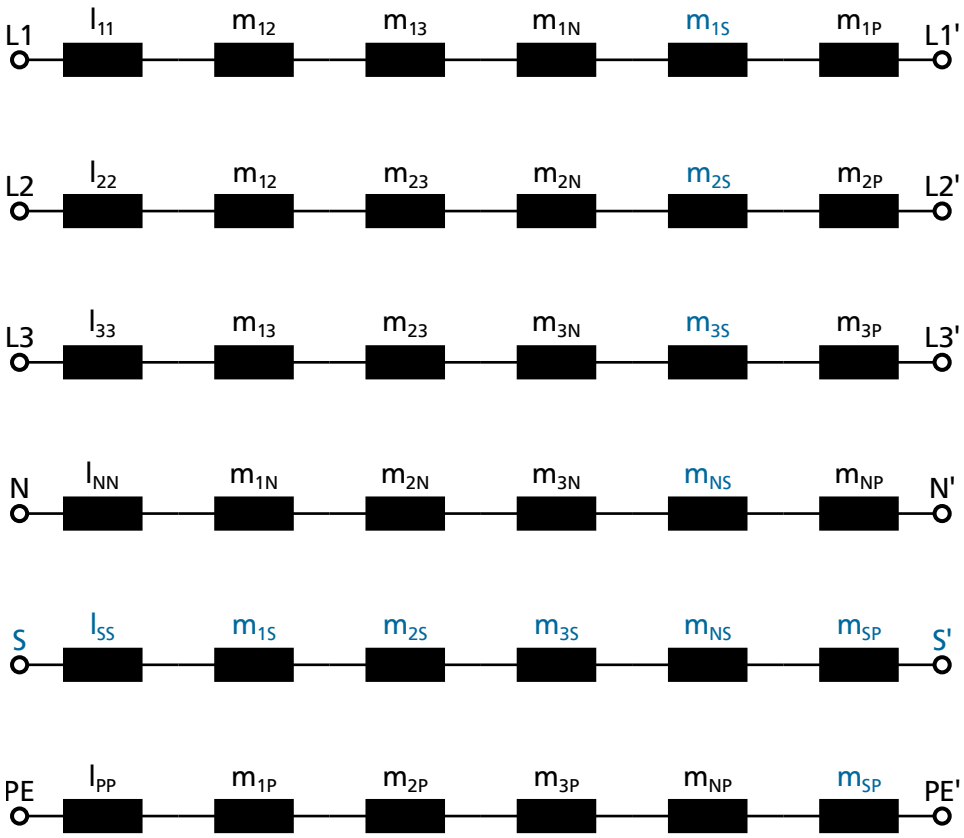

Figure 5.14.: Inductances per unit length for a shielded cable (for unshielded cables all blue inductances are zero)

In case of L_A, L_B, L_E the two above mentioned conductors are connected on the secondary side of the cable. All other connectors are left open both on the primary and secondary side. In case of L_C and L_D all connectors of the cable are isolated from each other. Figure 5.15 shows two different measurement setups to determine the above parameter L_B because both sets of conductors are distanced far.

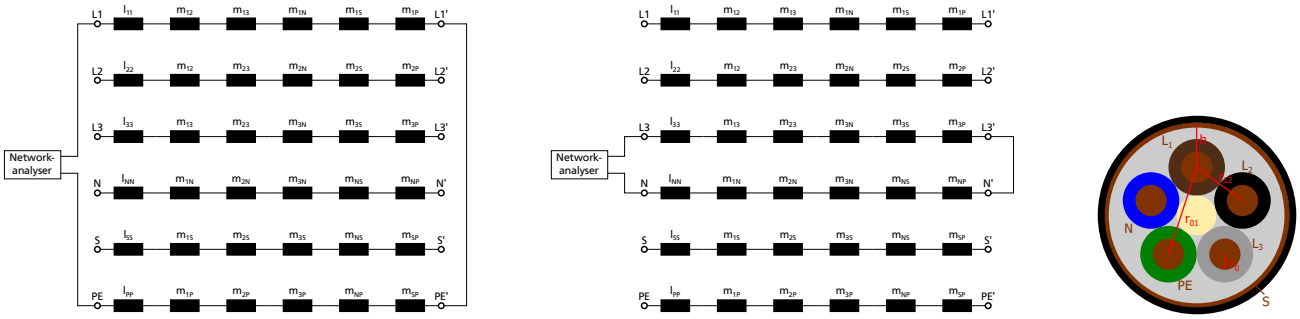

(a) L_1 to PE **(b)** L_3 to N **(c)** cable layout

Figure 5.15.: Different cable measurements and conductor layout of the cable

The measured inductances can be divided by the length of the cable and written in terms of the above listed inductive components per unit length of the cable:

$$l_A = 2 \cdot l_{11} + 4 \cdot m_{12} + 2 \cdot m_{13} + 2 \cdot m_{1S} \tag{5.16}$$

$$l_B = 2 \cdot l_{11} + 2 \cdot m_{12} + 4 \cdot m_{13} + 2 \cdot m_{1S} \tag{5.17}$$

$$l_C = l_{11} + 2 \cdot m_{12} + 2 \cdot m_{13} + m_{1S} \tag{5.18}$$

$$l_D = 5 \cdot m_{1S} + l_{SS} \tag{5.19}$$

$$l_E = l_{11} + 2 \cdot m_{12} + 2 \cdot m_{13} + 4 \cdot m_{1S} + l_{SS} \tag{5.20}$$

From this the chain matrix components can be derived. The diagonal components of the relevant submatrix must be equal to l_A for conductors next to the reference port (PE), l_B for conductors distanced from the reference port and l_E for the shield. The measurement of l_B at L1 and PE in figure 5.15 excites

only one secondary side port which is equal to the primary side port, at which the measurement is taken. The resulting impedance therefore is a diagonal component.

$$\begin{pmatrix} v_1 \\ v_2 \\ v_3 \\ v_N \\ v_S \\ i_1 \\ i_2 \\ i_3 \\ i_N \\ i_S \end{pmatrix} = \left[\begin{array}{c|ccccc} & z_B & z_C - 2\cdot z_{12} + z_{13} & z_C - z_{13} & z_C - z_{12} & z_C - z_{12} \\ & z_C - 2\cdot z_{12} + z_{13} & z_B & z_C - z_{12} & z_C - z_{13} & z_C - z_{12} \\ \mathbf{I}_5 & z_C - z_{13} & z_C - z_{12} & z_A & z_C + z_{12} - 2\cdot z_{13} & z_C - z_{13} \\ & z_C - z_{12} & z_C - z_{13} & z_C + z_{12} - 2\cdot z_{13} & z_A & z_C - z_{13} \\ & z_C - z_{12} & z_C - z_{12} & z_C - z_{13} & z_C - z_{13} & z_E \\ \hline \mathbf{O}_5 & \multicolumn{5}{c}{\mathbf{I}_5} \end{array}\right] \cdot \begin{pmatrix} v_1' \\ v_2' \\ v_3' \\ v_N' \\ v_S' \\ i_1' \\ i_2' \\ i_3' \\ i_N' \\ i_S' \end{pmatrix} \tag{5.21}$$

The measurement setup using L3 and N can be used to determine the non-diagonal matrix components. Now two secondary side ports are excited with the same current with opposing sign and the difference between two primary side voltages can be written in terms of the current i_{meas} and the components of the chain matrix a_{ij}:

$$v_{meas} = v_3 - v_4 = a_{38}\cdot i_{meas} - a_{39}\cdot i_{meas} - a_{48}\cdot i_{meas} + a_{49}\cdot i_{meas} \tag{5.22}$$

Rearranging for the measured impedance $z_B = \frac{v_{meas}}{i_{meas}}$ and inserting the known diagonal components of the submatrix leads to:

$$z_B = z_A - a_{39} - a_{48} + z_A \tag{5.23}$$

From subsection 4.1.2 it is known that the submatrix of a chain matrix describing passive series impedances including mutual inductances is diagonally symmetrical. a_{39} and a_{48} therefore must be equal and can be calculated by:

$$a_{39} = a_{48} = z_A - \frac{z_B}{2} = z_C + z_{12} - 2\cdot z_{13} \tag{5.24}$$

All other non-diagonal components can be described accordingly. In case the layout of a cable is not symmetrical, setting up the chain matrix with all individual components according to figure 5.14 is possible as well, but results in a quite complex matrix and the necessity to take 36 different measurements rather than 5.

When measuring the capacitances and inductances of different cables an interesting effect can be observed. The slope of the impedances is slightly smaller than 20 dB per decade while the phase is smaller than 90° by the same factor. Due to the cable resistance in series with the inductance and the isolation conductance in parallel to the capacitance this effect is expected. Due to the constant factor in

phase and slope the quality factors Q_L and Q_C are introduced to describe the ohmic components along with the reactive components:

$$z_\mathrm{L} = \mathrm{e}^{j\cdot\frac{\pi}{2}\cdot Q_\mathrm{L}} \cdot \omega^{Q_\mathrm{L}} \cdot l \tag{5.25}$$

$$y_\mathrm{C} = \mathrm{e}^{j\cdot\frac{\pi}{2}\cdot Q_\mathrm{C}} \cdot \omega^{Q_\mathrm{C}} \cdot c \tag{5.26}$$

By setting the quality factors to 1 (5.25) and (5.26) simplify to the well known equations: $z_\mathrm{L} = \mathrm{j}\cdot\omega\cdot l$ and $y_\mathrm{C} = \mathrm{j}\cdot\omega\cdot c$. For values between 0 and 1 the cable parameters per unit length can be determined in dependence of the angular frequency directly from formulas (5.25) and (5.26) as shown below by determining the real and imaginary parts respectively.

$$l(\omega) = \frac{\mathrm{Im}(z_\mathrm{L})}{\omega} \tag{5.27}$$

$$r(\omega) = \mathrm{Re}(z_\mathrm{L}) \tag{5.28}$$

$$c(\omega) = \frac{\mathrm{Im}(y_\mathrm{C})}{\omega} \tag{5.29}$$

$$g(\omega) = \mathrm{Re}(y_\mathrm{C}) \tag{5.30}$$

The above resistance increases with frequency which is physically plausible when considering the skin effect. At low frequencies the resistance of the cable would trend towards 0 however. Therefore in addition to the frequency dependent parameters, the DC resistance of the cable has to be added to the model.

A comparison between measurements taken at a non shielded cable and the model including the capacitances determined by measurement is shown in figure 5.16. A comparison for a shielded cable is shown in figure 5.17. In both cases the results match well in terms of the low frequency impedance, the resonance frequencies and the wave impedance. However, additional resonances distort the measured waveforms which can not be modeled using symmetrically placed conductors within the cable.

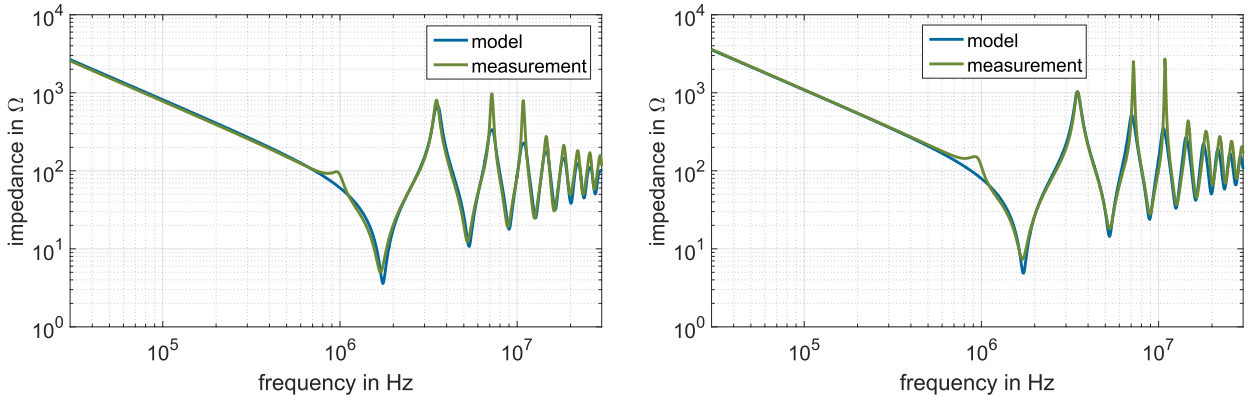

(a) close conductors **(b)** far conductors

Figure 5.16.: Verification of unshielded cable model, length = 21.6 m

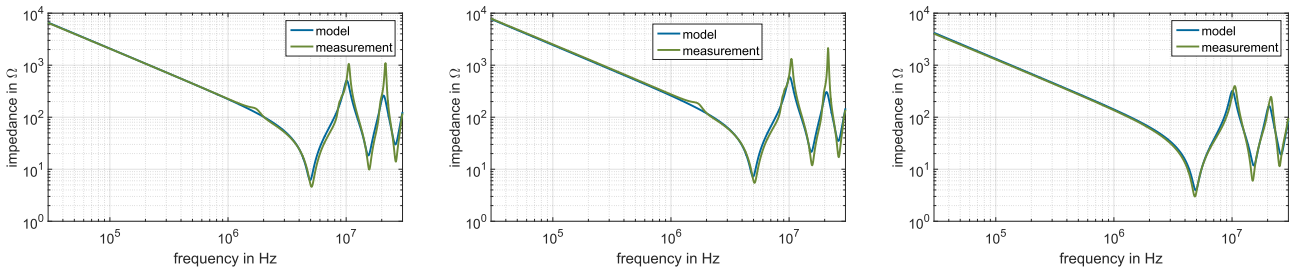

(a) close conductors **(b)** far conductors **(c)** conductor to shield

Figure 5.17.: Verification of shielded cable model, length = 8 m

Comparing this measurement based asymmetrical cable model to cable models used in papers shows a strong advantage of this technique. When only the asymmetry of the capacitances, but equal inductive components are assumed [Hel08], a large mismatch even for the first resulting cable resonances can be seen. The amount of resonances displayed in publications is typically small to keep deviations between measurements and symmetrical models acceptable. Even not displaying any resonance is possible [LZL+16].

Order Reduction of the shielded cable model

As discussed in the previous subsections and shown in figures 5.13 and 5.14 a shielded cable can be modeled as a 10-port network without any constraints. However, for the realized three phase simulation an 8-port network is required, which means that the shielded cable has to be reduced in order by determining two dependent and independent variables. This can be achieved only in case that the cable shield is connected to PE on both sides of the cable connection because the voltages at both ends of the cable shield are unknown otherwise and therefore the currents can not be calculated.

[SK11] states that especially for long cable connections a shield should be grounded on both sides in order to offer effective shielding. Therefore for electrically long cables the order of the cable can be reduced from a 10-port network to an 8-port network. Electrically short cables could be measured as a regular 8-port with the shield grounded at one end. Electrically long cables with a shield connection on only one side can not be calculated as 8-ports. To do so, the simulation would have to be extended to a 10-port simulation where the shield conductor of cable connections with disconnected shield has to be terminated by a large impedance on the corresponding side and shorted to PE where it is connected.

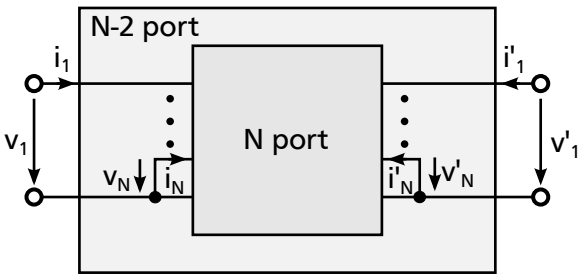

Figure 5.18.: Order reduction of an N port network by shorting ports

As seen in figure 5.18, the order of a cable with shorted shield is reduced by 2 orders without any influence on the other ports. The influence of the cable shield is still simulated, since the chain matrix of

the cable is calculated as the k^{th} power of the full set of parameters (including the shield), resulting in a repetitive multiplication of the shield parameters with all other parameters.

5.4 Power Grid

The LV grid is formed by a 400 V, 400 kV A transformer with a relative short circuit voltage of 3.9 %. The transformer supplies 4 test-benches from a conductor rail of approximately 40 m through a switching gear which is connected directly to the transformer with less than 20 m of cable. The impedance of the power grid is determined using the coupling circuits introduced in section 4.2. It is measured both with and without use of a Line Impedance Stabilization Network (LISN). In all cases no loads are connected to the grid at any point ensuring that the actual passive impedance of the grid is measured.

The measurement of the grid (blue) and the derived model (green) are displayed in figure 5.19. For frequencies below 80 kHz the measured grid impedance is ohmic inductive, which matches the common way to model power grids. Above this frequency several resonances with additional parasitic capacitances in the distribution and transformer are visible. Modeling those resonances would result in a very complicated replacement circuits, which is strongly dependent on the transformer and distribution under consideration. To avoid this a ohmic-inductive replacement circuit is chosen.

Calculating the inductance and resistance to match the measured ohmic-inductive behavior results in a resistance of $R = 287\,\mathrm{m\Omega}$ and an inductance of $L = 84\,\mu\mathrm{H}$ which corresponds to a R/X_L ratio at 50 Hz of 11. This factor is untypically large and does not match the expectations regarding the distribution network. A $35\,\mathrm{mm}^2$ copper cable would have to be more than 500 m long to realize this resistance. Since the distances are much smaller and the used conductor cross sections are larger the resistance is considered a measurement error of the network analyzer. Small errors in the phase measurement can result in large deviations of the calculated resistance, since the phase is close to 90° above 3 kHz and measurement accuracy decreases below this frequency anyways due to the utilized bandpass filters and minimum passing frequency of the coupling circuits. The resistance of the grid was therefore chosen to result in a R/X_L ratio of 1 at 50 Hz, which is a low value for low voltage grids but realistic for the comparably small physical dimensions.

The resulting parameters of the grid model, whose impedance is shown in green in figure 5.19, are shown in table 5.4:

Table 5.4.: Measured and modeled grid impedance

	measured	model
R_grid	287 mΩ	26 mΩ
L_grid	84 μH	84 μH

To smooth the impedance at high frequencies and allow for an accurate and comparable model of the grid impedance over the full considered frequency range a LISN is added to the setup in front of the grid connection. Besides easily modeled impedances this also offers a repeatability of measurements throughout the frequency range the LISN is specified in, which is from 9 kHz up to 30 MHz. Within this frequency range the impedance from each phase to ground is specified to be 50 Ω in parallel to 5 Ω plus 50 μH. Internally this is realized by the layout shown in figure 5.20 for one phase including the

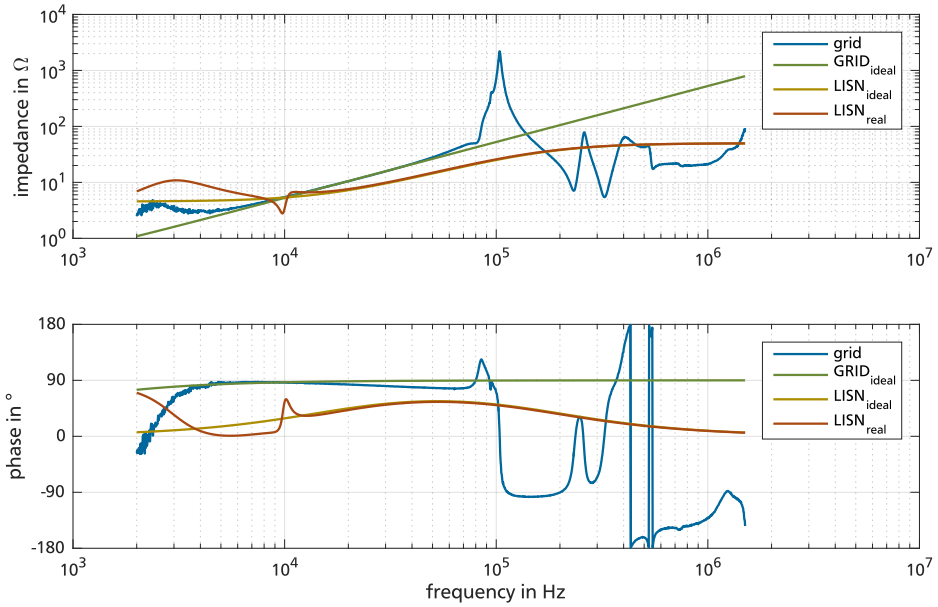

Figure 5.19.: Measured grid impedance

ohmic-inductive grid representation. The impedances of an ideal LISN (yellow) and the LISN according to figure 5.20 (red) are drawn in figure 5.19.

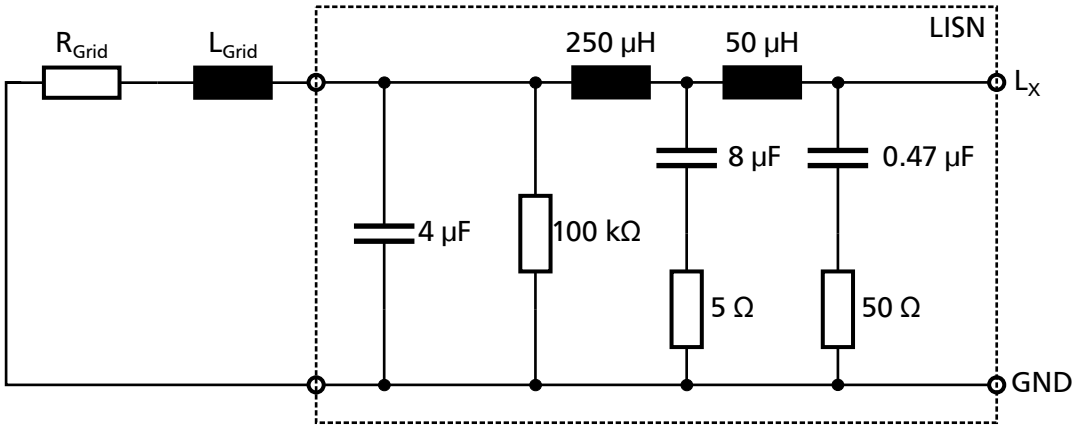

Figure 5.20.: Replacement circuit of one LISN phase with grid

A significant change in the grid impedance is observed due to the loads connected to the grid in several publications [JF15, JGF+15, Kno13]. In a separate publication the influence of a single converter with and without EMI-filter is discussed and the influence of just one EMI-filter is found to be significant, well below 150 kHz [BG18]. To avoid variations in the grid impedance all measurements in this work were performed with all other laboratory equipment and setups disconnected from the grid under examination.

5.5 Converters

The coupling circuits described in 4.2.1 are not suitable to determine the impedance into the power part of a converter directly, since the coupling is bidirectional. The harmonic components of the con-

verter at its switching frequency and the multiples of that would therefore couple directly into the high frequency source of the coupling circuit, destroying it or the coupling circuit in between.

Measurements were therefore performed in front of the converter choke and published separately [BG18]. Significant information about the impedance of the converters power part could not be extracted. The impedance of the choke alone is much larger than the grid impedance resulting in no significant change of impedance at the PCC by adding a converter connected solely through a choke. Extracting the impedance of the switching cell of the converter from this small deviation was not possible.

The same approach was therefore realized using time domain simulation: A three phase voltage source at the PCC with adjustable frequency is realized and the current into the converter with choke is measured. The impedance in case of CM is purely determined by passive components as the regular converter control only acts on differential mode components. The DM impedance within the control bandwidth can be varied by the converter, however. This consideration results in the converter models in figure 5.21 if simulated as a noise source or noise sink respectively.

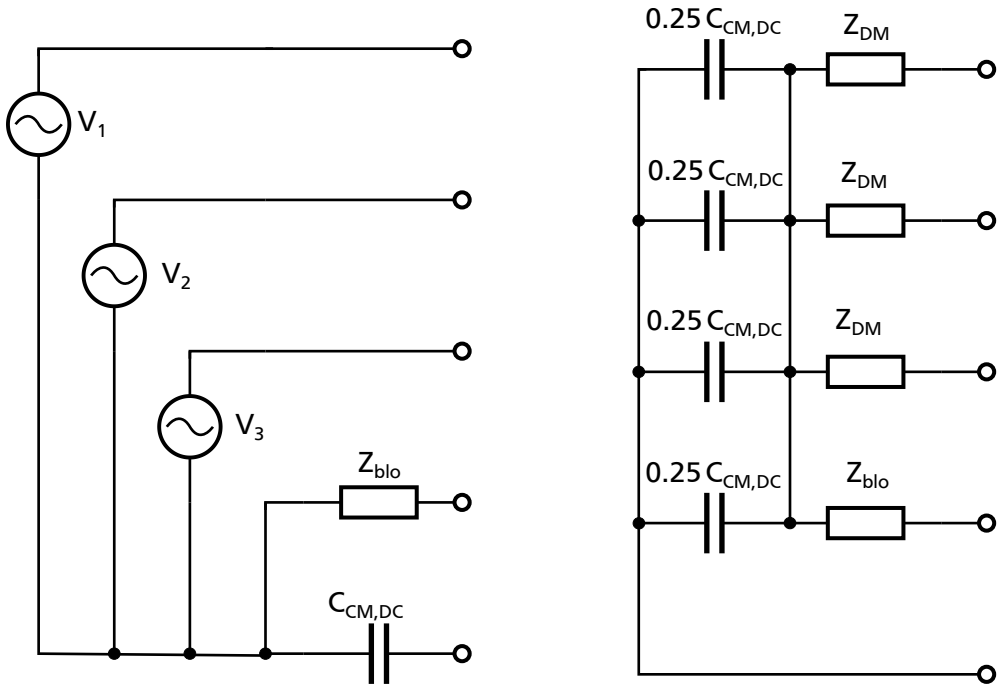

Figure 5.21.: Frequency domain model of a converter (without chokes)

The converter as a source is modeled by three voltage sources in the three lines and a blocking impedance in the neutral line, which is very large. This effectively disconnects this node, which is necessary for a typical three phase converter without active neutral connection. The impedance from the DC link to ground is assumed to be capacitive and represented by $C_{\mathrm{CM,DC}}$ in the PE path. By doing so this impedance is only visible to CM components while DM components are shorted at the starpoint.

In case of a converter considered to be a noise sink, the DM impedance is represented by Z_{DM} and the lines are shorted after this, making this impedance the only impedance visible to DM components. The CM impedance is represented by the capacitance $C_{\mathrm{CM,DC}}$, which is drawn distributed between the four top conductors but could just as well be placed in the PE path.

The value of $C_{\mathrm{CM,DC}}$ can be estimated from the area of the power module and the used DC link capacitors or can be chosen as a discrete component during the CM design process of the circuit. The DM impedance Z_{DM} depends on the control loop within the bandwidth of the controller.

In order to determine Z_{DM} a simulation imitating the measurement procedure with the coupling circuits was run. An additional DM component is fed to the PCC and current and voltage of the converter are measured and used to calculate the impedance at different frequencies. Figure 5.22 shows the results of the simulation as Z_{sim}. For frequencies above the switching frequency of 10 kHz the impedance shows typical inductive behavior and increases with frequency. The average value of the impedance is equal to the value of the simulated choke.

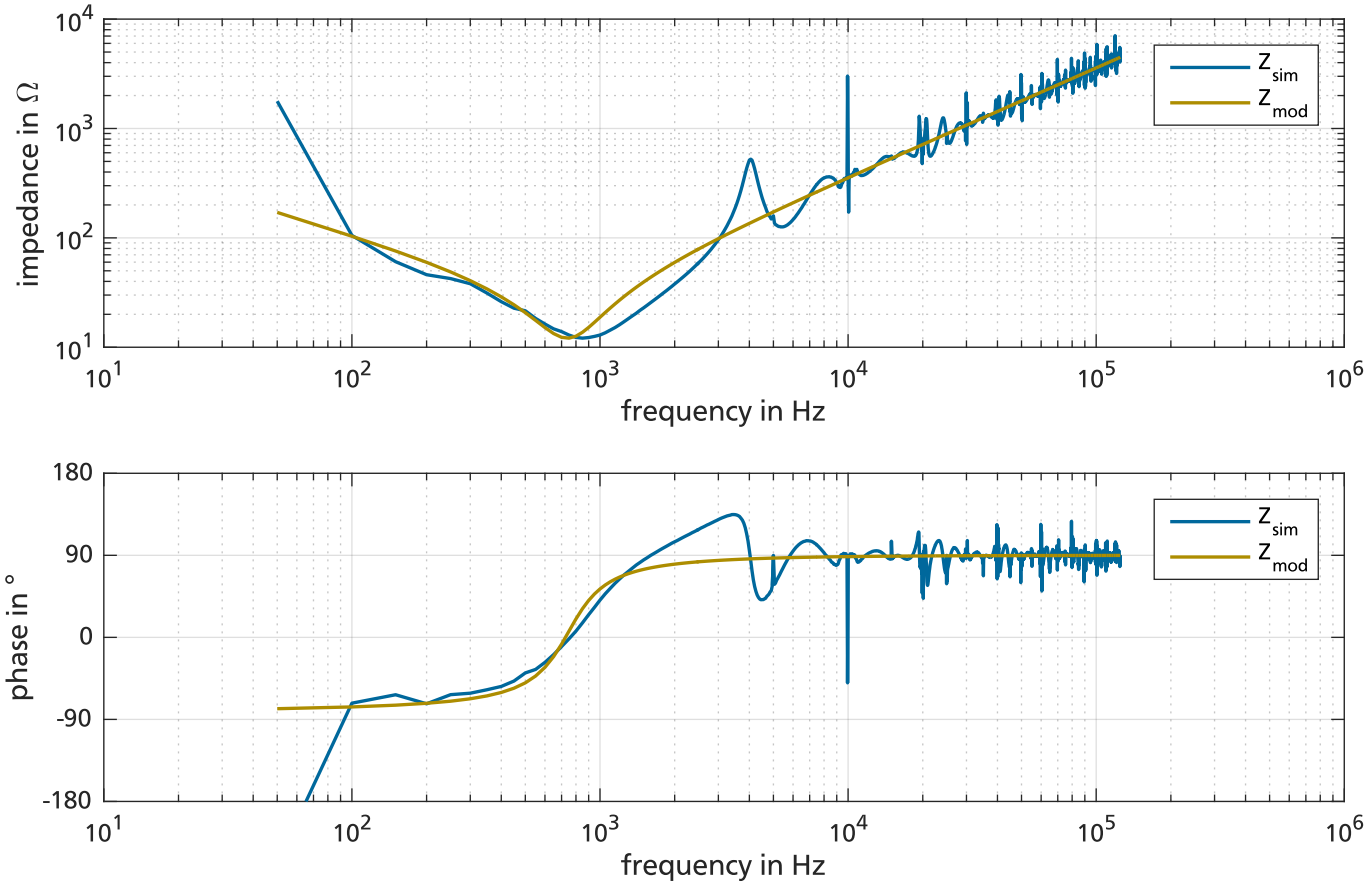

Figure 5.22.: Simulated impedance of a converter

Towards low frequencies the impedance of the converter increases and the impedance never drops below 10 Ω. The low frequency increase is due to the controller suppressing all low frequency currents into the converter. The general shape of the simulated impedance resembles a series connection of a capacitive and inductive impedance with resistive damping. Z_{DM} in figure 5.21 can be replaced by a resistance and capacitance, which depend on the control parameters of the VOC controller design. The inductive component is realized by the separate grid choke model.

6 Simulation of two converters in different environments

Figure 6.1 provides the structure of the two converters simulated in this chapter. One converter acts as noise source and the resulting behavior of the complete circuit is analyzed. The components on the noise sink side as well as the cable on the noise source side are varied in order to find a setup which is most likely to show resonant behavior. The simulation calculates all currents and voltages in the network resulting from an excitation at the source converter allowing to derive other values as well, such as impedances and current dampings through parts of the circuits. The PCC impedance Z_{PCC}, sink impedance Z_{sink} and current transmission from source to sink $\frac{i_{\mathrm{sink}}}{i_{\mathrm{source}}}$ are shown as examples in figure 6.1 using arrows.

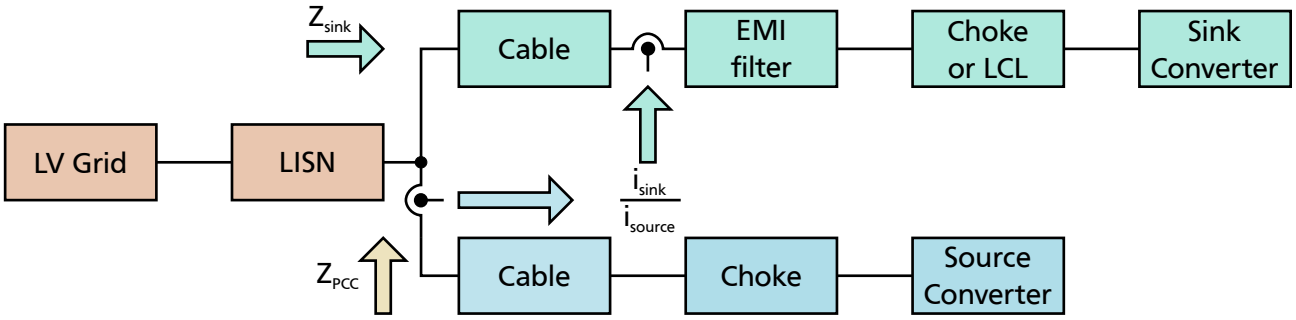

Figure 6.1.: Structure of the simulated converters

Table 6.1 provides the variations of each component used resulting in 512 different setups which were all simulated in a frequency range from 50 Hz to 500 kHz once with an excitation at the noise source in the form of a differential mode voltage and once with a common mode voltage. Additional variations beyond the ones listed in table 6.1 are performed for some of the results in the following sections.

Table 6.1.: Component Variations used in Simulation

component	variant 1	variant 2	variant 3	variant 4
source cable	2.5 mm shielded: 0 m, 100 m, 200 m, 400 m	6 mm unshielded: 0 m, 100 m, 200 m, 400 m		
sink cable	2.5 mm shielded: 0 m, 100 m, 200 m, 400 m	6 mm unshielded: 0 m, 100 m, 200 m, 400 m		
sink filter	none	2^{nd} order	3^{rd} order	4^{th} order
sink grid connection	L	LCL		

The models of grid and LISN as well as the source components are set up according to the models from chapter 5. The noise sink EMI filter, choke and LCL filter are generically sized based on component measurements but do not resemble a specific physical component. The parameters of the components in each variant are given in appendix A.

In order to analyze the system behavior, quantities which are independent of a specific specter created by the noise source converter, are examined. This leads to an analysis of impedances or admittances in the network. Also transfer functions from the generated voltage at the noise source to currents or voltages at other points of the network can be determined, having either no unit or being an admittance.

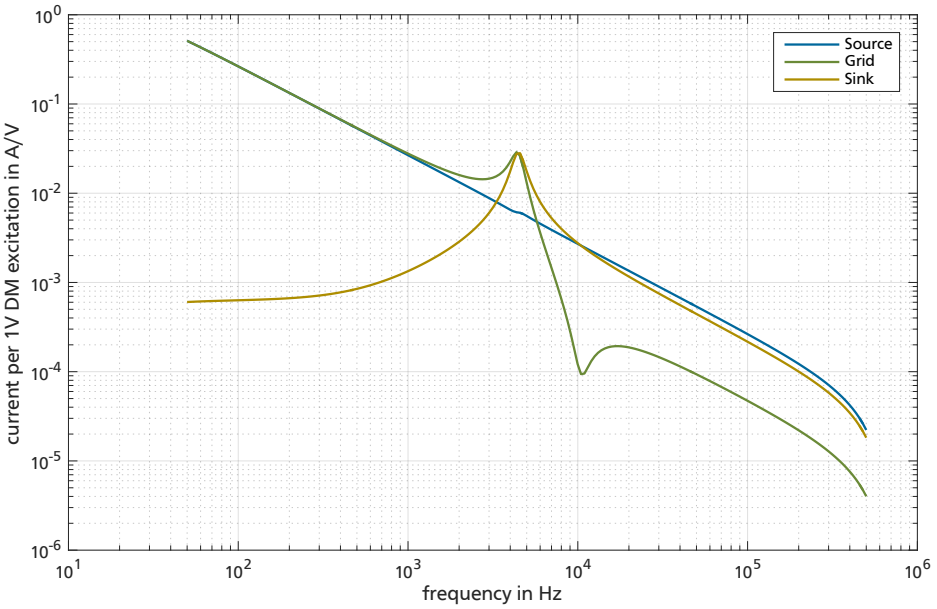

Figure 6.2.: Current distribution at the PCC

Figure 6.2 shows the currents at the PCC in relation to the voltage generated by the noise source converter between 50 Hz and 150 kHz. The unit is therefore an admittance.

The source admittance is dominated by the admittance of the source converters choke and falls with a factor of 10 per decade. At low frequencies the whole current from the source flows into the grid, at frequencies above 10 kHz it flows into the filter.

At and around 4.3 kHz the currents into the grid and into the filter are both larger than that from the source. This can no longer be considered a simple current sharing, but rather resembles a resonant point between grid inductance and filter capacitance which is excited by the noise source converter.

The main purpose of the following sections is to analyze the influence of different parameters and components on this resonance.

6.1 Influence of filter structure

Figure 6.3 shows the current generated per volt DM excitation at the noise source converter for different second order EMI-filters. For all graphs a clear maximum is visible, which is at the resonance frequency between grid and X-capacitors introduced in figure 6.2. The size of the capacitive stage of the filter is varied as labeled in the figure. The ratio of C_X to C_Y is kept constant at a value of 6.

The resonant point in figure 6.3 clearly shifts in accordance with the value of capacitance. Doubling the capacitance decreases the resonance frequency by a factor of $\sqrt{2}$ resembling a typical resonant behavior in accordance with the well known parallel LC resonance:

$$\omega_{\text{res}} = \frac{1}{\sqrt{L \cdot C}} \tag{6.1}$$

Although the resistance of the filter capacitors is scaled in accordance with section 5.2 with the value of capacitance, all resonances have the same amplitude of 48 mA per volt excitation voltage. The amplitude of the resonance is therefore independent of the capacitance or capacitor used.

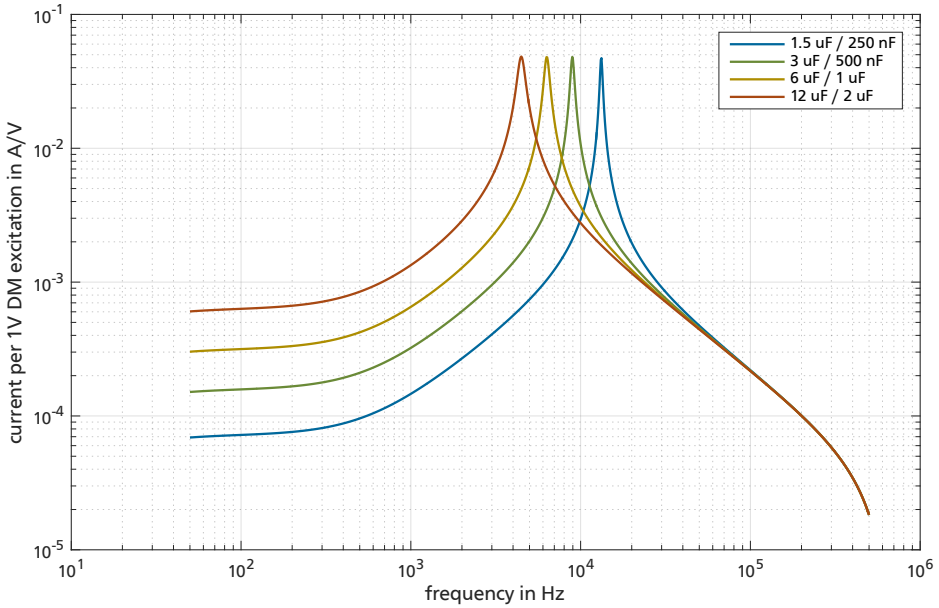

Figure 6.3.: Dependency of the DM resonance on value of C_X/C_Y capacitors

Figure 6.4 shows the currents through the Y-capacitors for different sizes of the filter capacitors. The resonance frequency is directly dependent on the capacitor value as in the DM case.

The amplitude differs without showing a certain trend. This is due to the frequency resolution being too small rather than a physical phenomenon. The inductance forming the CM resonance must have a significantly larger quality factor than that of the differential mode resonance, resulting in much sharper resonance peaks. Accurately resolving those would require significantly more frequency points.

Figure 6.5 shows the influence of the filter order on the DM resonance. While increasing the stages according to figure 5.8 the total amount of capacitance is kept constant. Hardly any influence on the resonance itself can be observed. The curves show small deviations above 20 kHz, which is negligible in practice due to the low amplitudes.

The CM resonance in figure 6.6 shows a dependency on the filter structure. The filters of 2$^{\text{nd}}$ and 3$^{\text{rd}}$ order behave exactly the same since the additional capacitive stage was designed without Y-capacitance and the reduced X-capacitance in the second capacitive stage was compensated by increasing the Y-capacitance in this stage accordingly to acchieve the same CM behavior. As the grid side Y-capacitor is not equipped the filter can be considered 3$^{\text{rd}}$ order concerning DM but remains 2$^{\text{nd}}$ order concerning CM.

In case of the 4$^{\text{th}}$ order filter the curve changes significantly. There are now two resonances, both at higher frequencies than for the lower order filters. The placement of the resonances depends strongly

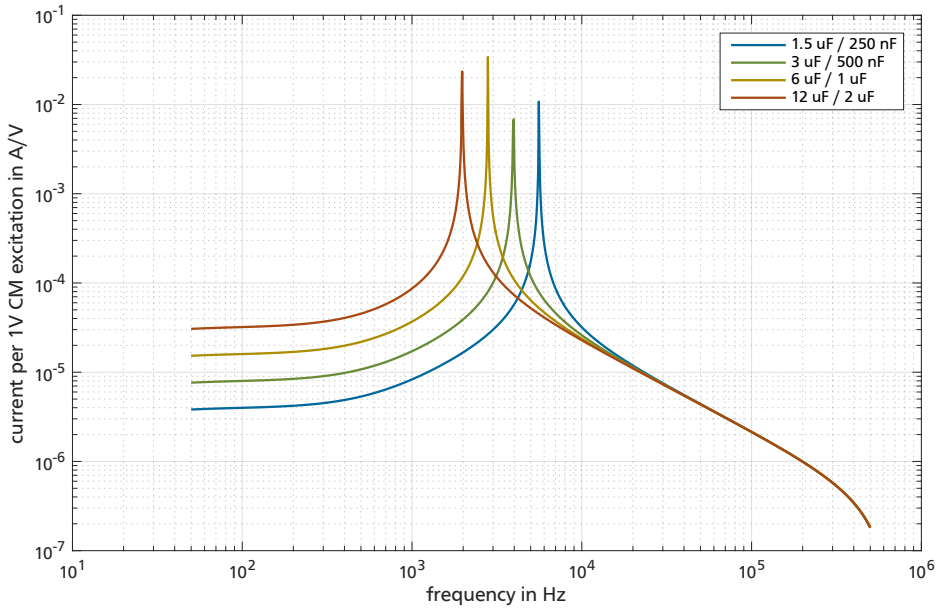

Figure 6.4.: Dependency of the CM resonance on value of $C_{\mathrm{X}}/C_{\mathrm{Y}}$ capacitors

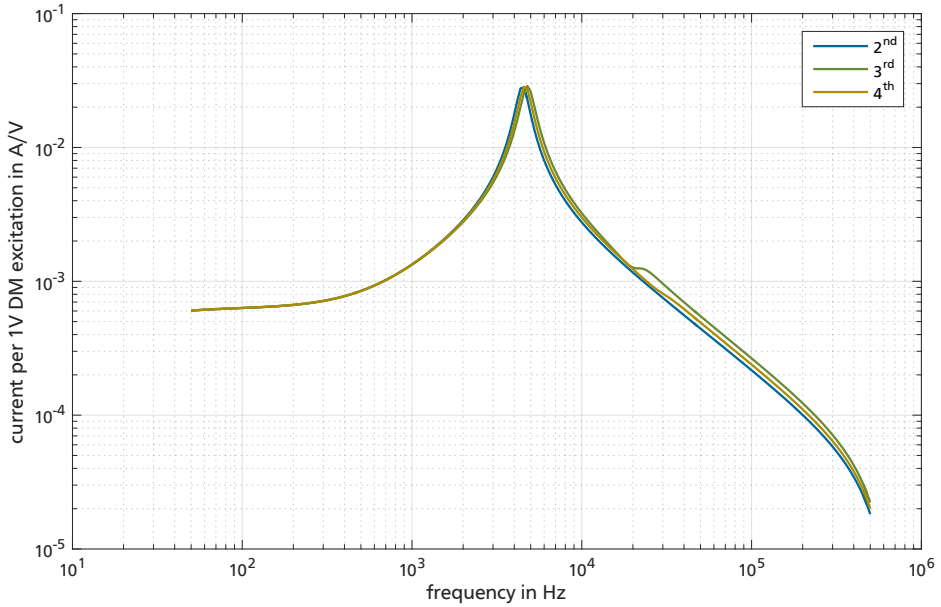

Figure 6.5.: Influence of filter order on DM resonance

on the actual design of a filter. In this case the capacitive and inductive stages of the 2nd order filter were simply split equally into two stages, each resulting in the depicted waveform. In practice the actual placement of the resonances is in the hand of the filter designer.

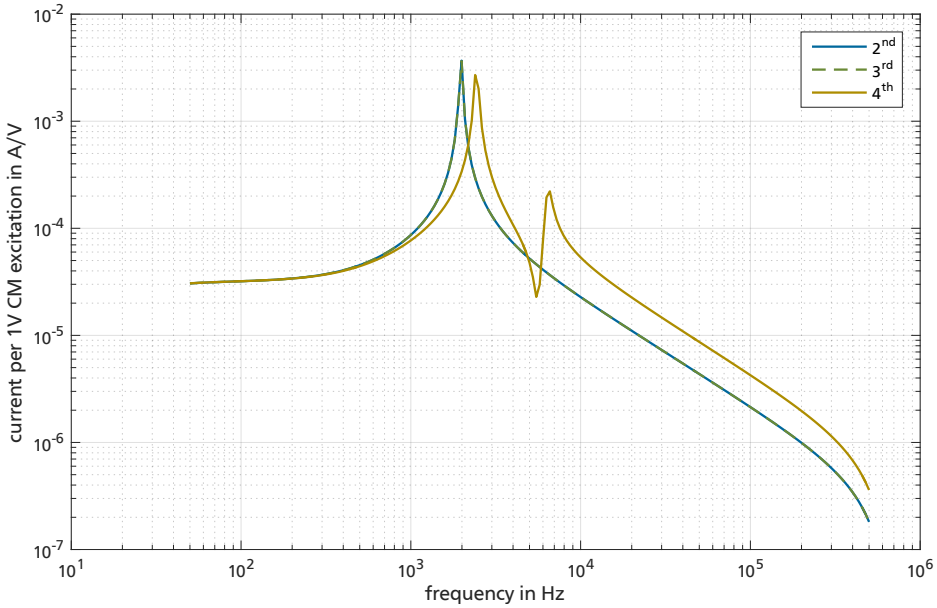

Figure 6.6.: Influence of filter order on CM resonance

From this section the following conclusions can be drawn:

- The DM resonance only depends on the total amount of X-capacitance, not the arrangement of the capacitances.
- The stray inductance of CM inductors and resistive components within the filter have close to no influence on the DM resonance. The damping of the DM resonance depends on components outside the filter.
- The CM resonance depends on the Y-capacitance used and on the filter structure as it is formed by the CM inductance and the filter capacitors.
- In this example the CM resonance is very sharp but since it is formed exclusively by filter components the resonance can be considered during filter design.

6.2 Influence of grid impedance

In section 6.1 the grid was modelled according to the measurements described in section 5.4. Two additional scenarios were simulated to observe the effect of the grid impedance on the resonance. If the standard grid impedance is $Z_{\text{grid}} = R + j\omega L$ the two cases are defined as:

- high L: $Z_{\text{grid}} = R + 5 \cdot j\omega L$
- high Z: $Z_{\text{grid}} = 5 \cdot R + 5 \cdot j\omega L$

IEC 60725 defines the grid impedance as a 240 mΩ resistance with 470 μH inductance and is also considered as grid impedance for simulation in this work [IEC12] .

Figure 6.7 shows the influence of the grid impedance on the DM resonance. By increasing the grid inductance the resonance is shifted to lower frequencies, demonstrating that the resonance is determined by the grid inductance together with the filter capacitors. Increasing also the grids resistance, strongly damps the resonance amplitude. The grid impedance has a strong influence on the possibility of DM resonances.

Using a LISN has a similar influence on the low frequency behavior as increasing the grid impedance, which can be explained by analyzing the LISNs structure in figure 5.20. Below 9 kHz [1] the LISN is not resembled by its standardized impedance but is dominated by the series inductances and slightly damped by the shunt resistors. This results in an impedance similar to a low quality factor inductance.

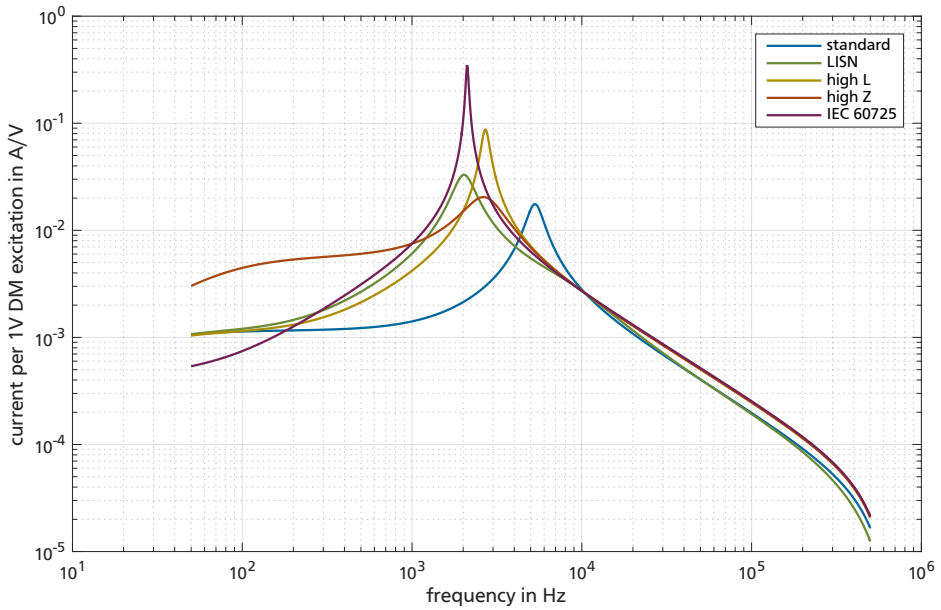

Figure 6.7.: Influence of different grid impedances on the DM resonance

Figure 6.8 shows the influence of different grid impedances on the CM resonance and substantiates the findings that the CM resonance is an internal filter resonance. The grid impedance has no influence on the resonance frequency and only small influence on the amplitude at the resonance. Very small grid impedances should be able to decrease the resonance amplitude as the grid impedance resembles a loading of the resonant circuit as a parallel impedance.

6.3 Influence of noise sink impedance

So far all above considerations were done for the special case that the converter can be represented by an open circuit. This situation could either appear in case of an idle converter or in case that the converter is disconnected from the grid by a circuit breaker placed behind the filter in order to avoid inrush currents at turn on that might trigger a RCD.

[1] the utilized LISN fulfills the standard between 9 kHz and 30 MHz, but LISNs covering only higher frequencies are also available on the market

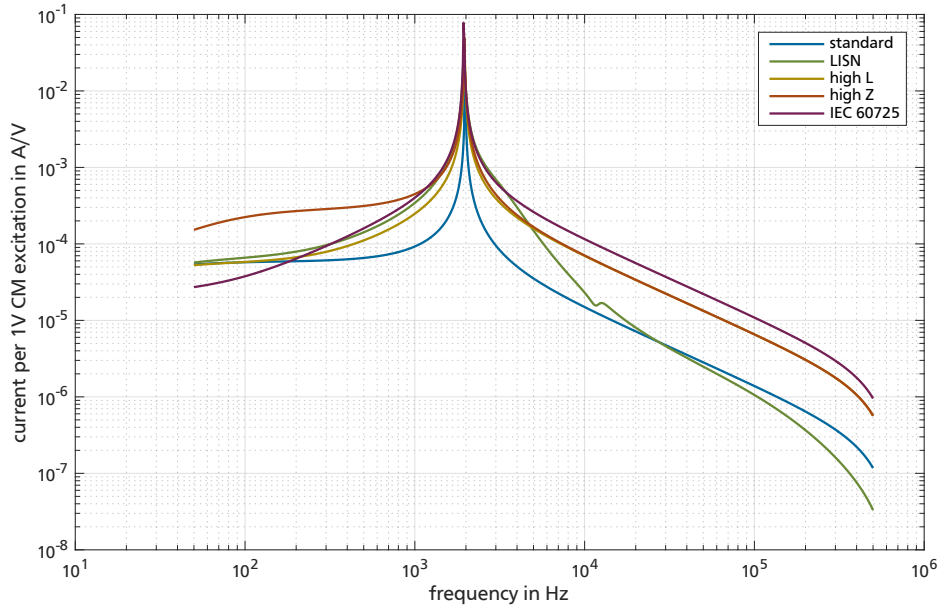

Figure 6.8.: Influence of different grid impedances on the CM resonance

This special case does not cover the operation time of the converter which is examined in this section. Figure 6.9 is used to study the influence of components in the noise sink converter path on the differential mode resonance between filter capacitors and power grid. The left figure compares the previously considered open circuit to an operating converter as described in section 5.5 connected through an inductor. Although additional currents flow past the filter capacitors into the converter, the current through the filter capacitors due to voltage generated at the noise source converter stays equal to the case with an open circuit EMI filter.

The right sub-figure of figure 6.9 shows the EMI filter capacitor currents generated by the noise source converter in case the choke is replaced by an LCL filter. This change as well as the use of an active or idle converter has no influence on the main resonance. Around 800 Hz an additional smaller resonance appears due to the resonance of the LCL filter. This resonance is damped by the utilized VOC controller running at 10 kHz due to the large control bandwidth compared to the LCL resonance. More complex controller design would be necessary to damp LCL resonances closer to the control bandwidth. Since the additional influence of the LCL filter on the EMI filter capacitor currents is negligible either way, this will not be analyzed further.

Figure 6.10 shows the CM results for the same variations of the circuit as figure 6.9 did for DM. The resonant capacitor currents at 2 kHz are not influenced by the converter being idle or active or by the choice between LCL filter and inductance. Since the capacitive stage of the LCL filter has no connection to protective earth this is the expected result. An active converter and its parasitic (or intentionally designed) capacitance to PE however add a small resonance around 10 kHz, which does not influence the EMI filter capacitors significantly.

The above analysis shows that an EMI filter with open secondary shows the same resonant behavior as with an active converter connected through an LCL filter or inductor. For an analysis of passive resonances between EMI filters and the grid all other components of the converters do not need to be considered.

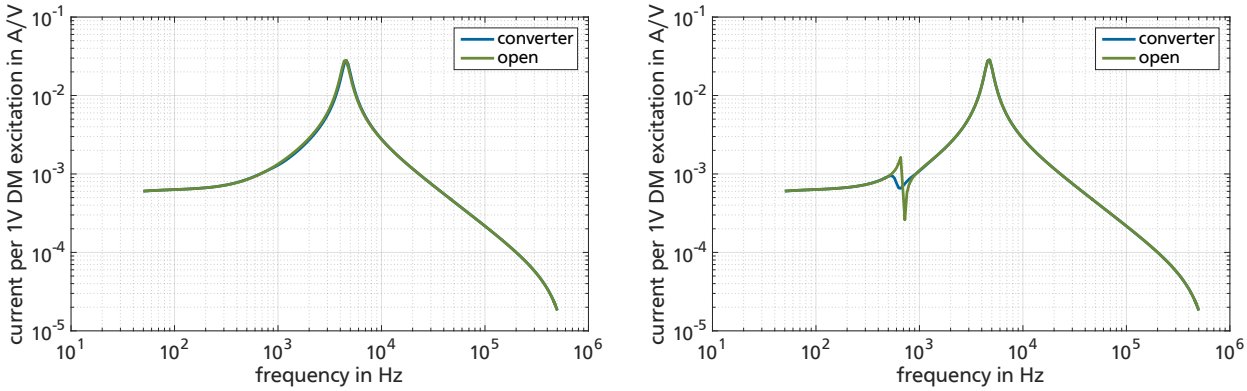

(a) L **(b)** LCL

Figure 6.9.: Influences of components of noise sink on DM resonance

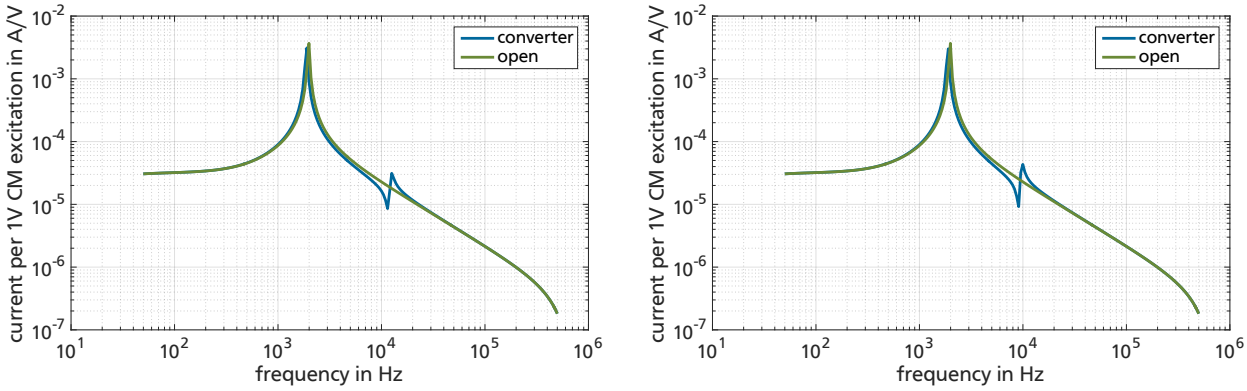

(a) L **(b)** LCL

Figure 6.10.: Influences of components of noise sink on CM resonance

6.4 Influence of cables

Since the resonance appears between the grid inductance and the EMI-filter capacitors a significant effect of components connected between those two components is expected. This section therefore focuses on different cables of varying length connecting the noise sink path to the PCC (see figure 6.1).

Figure 6.11 shows the DM current generated in the filter capacitors per 1 V excitation at the noise source converter when up to 400 m of the cables described in subsection 5.3.3 are used to connect the noise sink converter. In case of the unshielded 6 mm^2 cable increasing the length from 0 m to 400 m shifts the resonance frequency from 4.5 kHz to 3.2 kHz and decreases the amplitude by a factor of 1.5. In case of the 2.5 mm^2 shielded cable similar results can be observed. While the shift of frequency caused by the inductive component of the cable is only slightly larger, the damping of the resonance is about twice as large due to the higher resistance of the cable with less conductor area.

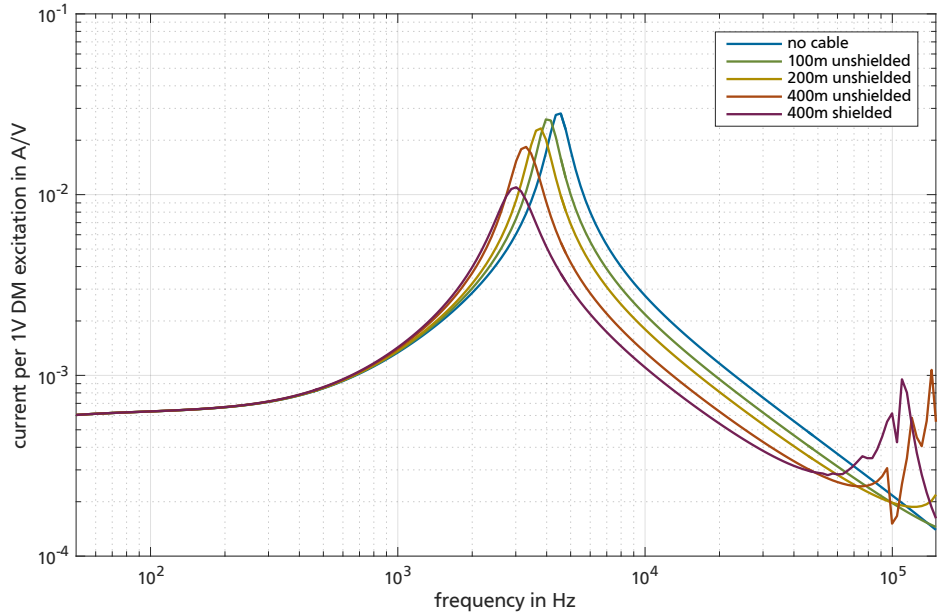

Figure 6.11.: Influence of different cables on the DM resonance

Figure 6.12 shows the influence of the same cables on the common mode current through the EMI-filter capacitors. The resonance frequency is not influenced by the cables used. Since the inductive cable is connected in series with the common mode choke at the filter input its additional inductance is negligibly small. A damping effect is visible for long cables but not as large as in the DM case. Since the CM resonance is formed by a much larger inductance, larger resistance is necessary to achieve similar damping.

As described in detail in section 5.3, cables with more than three conductors are asymmetrical components. This means that applying a signal containing only one sequence (compare subsection 3.2.1) will be transformed into several sequences. This means that the excitation with differential mode (or common mode) at the noise source will lead to both differential mode currents and common mode currents throughout the network. To evaluate how strong this influence is, the impedance into the noise sink converter with a 400 m, 2.5 mm^2 is shown in figure 6.13. The trend of the impedances remain the same although significant differences can appear around and above the DM resonance.

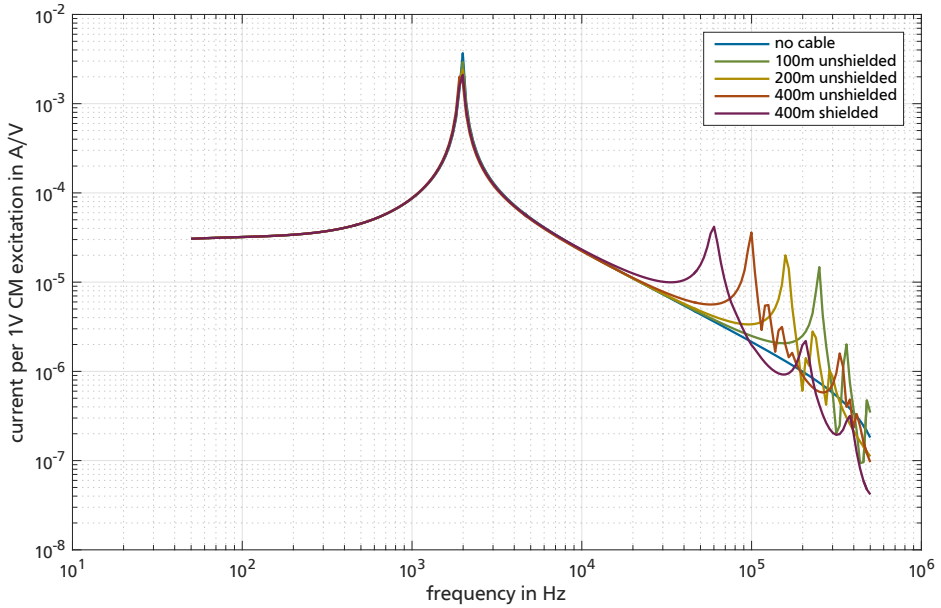

Figure 6.12.: Influence of different cables on the CM resonance

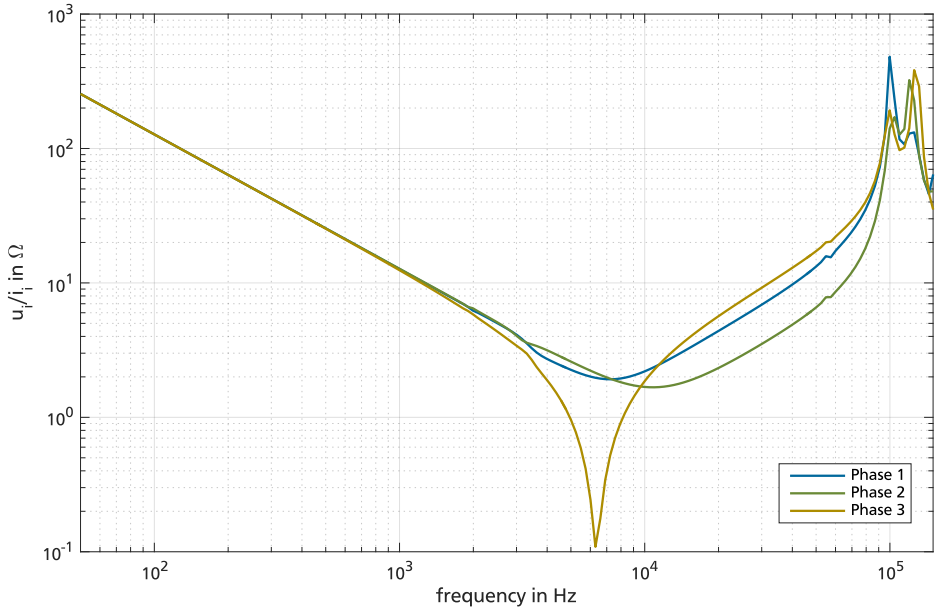

Figure 6.13.: Asymmetry of impedance into converter path if connected through $400\,\mathrm{m}$, $2.5\,\mathrm{mm}^2$ shielded cable

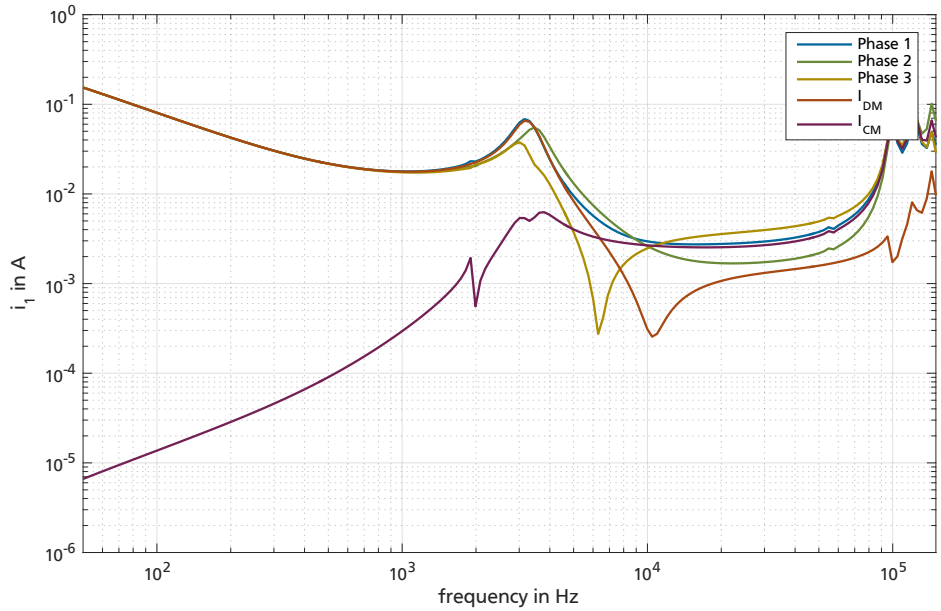

Figure 6.14.: Asymmetry of currents into converter path if connected through 400 m, 6 mm^2 unshielded cable

Figure 6.14 shows the three phase currents into the 400 m unshielded cable, which is the most asymmetrical type of cable considered in this work, and the DM and CM currents calculated according to the following formulas.

$$I_{\mathrm{CM}} = \frac{1}{3} \cdot (I_1 + I_2 + I_3) \tag{6.2}$$

$$I_{\mathrm{DM}} = \frac{1}{3} \cdot (2 \cdot I_1 - I_2 - I_3) \tag{6.3}$$

At low frequencies the DM voltage excitation generates only DM currents. At frequencies above 6 kHz the common mode current into the noise sink converter path exceeds the differential mode current although the system is excited by DM voltage only. For shorter cables and shielded cables this effect is decreased and the DM current is predominant for larger frequencies. Even in the worst case in figure 6.14, the highest phase current at the DM resonance at 3 kHz is still well represented by the DM current.

Cables are capable of having impact on higher frequency resonances if they reach a significant length. For the low frequencies observed in this work a consideration of possible asymmetries by calculation of DM or CM components from the phase values is sufficient.

7 Measurements

The simulated variants of chapter 6 have to be decreased to a reasonable amount to verify the results by measurement. Additionally the measured signals are decreased to the values found relevant by simulation. This chapter covers measurements of the currents through the filter capacitors in terms of the voltage generated by the noise source converter in section 7.1 for different switching frequencies of the noise source converter. Additionally the effect on the PCC voltage is presented in section 7.3 in case the resonance is excited. Extending beyond the simulated electrical behavior, the thermal influence on the filter capacitors is analyzed in section 7.2. Because the CM resonance found is an internal resonance of the filter and can be considered during the filter design, all measurements focus on the DM resonance.

In order to measure the filter currents a filter PCB has been designed, that incorporates current shunt resistors in series with every capacitor. The value of those resistors was chosen as 8 mΩ and the measurement across the resistors is measured with 1:1 differential probes. The voltage measurement at the noise source converter is realized with 1:100 passive probes connected to the floating potentials of the gate driving circuits of the high sides of the IPM (Intelligent Power Module). The shields of the passive probes are not connected and the PE connection of the oscilloscope is used as reference.

All electrical measurements are taken over a period of 100 ms with a sample rate of 10 MHz and transformed to frequency domain by a DFT.

Section 7.1 shows the measured DM resonance with LISN to prove the simulation accuracy for a well known scenario. The subsections then analyze the influences on the resonance if no LISN is used, being the more realistic scenario. Section 7.2 analyzes the thermal impact on the filter capacitors by the resonant currents. Section 7.3 shows the voltage at the PCC when the converter is operated in different resonant conditions.

7.1 Parallel resonance between X-Capacitors and Grid inductance

Figure 7.1 shows the simulated current transmission as a solid line and measured values as stars. The measured points are acquired by setting different switching frequencies of the noise source converter. From the determined specters only relevant points, well beyond the noise floor, in both current and voltage are selected for the plot. This results in several results at the sidebands of the multiples of the switching frequency.

By careful selection of different switching frequencies the simulated behavior can be proven well within the desired frequency span. Figure 7.1 shows the DM transmission in case a LISN is used and all measured components described in chapter 5 are used. The measurements are very consistent with the simulation, proving the accuracy of the simulation and modeling.

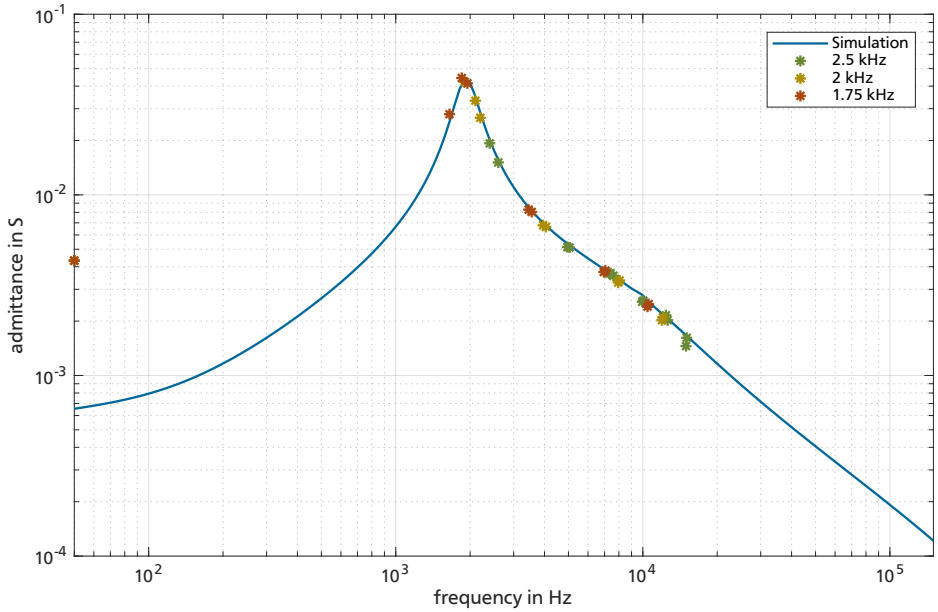

Figure 7.1.: Measurement of resonance with LISN

7.1.1 Influence of filter capacitance

This subsection describes the influence of the filter capacitance on the DM resonance. For this purpose two 2nd order filters according to section 5.2 are used with the same common mode choke (3.4 mH + 14 mΩ) but different capacitances according to table 7.1.

Table 7.1.: Capacitance values of used filters

Cx	Cy
4.4 μF	0.68 μF
12.3 μF	1.9 μF

The resulting measurements and simulations are shown in figure 7.2. From simulation a shift of the resonance frequency from 9 kHz to approximately 5.3 kHz by increasing the capacitance according to table 7.1 is expected. A change in amplitude is not expected. The measurements match those expectations well. Simulation and measurement of the smaller filter match exactly, whereas the larger filter has some small deviations.

A slight increase in the resonance amplitude can also be observed in case of the measurement, which is not expected from simulation. Due to the few samples around the resonance frequencies the accuracy of such a small increase is questionable, however. The error made by neglecting the influence of the filter capacitance on the resonance amplitude is insignificant compared to the change in frequency.

Some measurement points above 50 kHz show significant deviation from the simulation. This effect could either be due to ignored non-idealities in the simulation or measurement errors at higher frequencies, where the selected harmonic content is much closer to the noise floor than at lower frequencies.

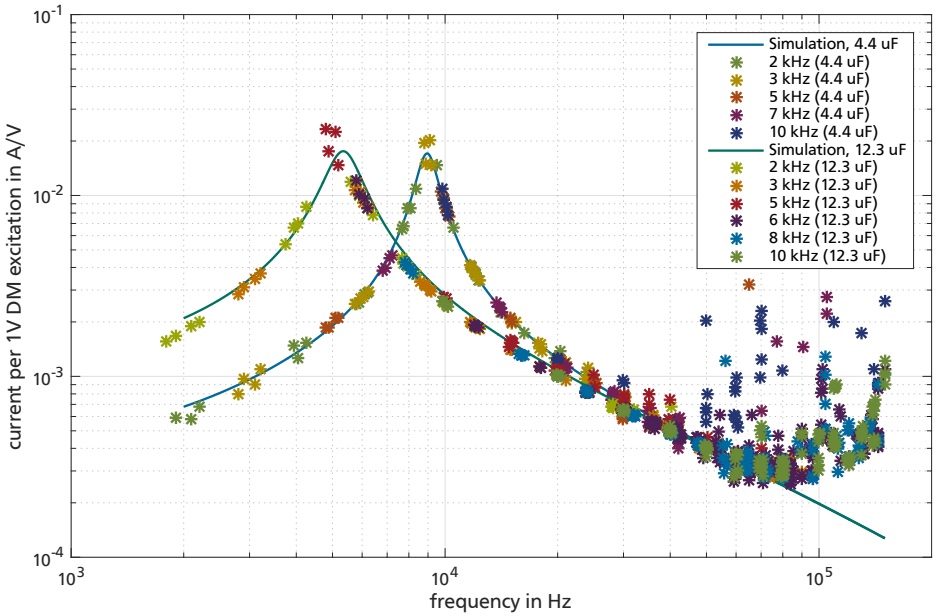

Figure 7.2.: Measured influence of filter capacitance on resonance

7.1.2 Influence of grid impedance

The first measurement results without the use of a LISN were found to be very different than the expectations from the simulation. All measured resonance frequencies were larger than their simulated counterparts and had a significantly smaller amplitude. Since the influence of the grid impedance is eliminated by the use of a LISN and deviations are not visible in this case, the decision was made to adjust the grid impedance from section 5.4 to match the resonance measurements. The following values were found to lead to good matching between simulation and measurement and are closer to the values from the initial measurement than the assumptions made for the simulation (compare table 5.4). Also the simulated graphs displayed in subsection 7.1.1 use this adapted grid impedance.

- $R_{\text{grid}} = 550\,\text{m}\Omega$
- $L_{\text{grid}} = 54\,\mu\text{H}$

Comparing those values to the grid impedance specified in IEC 60725 as 240 mΩ with 470 µH [IEC12] shows a 20 times higher quality factor of the standardized grid inductance over the actual grid inductance at the test bench used in this work. The assumed quality factor in the standard might be too large, but nonetheless significantly less damped grids should be considered and expected when transferring the results of this work to other grids.

Figure 7.3 shows the simulation and measurement with the above grid impedance and an additional series inductance with a nominal value of 100 µH and a tolerance of 25 %. A good accordance between measurement and simulation with the standard laboratory grid impedance is shown. As predicted in section 6.2 an increase in grid inductance reduces the resonance frequency. As the resistance is not increased as much, the resonance amplitude increases significantly. The difference between simulation and measurement can be explained by the large tolerance of the used inductors, which exceed their nominal inductance. Measurement of the chokes showed inductances of 108 µH, 111 µH and 115 µH

leading to a stronger decrease in the resonances frequency than expected from simulation using their nominal inductance.

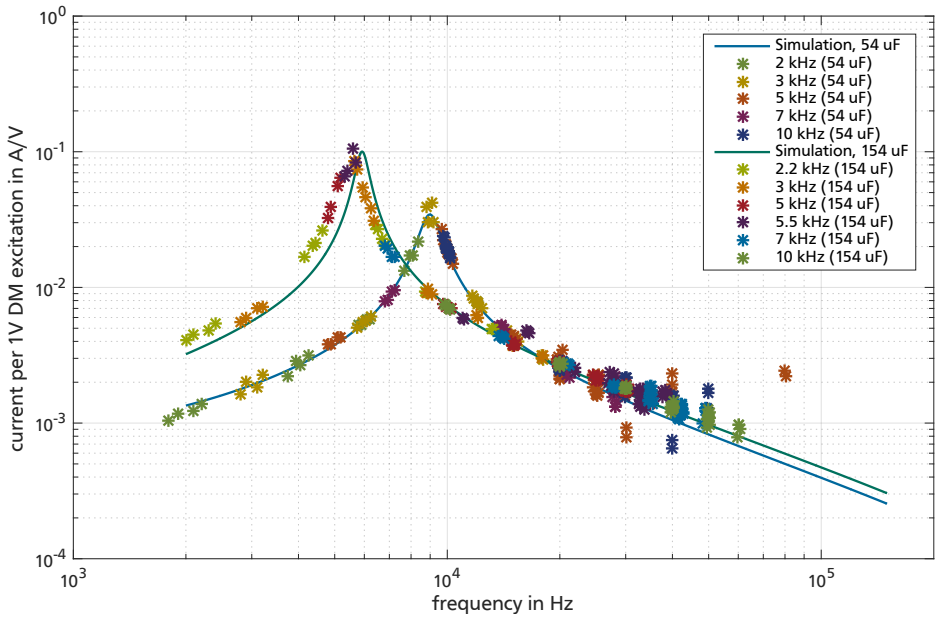

Figure 7.3.: Measured influence of grid impedance on resonance

7.1.3 Influence of noise source power rating

The value of a power choke is anti-proportional to the power of a converter, assuming a constant relative short circuit voltage. A converter of larger nominal power therefore creates proportionally more ripple currents than a converter of lesser nominal power if generating the same amount of fundamental current. Larger converters can be expected to excite a resonance at the PCC more.

Figure 7.4 shows the simulated and measured results in case the converter uses its full 5.4 mH inductor or only half (2.7 mH) the value. Both simulation and measurement clearly show that the disturbance created by a converter is proportional to its nominal power.

7.2 Thermal impact on filter capacitors

This section analyzes a filter thermally if a resonance is excited in the network. Unfortunately current ratings for EMI capacitors are typically not provided in their datasheets. Würth's FTXX series datasheet [Wue18] provides the designer with a maximal allowed temperature increase above the ambient temperature and was therefore selected for use in the test filters. The allowed temperature increase is specified at 7 K.

All measurements, including the thermal measurements, were taken with a filter under open circuit condition on its load side. The results found in this section therefore show the thermal influence of the resonance in an isolated manner. If an operating converter is connected to the grid through the filter, additional currents from this converter strain the filter capacitors.

While most operating points only resulted in temperature increases between 2 and 3 K, operating the noise source converter with a switching frequency of 5.5 kHz, with the hardware setup resulting in the

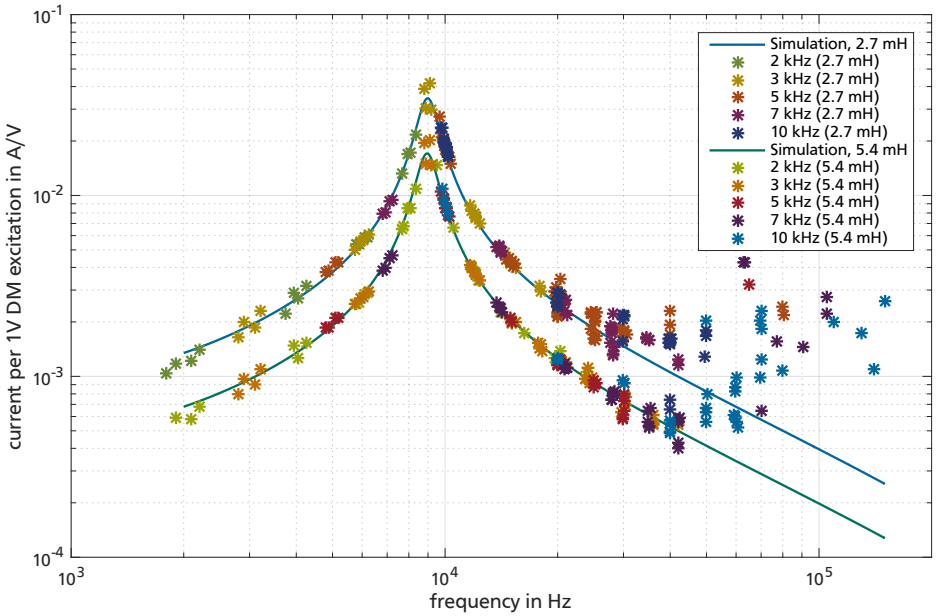

Figure 7.4.: Measured influence of noise source power rating on resonance

higher resonance in figure 7.3, significant heating of the filter capacitors can be observed. This operating point is characterized by the following three conditions in accordance with the findings from subsections 7.1.1 through 7.1.3:

- small filter ($C_{\mathrm{X}} = 4.4\,\mathrm{mF}$)
- increased grid inductance ($L_{\mathrm{grid}} = 154\,\mu\mathrm{H}$)
- larger noise source nominal power ($L_{\mathrm{source}} = 2.7\,\mathrm{mH}$)

Figure 7.5 shows the filter temperatures for this operating point after different operation times. In the back of the pictures the common mode choke can be recognized and its winding temperature is measured at the marker M3. The marker M2 determines the temperature of one X-capacitor, while M1 is placed on a non connected capacitor as reference measurement. Two additional hot spots are visible in the pictures, which are two of the three shunt resistors for current measurement. The routes on the PCB are clearly visible especially after 5 min. The hottest PCB spots are observed at the starpoint of the X-capacitors, which is located between the two visible shunt resistors.

Table 7.2 shows the temperatures at the markers and the difference between the marker M2 and M1, which is equal to the temperature increase of the X-capacitors. Clearly the CM inductors temperature is the largest in this example. Increasing the chokes temperature reduces it's saturation flux. While not the focus of this thesis it is possible that there are operating points, where this effect of the DM resonance leads to a saturation of the CM choke.

The temperature increase of the capacitors reaches 6.2 K after one hour. In the considered operating point the filter capacitors are stressed almost to the nominal allowed value by the neighboring converter alone. Additional stress from the converter of the filter would quickly result in thermal stress above the specified limit of 7 K. Typical ageing procedures of foil capacitors result in an increase in ESR, which in turn increases the temperature of the components. This positive feedback is likely to result in accelerated ageing of the filter capacitors.

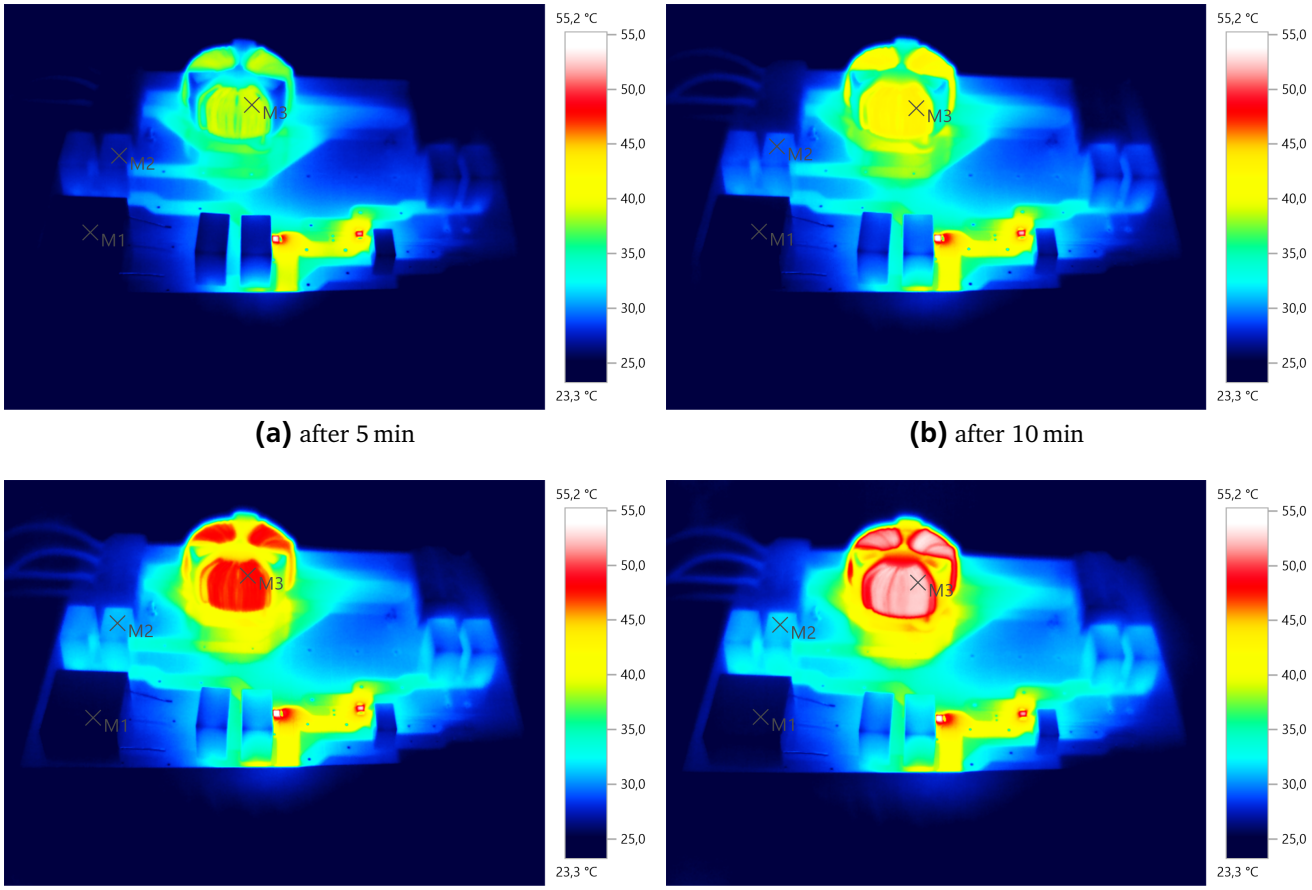

(a) after 5 min **(b)** after 10 min

(c) after 20 min **(d)** after 40 min

Figure 7.5.: Temperature of filter components over time

Table 7.2.: Temperatures in EMI filter

	5 min	10 min	20 min	40 min	60 min
M1	24.5 °C	24.7 °C	25.1 °C	25.5 °C	25.2 °C
M2	27.0 °C	29.0 °C	30.9 °C	31.6 °C	31.4 °C
M3	39.1 °C	43.3 °C	47.4 °C	52.5 °C	53.8 °C
delta (M2-M1)	2.5 K	4.3 K	5.8 K	6.1 K	6.2 K

The above scenario is expected to show a reduced lifetime of the EMI filters X-capacitors. If the grid was characterized by a larger L/R ratio, the filter size was reduced or the noise source nominal power was increased, the stress on the capacitors would increase until operating points with immediate destruction of the filter would be reached.

7.3 Impact on PCC voltage

Figure 7.6 shows one period of the voltage at the PCC in case the worst case resonance from section 7.1 is excited. A converter connected to this PCC and sampling this voltage would have to deal with significant sampling errors[1] depending on its sampling frequency. Depending on the sampling rate of a parallel converter also aliasing could appear and result in a resonance of its controller. Converter failure or protective disconnection are likely.

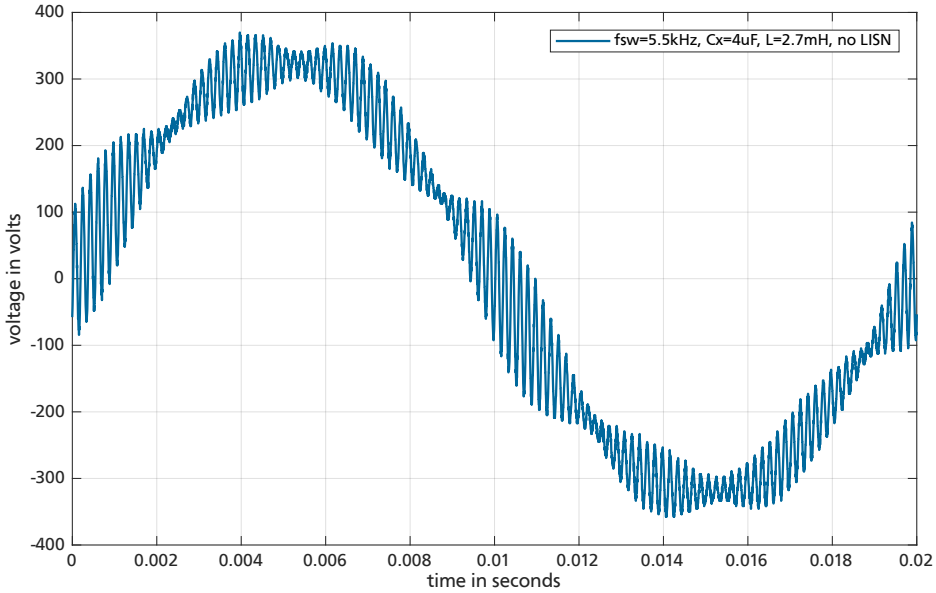

Figure 7.6.: Worst case PCC voltage in time domain

DIN EN 50160 [DIN11] describes the voltage characteristics of public distribution networks. Besides several other voltage disturbances it also defines harmonic voltage limits which can be expected to be complied with by the power network under regular operation conditions according to table 7.3.

Figure 7.7 shows the limits of DIN EN 50160 and the spectral content of the measured PCC voltages of different resonant operating points. The blue specter results from taking the smaller filter, the larger noise source and a LISN. In this case the large grid impedance results in large voltages at the PCC, which would clearly exceed the limits of the standard, if it extended into this frequency range. The same holds true for the other two more realistic operating points. The yellow specter represents the time domain signal from figure 7.6 and the thermal findings from section 7.2.

[1] as discussed in chapter 2

Table 7.3.: Supply harmonics according to DIN EN 50160 [DIN11]

uneven harmonics				even harmonics	
non-multiples of 3		multiples of 3			
order	relative voltage amplitude	order	relative voltage amplitude	order	relative voltage amplitude
5	6 %	3	5 %	2	2 %
7	5 %	9	1.5 %	4	1 %
11	3.5 %	15	0.5 %	6 to 24	0.5 %
13	3 %	21	0.5 %		
17	2 %				
19	1.5 %				
23	1.5 %				
25	1.5 %				

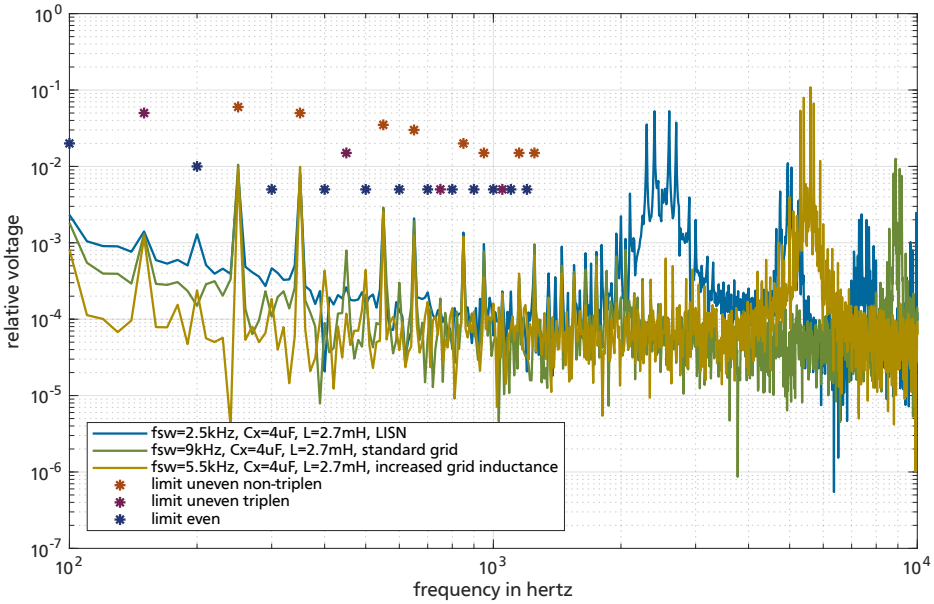

Figure 7.7.: Measured harmonic content at PCC for different setups

8 Discussion and Outlook

Section 8.1 of this chapter extracts and discusses the main findings from the simulations and measurements in chapter 6 and 7 respectively. Secondly a change in filter design is proposed and simulated in section 8.2, that realizes disturbance resistant converters.

8.1 Key findings

The key findings of the previous chapters are:

1. Common mode resonances were proven to be internal filter resonances (compare figures 6.4 and 6.8) as long as the first filter component on grid side is either a common mode choke or capacitive stage without Y-capacitors followed by a common mode choke. Because the impedance into such filters is several orders of magnitude larger than typical impedances at the PCC, this design is characterized by extreme robustness against external changes of the PCC impedance or connection through long cables (compare figures 2.5 and 6.12 respectively).

2. The differential mode behavior on the other hand depends strongly on the components surrounding the converter, since the resonance is formed by the total X-capacitance (compare figure 6.5) along with the grid inductance (compare figure 6.7).

3. Significant influence of cables on the DM resonance could be observed only for several hundreds of meters (compare figure 6.11). Capacitive components in close proximity in industrial networks therefore add up to a total capacitance at their PCC. This applies both to EMI filter capacitors and capacitors in LC filters. Only LCL filters can prevent this effect by increasing the impedance on grid side using the second inductor in analogy to item 1 of this list.

4. The amplitude of the resonant current is proportional to the nominal power of the converter stimulating the resonance and the damping of the grid (compare figures 7.2, 7.3 and 7.4). The capacitance has only minor influence on the amplitude (compare figure 7.2), therefore decreasing the amount of capacitance results in larger currents through each capacitor.

5. While significant disturbances appear in the PCC voltage if a resonance is excited (compare section 7.3), the filter capacitors may be able to withstand the currents generated by the resonance. Slight changes according to item 4 of this list brought the capacitors close to their specified thermal limit (compare section 7.2). Exceeding it should be possible just as easily, resulting in the destruction of the EMI filter.

The above findings are found using a simple setup consisting only of two converters connected in parallel. Using item 3 of the above list, a parallel connection of more than two converters can be described equally, provided that they are positioned closely, which would be the case in most industrial

grids. The larger the nominal power of one converter is, the higher are the currents resulting from an excitation. Considering many parallel converters an additional critical scenario becomes possible: Several converters of the same type might create the same specter, for example by utilizing the same switching frequency and synchronizing their PWM to the grid voltage, which would superposition constructively. The resulting effect would be equal to that of a converter of the combined power of all equal converters.

Item 4 could be used to justify that increasing the components with filters at a certain point eventually leads to a weakening of the resonance effects, as the amplitude of the resonant current is not influenced, but the current is distributed among more capacitors. This conclusion might be correct but ignores two important aspects. Primarily the problem of a distorted grid voltage remains with equal severity. Secondly the resonance frequency is decreased, eventually moving it into the classical power quality range below 2 kHz. A violation of standards is very likely in this case and an excitation by the harmonic content of line-commutated power electronic circuits becomes possible.

In general possible DM resonances can be considered when designing a system where all influences on the resonance are known. In most cases however, neither the grid impedance nor the capacitance at the PCC is known when designing a converter. Without even considering load changes with a resulting change in capacitance connected to the grid, both resonance frequency and amplitude are unknown at the design stage. The following section therefore proposes a design of the grid interface for converters that is robust against resonances, independent of the environment it is used in.

8.2 Prevention of resonance by variation of the converter structure

A common mode design with an inductive stage towards the grid resulted in a CM behavior mostly independent of the surrounding components as shown in figure 2.5. Transferring this to the differential mode case leads to the need for a differential mode inductance as first component connected to the grid, as is customary when using an LCL filter without an additional EMI filter. As soon as additional common mode damping is needed this advantage is lost by placing an EMI filter between the LCL filter and the grid. The proposition is therefore to integrate the EMI filter into the capacitive stage of the LCL filter. Figure 8.1 demonstrates this concept.

Since the first capacitive stage in converter side has no Y-capacitor the grid interface according to figure 8.1 realizes a 3$^{\text{rd}}$ order filter both for CM and DM.

Utilizing the same 2$^{\text{nd}}$ order EMI filter structure in the classical way between inductance or LCL filter and grid is shown in figures 8.2 and 8.3 respectively. With inductance a 3$^{\text{rd}}$ order CM and 2$^{\text{nd}}$ order DM damping can be achieved, whereas the LCL filter plus EMI filter realizes a 3$^{\text{rd}}$ order CM and 4$^{\text{th}}$ order DM damping. The proposed alternative design effectively looses one DM stage.

To compare the concepts 6 different converters were designed, realizing grid currents of 21 A and 50 A or 15 kW and 35 kW with each of the circuits in figures 8.1, 8.2 and 8.3. Each of the converters was simulated as noise source and noise sink according to section 5.5 resulting in 36 different simulations. The converter models and filter designs were done for the 21 A variant using a switching frequency of 25 kHz and the 35 kW variant one of 15 kHz.

Designing the grid interfaces according to the above topologies still leaves many degrees of freedom, which are reduced here by the following assumptions, using the nominal current I_{N} and the switching frequency f_{SW}:

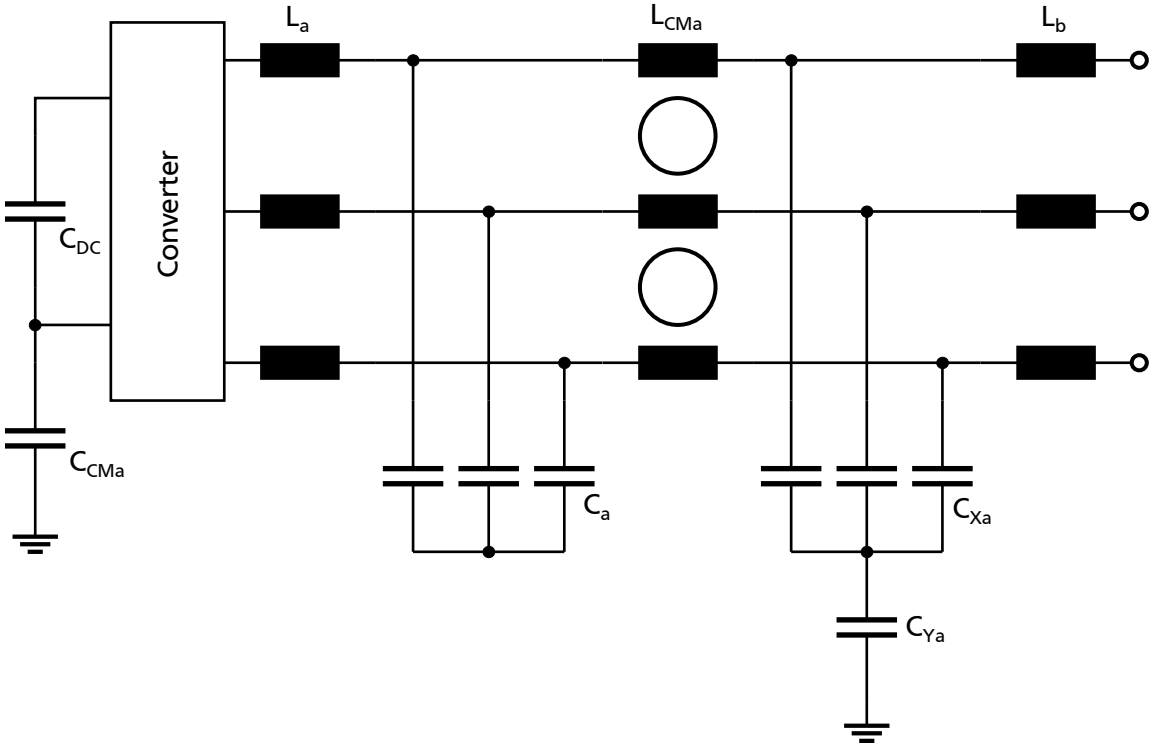

Figure 8.1.: Proposed design of LCL filter with internal EMI filter

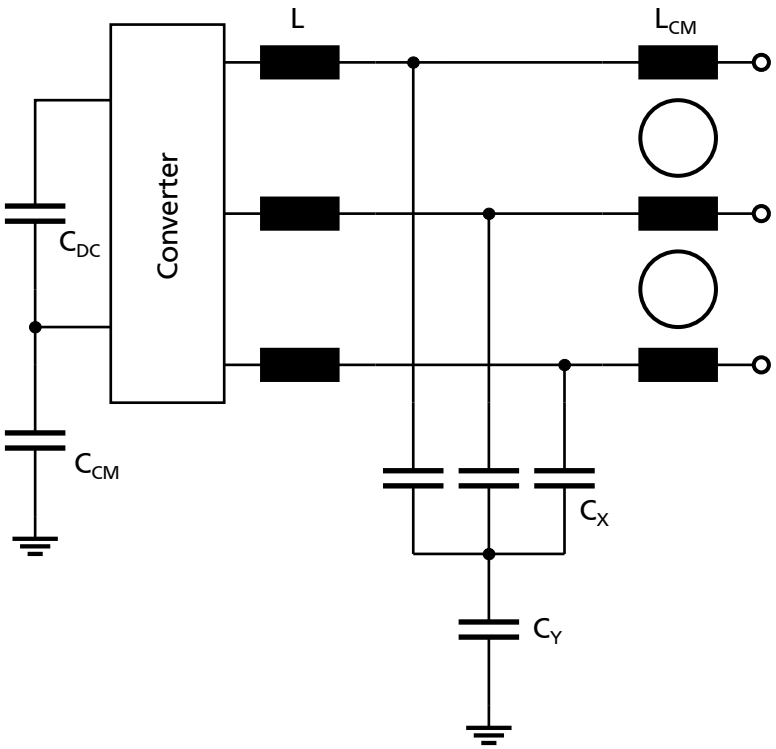

Figure 8.2.: Classical inductance with EMI filter

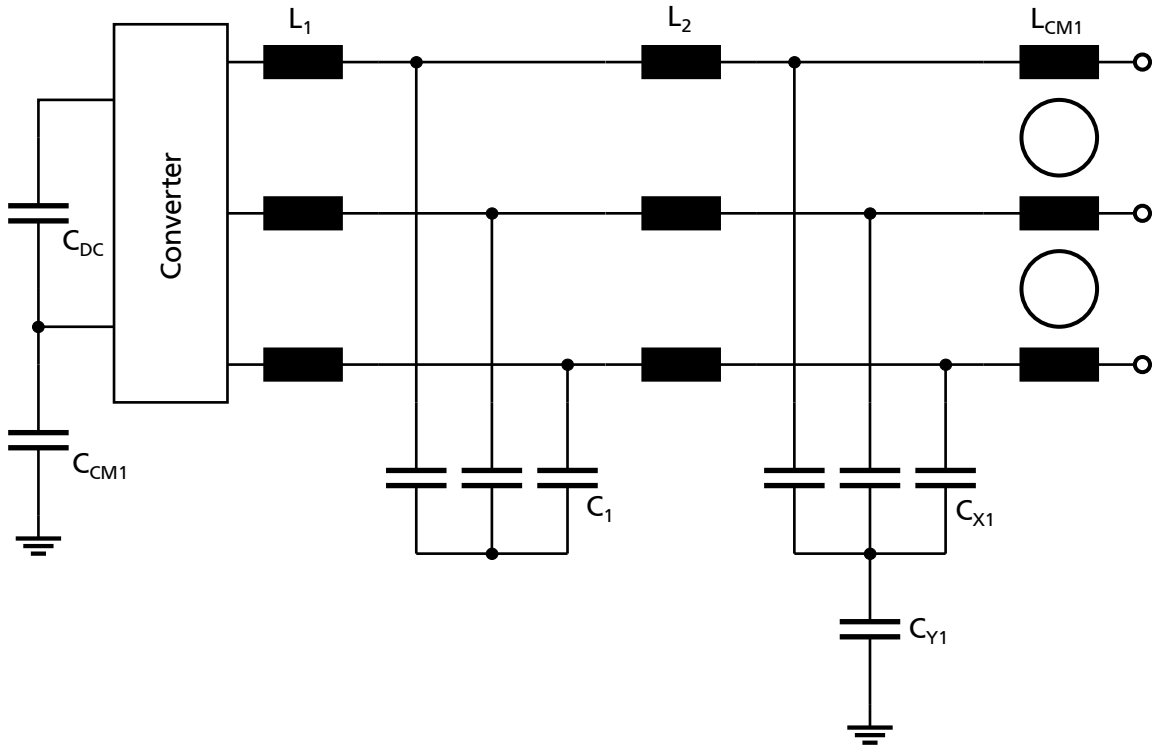

Figure 8.3.: Classical LCL with external EMI filter

- EMI filter CM inductance: $L_{\mathrm{CM}} = \frac{40\,\mathrm{mH\,A}}{I_{\mathrm{N}}}$
- EMI filter capacitance: $C_{\mathrm{X}} = 6 \cdot C_{\mathrm{Y}} = 120\,\mathrm{nF\,A^{-1}} \cdot I_{\mathrm{N}}$
- DC side CM capacitance C_{CM} to realize common mode resonance at $\frac{2}{3} \cdot f_{\mathrm{SW}}$
- choke inductance (L) with relative short circuit voltage of 8 %
- converter (L_1/L_{a}) and grid (L_2/L_{b}) side inductance of the LCL filter with relative short circuit voltage of 8 %/4 %
- capacitive LCL stage to place DM resonance of the LCL filter at $\frac{1}{8} \cdot f_{\mathrm{SW}}$

The resulting values and assumptions concerning their parasitic properties are listed in appendix B. Designing according to the above strategy leads to a reduction of the CM capacitance on the DC side and the capacitive stage of the LCL filter by integrating the EMI-filter into it. The loss of one order of DM damping is accompanied by a decrease in component size, leaving room for an optimization of the damping of the topology.

To evaluate the performance of the proposed grid interfacing topology the currents through the capacitors have to be evaluated.

At first the influence of the redesign of the LCL filter on the self-resonance and resulting current within the filter has to be analyzed and is shown in figure 8.4. One separate plot is done for each of the four converter types with LCL filter used as noise source converter here. Within each plot 6 traces are displayed, one for each of the previously designed converters connected as noise sink in parallel to the source converter. The traces show the total currents into the X-capacitors of the LCL filter, namely C_1 in figure 8.3 and $C_{\mathrm{a}} + C_{\mathrm{Xa}}$ in figure 8.1 per 1 V differential mode voltage generated by the converter.

Figure 8.4 shows that the type of parallel converter has no influence on the internal DM behavior of the filter, as all traces within each plot show no significant difference. Also the equivalence of the LCL filter with integrated EMI filter is shown for both current values because the resonance is not influenced. The controller design of an LCL filter with internal EMI filter does not change compared to one with an external EMI filter. In both cases the peaks have to be damped by the control algorithm.

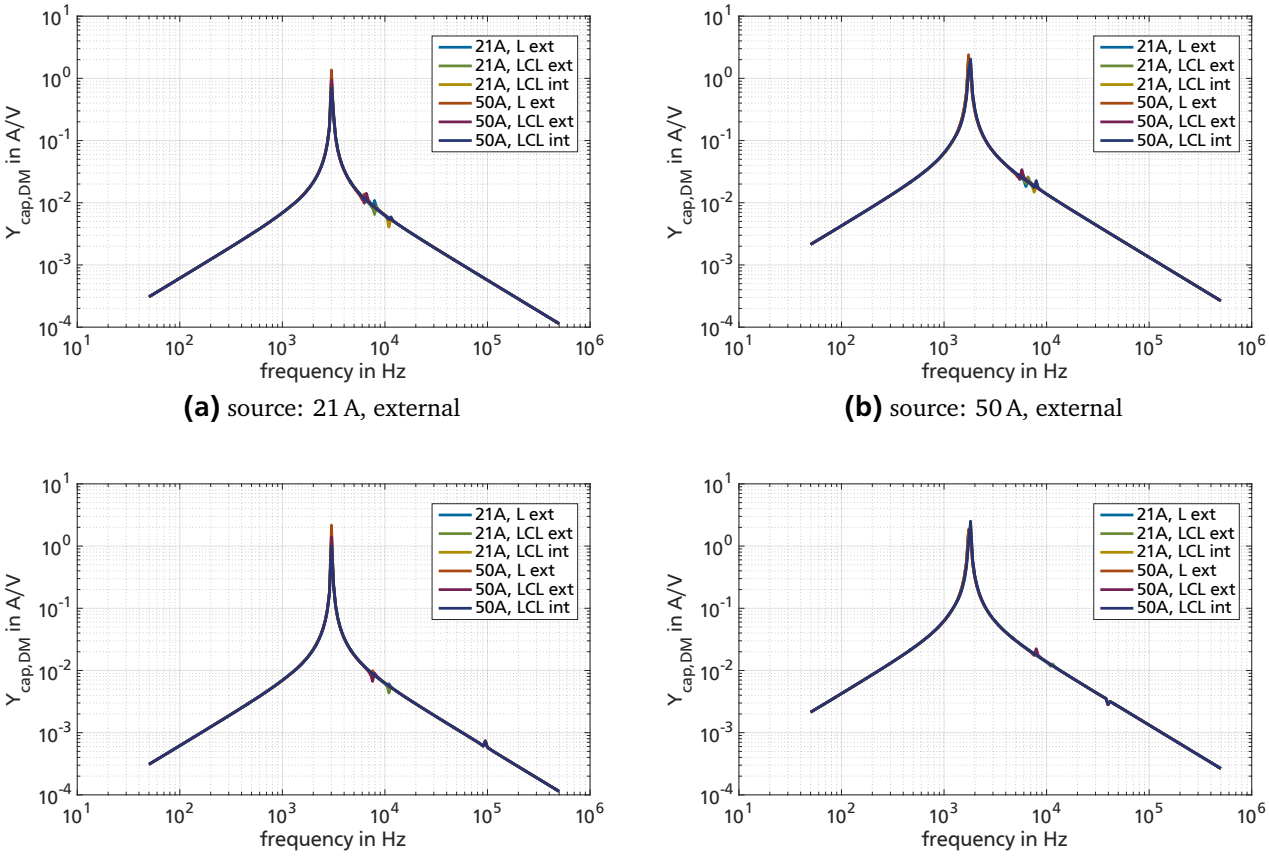

(a) source: 21 A, external

(b) source: 50 A, external

(c) source: 21 A, internal

(d) source: 50 A, internal

Figure 8.4.: DM currents in source converters LCL filter with different converters connected in parallel

Figure 8.5 shows the currents in the X-capacitors of the different types of noise sink converters when excited by the three topology variants of the 21 A converter. Because the results with the 50 A variants are equivalent they are omitted here. The first subfigure shows the excitation by a converter with inductance and EMI filter and a significant resonant peak can be excited in the neighboring converters if they have an external EMI filter at 31 kHz. When the EMI filter of the noise sink converter is integrated into the LCL filter this peak is shifted and decreased significantly and the excitability of the filter is less than that of its counterparts of the same current rating across the whole simulated frequency range.

The second subfigure in 8.5 shows the effect of the LCL in contrast to just an inductance as grid interface. Firstly an additional resonance appears in the simulation at 3.1 kHz, that is typically damped by the controller and will not appear as strongly in an actual setup. The benefit of this resonances is seen above 3 kHz where the excitation of neighboring converters is strongly damped compared to the case in the first subfigure. Due to the LCL filter, the decreasing slope of the DM transmission is larger than in case of the inductance in the first subfigure.

The third subfigure shows the results for the LCL with internal EMI filter, which looks similar to the case with external EMI filter. Only the last resonance and the corresponding damping is shifted to higher frequencies. The effective damping is worse than that of the LCL filter with external EMI filter but still significantly better than that of the inductance with EMI filter.

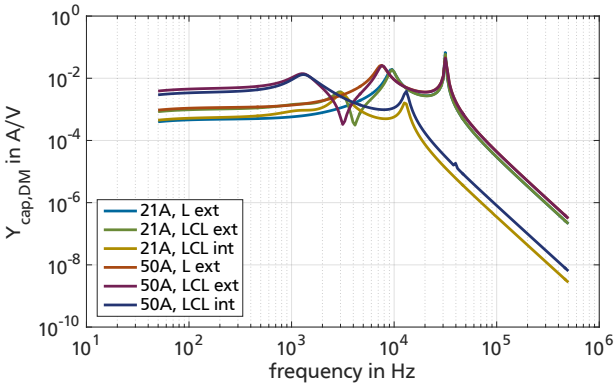

(a) source: 21 A, L ext; sink: according to label

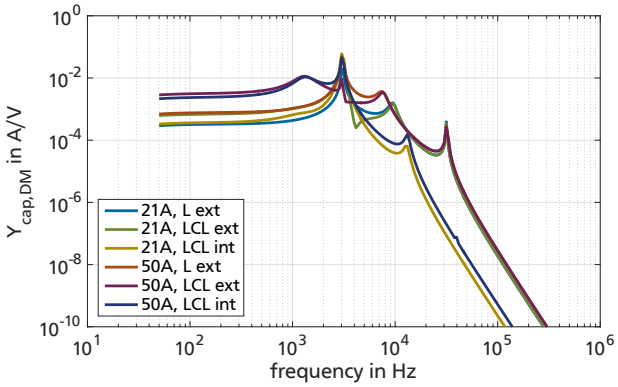

(b) source: 21 A, LCL ext; sink: according to label

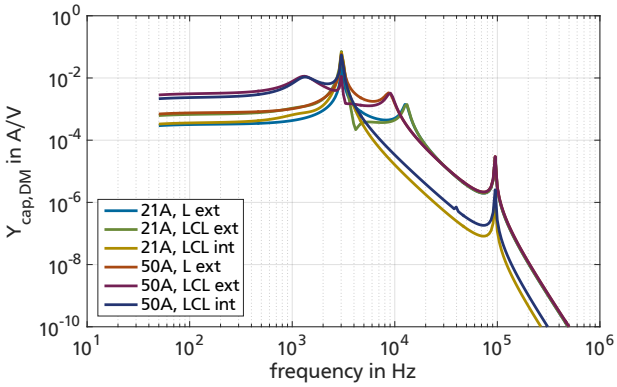

(c) source: 21 A, LCL int; sink: according to label

Figure 8.5.: DM currents in parallel converters' capacitors if excited from different converters

The CM behavior of the proposed grid interface is very similar to the DM behavior:

- The self generated capacitor currents are independent of parallel loads.
- The internal EMI filter capacitors are not significantly excited from outside, when viewed as noise sink.
- The high frequency damping is slightly worse than that of the LCL filter with external filter, but significantly better than that of the inductance with EMI filter.

The benefit of higher suppression of resonances and decreased excitation of resonances is gained with the tradeoff of reduced filter damping at high frequencies. Since no optimization of the proposed grid interface is done in this work and the overall needed components are reduced compared to the LCL filter with external EMI filter there is significant room for optimization of the filter parameters. For a real design of such a filter up to 30 MHz the parasitic properties of the used components have to be taken into account more closely than is the focus of this work. Suggested targets for optimization are:

- change distribution between C_{a} and C_{Xa}
- distribute C_{Ya} between both capacitive stages to realize 5$^{\mathrm{th}}$ order rather than 3$^{\mathrm{rd}}$ order CM filter
- add intentional DM inductance to LCMa, which does not interfere within controller bandwidth, but makes DM damping intentionally 5$^{\mathrm{th}}$ order rather than random due to stray inductance of common mode choke
- evaluate combination of cheap and high-frequency components in parallel (capacitors) or series (inductors) to realize good performance per cost ratio

9 Conclusion

This work presents the realized converter in chapter 2 with its control modifications in order to operate well even during resonances at its PCC. Chapter 3 introduces typical calculation methods in frequency domain and explains the method used in this work. The measurement procedures described in chapter 4 are used to determine the component models presented in chapter 5. Two parallel converters are simulated in chapter 6 and the influences on the resonance between filter capacitors and the power grid are shown. Chapter 7 validates those findings by measurement. Additionally the thermal impact on the filter capacitors during resonance and the distortion of the PCC voltage are analyzed. Finally chapter 8 uses the findings to propose a different structure for the grid interface of converters and demonstrates a reduced likeliness of resonances by simulation.

Concerning resonances in low power grids the work shows that the connection of capacitance in form of EMI filters or LC filters leads to a resonance between this capacitance and the inductive power grid. The damping of this resonance depends mainly on the grid impedance, which is typically unknown. The resonance frequency is determined by the total capacitance value, which might change over time, and the grid impedance. It can be assumed that the resonance frequency and amplitude in typical networks changes over time and is not known at any time.

The selected calculation method allowing asymmetrical components in frequency domain shows good results. One simulation of two parallel converters takes between 5 and 10 s depending on the complexity of the converters, when executed on one core of a mid-range laptop processor from 2013. Due to the assumptions made for the simulation an increase of simulation time proportional to the amount of converters is expected. (The ground reference ensures 8^{th} order matrices for any network size. Adding another converter simply adds the calculation of another parallel admittance.) The complexity of the used models is appropriate for the considered frequency range as the proximity of the simulations and measurements show. Only above 100 kHz deviations appear which are more likely to come from the measurements as the amplitudes at higher frequencies decrease almost to the noise floor of the measured specters. While representing the actual value better, than common assumptions, the initial measurement of the grid impedance shows a larger error than other component measurements. Optimizing the coupling circuits for the measurement of smaller impedances could improve the accuracy of the measured impedance amplitude. An error in the resistive part of the measurement will remain since small errors in the measured phase, which is close to 90°, result in much larger errors in measured resistance. Especially the asymmetrical cable model shows very promising results and is able to model the cable resonances much more accurate than symmetrical approaches do.

In summary the author strongly suggests a shift of the following two well established paradigms in power electronics:

1. The common assumption of an inductive power grid must be abandoned. Just one converter with EMI filter is enough to compensate the inductive grid impedance above a cut-off frequency and make the effective impedance capacitive. Depending on the size and design this can already

make the PCC capacitive within the frequency range of typical switching frequencies. The more converters add to the capacitance the lower the cut-off frequency becomes, making the assumption of an inductive grid more false.

2. A grid choke, LC filter or LCL filter is typically considered as a component separate from the EMI filter which are often even designed by different companies. This is usually justified by stating that the choke or LC/LCL filter is necessary to stay within the power quality limits whereas the EMI filter assures electromagnetic compatibility above 150 kHz and both components have no influence in the frequency range of the other component. This work however shows that influences of EMI filters are visible even at low frequencies. As a result, the complete grid interface should be designed as one functional unit to comply with standards of all frequency ranges while preventing resonances to appear in concordance with any possible surroundings. At least in critical applications an approach according to section 8.2 is imperative.

A Values used for Simulation

Table A.1 shows the parameters of the choke used in series connection of four (standard) or two (only in chapter 7 to imitate a converter with larger nominal power) inductors to realize nominal choke values of 5.4 mH and 2.7 mH.

Table A.1.: Values of the noise source choke according to figure 5.3

L	C	R
1.47 mH	40.6 nF	68 mΩ

Table A.2 shows the values used to model the noise sink choke and the LCL filter compared in section 6.3.

Table A.2.: Values of the noise sink choke L (L) and LCL (L1,C,L2) filter

L	$L1$	C	$L2$
2.8 mH	3.5 mH	27.7 μF	1.05 mH

Tables A.3 through A.5 show the values used for the comparison of the influence of the filter order in section 6.1. The ESR of each component is listed in the corresponding row. A coupling factor of 0.995 between the CM chokes windings is used.

Table A.3.: 2nd order EMI filter values

L_{CM1}	3.4 mH	ESR	14 mΩ
C_{x1}	12 μF	ESR	1.3 mΩ
C_{y1}	2 μF	ESR	8 mΩ

The noise source converter is modeled according to figure 5.21 with the values in table A.6.

The noise sink converter is modeled according to figure 5.21 with the values in table A.7.

Table A.8 shows the parameters of the two cables described in section 5.3. Figures 5.14 and 5.13 show the replacement circuits of the inductive and capacitive components. The chain matrices to be filled with the values from table A.8 are found in equations (5.15) and (5.21).

Table A.4.: 3rd order EMI filter values

L_{CM1}	3.4 mH	ESR	14 mΩ
C_{x1}	6 µF	ESR	2.6 mΩ
C_{y1}	2.3 µF	ESR	7 mΩ
C_{x2}	6 µF	ESR	2.6 mΩ

Table A.5.: 4th order EMI filter values

L_{CM1}	1.7 mH	ESR	7 mΩ
C_{x1}	6 µF	ESR	2.6 mΩ
C_{y1}	1 µF	ESR	16 mΩ
L_{CM2}	1.7 mH	ESR	7 mΩ
C_{x2}	6 µF	ESR	2.6 mΩ
C_{y2}	1 µF	ESR	16 mΩ

Table A.6.: Values of the noise source converter

Z_{blo}	$C_{CM,DC}$
1 MΩ	4 nF

Table A.7.: Values of the noise sink converter

Z_{blo}	$C_{CM,DC}$	C_{DM}	R_{DM}
1 MΩ	200 nF	10 µF	12.3 Ω

Table A.8.: Simulation values for the measured cables

	6 mm² unshielded	2.5 mm² shielded
r_{DC} in mΩ m^{-1}	0.915	2.2
$r_{DC,S}$ in mΩ m^{-1}	NA	1.1
Q_C	0.9826	0.9565
c_{12} in pF m^{-1}	47.07	56.4
c_{13} in pF m^{-1}	7.95	5.66
c_{1S} in pF m^{-1}	NA	169
Q_L	0.98	0.98
l_A in nH m^{-1}	612	803
l_B in nH m^{-1}	448	676
l_C in nH m^{-1}	916	1460
l_E in nH m^{-1}	NA	431
m_{12} in nH m^{-1}	692	113
m_{13} in nH m^{-1}	610	107

B Values for Comparison of Converter Designs

Tables B.1 through B.3 show the values of the components used for simulation in section 8.2.

Table B.1.: L with EMI filter as shown in figure 8.2

I_{AC}	L	C_X	C_Y	L_{CM}	C_{CM}
21 A	2.8 mH	2.52 µF	0.42 µF	1.9 mH	98 nF
50 A	1.2 mH	6 µF	1 µF	0.8 mH	2 µF

Table B.2.: LCL with external EMI filter as shown in figure 8.3

I_{AC}	L_1	C_1	L_2	C_{X1}	C_{Y1}	L_{CM1}	C_{CM1}
21 A	2.8 mH	2.8 µF	1.4 mH	2.52 µF	0.42 µF	1.9 mH	78 nF
50 A	1.2 mH	18.5 µF	0.6 mH	6 µF	1 µF	0.8 mH	796 nF

Table B.3.: LCL with internal EMI filter as shown in figure 8.1

I_{AC}	L_a	C_a	L_{CMa}	C_{Xa}	C_{Ya}	L_b	C_{CMa}
21 A	2.8 mH	320 nF	1.9 mH	2.52 µF	0.42 µF	1.4 mH	35 nF
50 A	1.2 mH	12.5 µF	0.8 mH	6 µF	1 µF	0.6 mH	274 nF

The parasitic properties of the components are selected to fulfill the following assumptions:

- ESR of capacitors with a loss factor of $1e^{-4}$ at 1 kHz
- DC resistance of CM chokes to generate 4 W of winding losses at nominal current
- coupling between windings of CM choke is 99.5 %

Bibliography

[AV06] Anderson, Brian D. O. ; Vongpanitlerd, Sumeth: *Network analysis and synthesis: A modern systems theory approach*. Reprint. Mineola, NY : Dover Publ, 2006. – ISBN 9780486453576

[BDL00] Briz, F. ; Degner, M. W. ; Lorenz, R. D.: Analysis and design of current regulators using complex vectors. In: *IEEE Transactions on Industry Applications* 36 (2000), Nr. 3, S. 817–825. http://dx.doi.org/10.1109/28.845057. – DOI 10.1109/28.845057. – ISSN 0093–9994

[BG16] Bienholz, Markus ; Griepentrog, Gerd: Prediction of harmonic current frequencies and amplitudes generated in Power Inductors due to Saturation in Ferrite and Iron Powder Cores. In: *2016 IEEE 2nd Annual Southern Power Electronics Conference (SPEC)* (2016)

[BG18] Bienholz, Markus ; Griepentrog, Gerd: Wide-Band Impedance Measurement for converter impedance determination in LV-Grids. In: *20th european conference on power electronics and applications (EPE ECCE Europe)* (2018)

[BSL+15] Brundlinger, Ronald ; Strasser, Thomas ; Lauss, Georg ; Hoke, Andy ; Chakraborty, Sudipta ; Martin, Greg ; Kroposki, Benjamin ; Johnson, Jay ; Jong, Erik de: Lab Tests: Verifying That Smart Grid Power Converters Are Truly Smart. In: *IEEE Power and Energy Magazine* 13 (2015), Nr. 2, S. 30–42. http://dx.doi.org/10.1109/MPE.2014.2379935. – DOI 10.1109/MPE.2014.2379935. – ISSN 1540–7977

[CBA+16] Chernet, Selam ; Bongiorno, Massimo ; Andersen, Gert K. ; Lund, Torsten ; Kjaer, Philip C.: Online Variation of Wind Turbine Controller Parameter for Mitigation of SSR in DFIG based Wind Farms. In: *IEEE Energy Conversion Congress and Exposition (ECCE)* (2016)

[CMB17] Cho, Yonghwan ; Mobarrez, Maziar ; Bhattacharya, Subhashish: A multi-loop controller for LCL-filtered grid-connected converters integrated with a hybrid harmonic compensation and a novel virtual impedance. In: *APEC* (2017). http://ieeexplore.ieee.org/servlet/opac?punumber=7922447

[CWZ+14] Chen, Cuili ; Wang, Zhiqiang ; Zhang, Yulong ; Li, Guofeng ; Wu, Yan: A novel passive damping LCL-filter for active power filter. In: *ITEC Asia-Pacific* (2014), S. 1–5. http://dx.doi.org/10.1109/ITEC-AP.2014.6940684. – DOI 10.1109/ITEC–AP.2014.6940684

[DIN71] DIN 40148 Blatt 3: Übertragungssysteme und Vierpole, Spezielle Dämpfungsmaße. (November 1971)

[DIN78] DIN 40148 Teil 1: Übertragungssysteme und Zweitore, Begriffe und Größen. (November 1978)

[DIN84] DIN 40148 Teil 2: Übertragungssysteme und Zweitore, Symmetrieeigenschaften von linearen Zweitoren. (Januar 1984)

[DIN11] DIN: *Voltage characteristics of electricity supplied by public distribution networks*. 2011-2. February 2011

[EBWB17] Ebrahimzadeh, Esmaeil ; Blaabjerg, Frede ; Wang, Xiongfei ; Bak, Claus L.: Harmonic Stability and Resonance Analysis in Large PMSG-Based Wind Power Plants. In: *IEEE Transactions on Sustainable Energy* (2017), S. 1. http://dx.doi.org/10.1109/TSTE.2017.2712098. – DOI 10.1109/TSTE.2017.2712098. – ISSN 1949–3029

[FCG+15] Freijedo, F. D. ; Chaudhary, R. T. ; Guerrero, Josep M. ; Bak, Claus L. ; Kocewiak, L. H. ; Jensen, C. F.: Harmonic Resonances in Wind Power Plants: Modeling, Analysis and Active Mitigation Methods. In: *IEEE PowerTech 2015 in Eindhoven* 2015 (2015)

[For18] Fortescue, C. L.: Method of Symmetrical Co-Ordinates Applied to the Solution of Polyphase Networks. In: *Transactions of the American Institute of Electrical Engineers* XXXVII (1918), Nr. 2, S. 1027–1140. http://dx.doi.org/10.1109/T-AIEE.1918.4765570. – DOI 10.1109/T–AIEE.1918.4765570. – ISSN 0096–3860

[GBM+15] Gervasio, F. A. ; Bueno, E. ; Mastromauro, R. A. ; Liserre, M. ; Stasi, S.: Voltage Control of Microgrid Systems Based on 3L-NPC Inverters with LCL-Filter in Islanding Operation. In: *International Conference on Renewable Energy Research and Application* 2015 (2015)

[Hel08] Heldwein, Marcelo L.: *EMC Filtering of Three-Phase PWM Converters*. Zürich, ETH, Dissertation, 2008

[IEC12] IEC 60725: *Consideration of reference impedances and public supply network impedances for use in determining the disturbance characteristics of electrical equipment having a rated current ≤75 A per phase*. 2012

[JF15] Jessen, Lars ; Fuchs, Friedrich W.: Modeling of inverter output impedance for stability analysis in combination with measured grid impedances. In: *IEEE 6th International Symposium on Power Electronics for Distributed Generation Systems (PEDG)* 2015 (2015). http://dx.doi.org/10.1109/PEDG.2015.7223037. – DOI 10.1109/PEDG.2015.7223037

[JGF+15] Jessen, Lars ; Gunter, Sandro ; Fuchs, Friedrich W. ; Gottschalk, Martin ; Hinrichs, Hans-J.: Measurement results and performance analysis of the grid impedance in different low voltage grids for a wide frequency band to support grid integration of renewables. In: *ECCE* 2015 (2015), S. 1960–1967. http://dx.doi.org/10.1109/ECCE.2015.7309937. – DOI 10.1109/ECCE.2015.7309937

[KKB02] Kaźmierkowski, Marian P. ; Krishnan, R. ; Blaabjerg, Frede: *Control in power electronics: Selected problems*. Amsterdam and New York : Academic Press, 2002 (Academic Press series in engineering). – ISBN 0080490786

[Kle76] Klein, Wilhelm: *Mehrtortheorie*. 3. Auflage. Berlin : Akad.-Verl., 1976

[KMR13] Küpfmüller, Karl ; Mathis, Wolfgang ; Reibiger, Albrecht: *Theoretische Elektotechnik: Eine Einführung*. 19. Springer, 2013

[Kno13] Knop, Andre: *Entwicklung eines schnelltaktenden Stromrichters für die Netzimpedanzanalyse im Frequenzbereich bis 10 kHz*. Kiel, Christian-Albrechts-Universität, Dissertation, 2013

[LABB07] Lascu, Cristian ; Asiminoaei, Lucian ; Boldea, Ion ; Blaabjerg, Frede: High Performance Current Controller for Selective Harmonic Compensation in Active Power Filters. In: *IEEE Transactions on Power Electronics* 22 (2007), Nr. 5, S. 1826–1835. http://dx.doi.org/10.1109/TPEL.2007.904060. – DOI 10.1109/TPEL.2007.904060. – ISSN 0885–8993

[LBH05] Liserre, M. ; Blaabjerg, F. ; Hansen, S.: Design and Control of an LCL-Filter-Based Three-Phase Active Rectifier. In: *IEEE Transactions on Industry Applications* 41 (2005), Nr. 5, S. 1281–1291. http://dx.doi.org/10.1109/TIA.2005.853373. – DOI 10.1109/TIA.2005.853373. – ISSN 0093–9994

[Lus11] Luszcz, Jaroslaw: Broadband Modeling of Motor Cable Impact on Common Mode Currents in VFD. In: *ISIE 2011* (2011)

[Lyo40] Lyon, Waldo V.: An extension of the method of symmetrical components using ladder networks. In: *Electrical Engineering* 59 (1940), Nr. 12, S. 1025–1030. http://dx.doi.org/10.1109/EE.1940.6435276. – DOI 10.1109/EE.1940.6435276. – ISSN 0095–9197

[LZHL11] Lei, Yi ; Zhao, Zhengming ; He, Fanbo ; Lu, Sizhao and Yin, Lu: An Improved Virtual Resistance Damping Method for Grid-Connected Inversters with LCL Filters: 17 - 22 Sept. 2011, Hyatt Regency Phoenix & Phoenix Convention Center, Phoenix, Arizona. In: *IEEE Energy Conversion Congress and Exposition (ECCE)* (2011)

[LZL+16] Lu, Xiangyu ; Zhang, Shuxue ; Liu, Chen ; Xie, Pengkang ; Chen, Henglin: Modeling of Common-mode Current in Motor Cable of Inverter-fed Motor Drive System. In: *APEC 2016* (2016)

[Pau06] Paul, Clayton R.: *Introduction to electromagnetic compatibility*. 2nd ed. Hoboken N.J. : Wiley-Interscience, 2006 (Wiley series in microwave and optical engineering). – ISBN 9780471755005

[PMCS14] Peña, José C.U. ; Melo, Guilherme ; Canesin, Carlos A. ; Sampaio, Leonardo P.: *IEEE Energy Conversion Congress and Exposition (ECCE) 2014*. 2014. – ISBN 97814 79956982

[PO03] Pignari, S. A. ; Orlandi, A.: Long-cable effects on conducted emissions levels. In: *IEEE Transactions on Electromagnetic Compatibility* 45 (2003), Nr. 1, S. 43–54. http://dx.doi.org/10.1109/TEMC.2002.808023. – DOI 10.1109/TEMC.2002.808023. – ISSN 0018–9375

[PST06] Petterson, Sami ; Salo, Mika ; Tuusa, H.: Applying an LCL-filter to a four-wire active power filter. In: *IEEE Power Electronics Specialists Conference* 2006 (2006)

[RT07] Routimo, M. ; Tuusa, H.: LCL Type Supply Filter for Active Power Filter - Comparison of an Active and a Passive Method for Resonance Damping: PESC 2007 ; 17 - 21 June 2007, Orlando, Florida, USA. In: *IEEE Power Electronics Specialists Conference* 2007 (2007)

[RVS14] Roinila, Tomi ; Vilkko, Matti ; Sun, Jian: Online Grid Impedance Measurement Using Discrete-Interval Binary Sequence Injection. In: *IEEE Journal of Emerging and Selected Topics in Power Electronics* 2014 (2014)

[SK11] Schwab, Adolf ; Kürner, Wolfgang: *Elektromagnetische Verträglichkeit*. 6., bearb. und aktual. Aufl. Berlin : Springer, 2011 (VDI-Buch). http://dx.doi.org/10.1007/978-3-642-16610-5. http://dx.doi.org/10.1007/978-3-642-16610-5. – ISBN 9783642166099

[SLD12] Sigle, Martin ; Liu, Wenqing ; Dostert, Klaus M.: On the Impedance of the Low-Voltage Distribution Grid At Frequencies Up to 500 kHz: [Beijing, China, 27-30 March 2012]. In: *IEEE International Symposium on Power Line Communications and Its Applications* 2012 (2012)

[SMR12] Suul, Jon A. ; Molinas, Marta ; Rodriguez, Pedro: Exploring the Range of Impedance Conditioning by Virtual Inductance for Grid Connected Voltage Source Converters. In: *3rd IEEE PES Innovative Smart Grid Technologies Europe (ISGT Europe), Berlin* 2012 (2012)

[VDE11] VDE: *Erzeugungsanlagen am Niederspannungsnetz*. 01. August 2011

[Web06] Weber, Stefan-Peter: Modellierung geschirmter Leistungskabel im Frequenzbereich der EMV. In: *EMV Messe und Kongress, Düsseldorf* (2006)

[Web07] Weber, Stefan-Peter: *Effizienter Entwurf von EMV-Filtern für leistungselektronische Geräte unter Anwendung der Methode der partiellen Elemente*. Berlin, TU Berlin, Dissertation, 2007

[WHCJ10] Wang, Liwei ; Ho, Carl ; Canales, Francisco ; Jatskevich, Juri: High-Frequency Cable and Motor Modeling of Long-Cable-Fed Induction Motor Drive Systems. In: *ECCE 2010* (2010)

[WHTB13] Wu, Weimin ; He, Yuanbin ; Tang, Tianhao ; Blaabjerg, Frede: A New Design Method for the Passive Damped LCL and LLCL Filter-Based Single-Phase Grid-Tied Inverter. In: *IEEE Transactions on Industrial Electronics* 60 (2013), Nr. 10, S. 4339–4350. http://dx.doi.org/10.1109/TIE.2012.2217725. – DOI 10.1109/TIE.2012.2217725. – ISSN 0278–0046

[WPC+16] Wu, Weibiao ; Peng, Li ; Chen, Manlin ; Wen, Tiliang ; Li, Yang ; Lei, Ji ; Dong, Fangming: Active Damping Control of Multiple Resonances for Grid-Connected Inverter With Long Transmission Cable. In: *ICIT 2016* 2016 (2016)

[Wue18] Wuerth Elektronik eiSos GmbH & Co. KG: WCAP-FTXX Film Capacitors: 890334026034. 2018 (2018). https://katalog.we-online.de/pbs/datasheet/890334026034.pdf

[YLY+16] Yang, Rongfeng ; Li, Lei ; Yu, Yannan ; Xu, Dianguo ; Cecati, Carlo: Grid Connected Converter Impedance Calculation under Virtual Synchronous Machine Control. In: *IEEE International Conference on Industrial Technology (ICIT)* 2016 (2016)

[ZJL+13] Zhang, Shao ; Jiang Shuai ; Lu, Xi ; Ge, Baoming ; Zheng Peng, Fang: Auto-tuning based Resonance Damping of Gridconnected Voltage Source Inverters with Long Transmission Cable. In: *ECCE 2013* (2013)

[ZJL+14] Zhang, Shao ; Jiang, Shuai ; Lu, Xi ; Ge, Baoming ; Peng, Fang Z.: Resonance Issues and Damping Techniques for Grid-Connected Inverters With Long Transmission Cable. In: *IEEE Transactions on Power Electronics* 29 (2014), Nr. 1, S. 110–120. – ISSN 0885–8993

[ZWMZ16] Zhao, Hui ; Wang, Shuo ; Min, Jianjun ; Zhi, Yongjian: Systematic Modeling for a Three Phase Inverter with Motor and Long Cable using Optimization Method. In: *ECCE 2016* (2016)

Publications

1. M. Bienholz, G. Griepentrog. "Prediction of harmonic current frequencies and amplitudes generated in Power Inductors due to Saturation in Ferrite and Iron Powder Cores", in *IEEE Southern Power Electronics Conference (SPEC)*. Auckland, New Zealand. December 2016

2. M. Bienholz, G. Griepentrog. "Influences on resonances between EMI filter capacitors and the utility grid", in *IEEE International Conference on Industrial Technology (ICIT)*. Lyon, France. February 2018

3. M. Bienholz, G.Griepentrog. "Wide-Band Impedance Measurement for converter impedance determination in LV-Grids", in *European Conference on Power Electronics and Applications (EPE ECCE Europe)*. Riga, Latvia. September 2018

Erklärungen laut Promotionsordnung

§ 8 Abs. 1 lit. c PromO

Ich versichere hiermit, dass die elektronische Version meiner Dissertation mit der schriftlichen Version übereinstimmt.

§ 8 Abs. 1 lit. d PromO

Ich versichere hiermit, dass zu einem vorherigen Zeitpunkt noch keine Promotion versucht wurde.

§ 9 Abs. 1 PromO

Ich versichere hiermit, dass die vorliegende Dissertation selbstständig und nur unter Verwendung der angegebenen Quellen verfasst wurde.

§ 9 Abs. 2 PromO

Die Arbeit hat bisher noch nicht zu Prüfungszwecken gedient.

Darmstadt, den 08. März 2019

Markus Bienholz